Nonlinear Capacitors for Superconducting Quantum Device Applications

Henry Chew

A dissertation submitted in partial fulfillment

of the requirements for the degree of

Doctor of Philosophy

of

University College London

Department of Electronic and Electrical Engineering
University College London

22 May 2025

I, Henry Chew confirm that the work presented in my thesis is my own. Where information has been derived from other sources, I confirm that this has been indicated in the thesis.

Abstract

The key components in superconducting quantum computing architectures are qubits, couplers, microwave elements and low-noise amplifiers among others. In a variety of these subsystems, nonlinear circuit elements are an essential ingredient which enables their functionality. In this thesis, we study two different superconducting elements used to implement nonlinear capacitors.

First we simulated a novel Josephson-junction-based tuneable nonlinear capacitor to couple flux qubits. Such a device implements a YY interaction, which has the potential to enhance the performance and extend the capabilities of current generation quantum annealers. We show that the interaction strength of the YY coupling is on the order of MHz and tuneable across zero. We discuss experimental realisations of this device to verify its function.

Next, we present our study of a low temperature parametric amplifier utilizing the nonlinear capacitance of quantum phase-slip nanowires. We have fabricated a single-nanowire and two-nanowire variants which shunt a quarter-wavelength superconducting coplanar waveguide resonator. We characterised the nonlinear properties of the first variant such as the power-dependent resonance frequency, idler generation and signal gain, while in the second variant we developed a lock-in detection method to investigate the gate voltage response and demonstrate that the device acts as a gate-voltage-tuneable resonator.

We also report on the progress towards a fabrication process for sputtered Al

overlap junctions in the LCN cleanroom. Back-sputter and in-situ oxide growth techniques are developed as an alternative to shadow evaporation. These techniques are better suited for large-scale integration as they do not rely on angular deposition, but they require better control over the interfaces due to patterning the two electrodes separately. We characterised the processes using resistance measurements and characterised their low temperature properties. We show that our junctions exhibit overdamped dynamics and the critical current is suppressed with RF radiation.

Impact Statement

Quantum technologies have attracted significant private and public investment, with a growing number of startups developing the technology to transform various industries such as finance, cybersecurity, material science and medicine. This thesis explores the practical aspects of quantum devices including numerical simulations of a Josephson junction-based capacitive coupler, and experiments on niobium nitride nanowires. The results presented in this work lays the groundwork for future research directions in the areas of qubit coupling hardware and parametric amplification, and is mainly of academic interest.

The designs and simulations of the YY coupler, as well as the experimental methods discussed enables these circuits to be fabricated for characterisation and verification, while providing a starting point for future circuit designs and further development is required before the coupling element can be integrated into commercial systems. Moreover, the feasibility study of fabricating overlap Josephson junctions in our cleanroom also gives a foundation for other researchers who wish to extend the junction interface preparation methods considered in this thesis.

Parametric amplifiers are of interest in low-temperature electronics, and for superconducting qubit readout. In the experiments on nanowire-based parametric amplifiers, we have found evidence for frequency mixing and gate-voltage tuneable capacitance in our resonators, demonstrating the operation principle of this novel device. We hope that this demonstration will stimulate future research to optimize our design for an alternative to amplifiers based on Josephson junctions.

Acknowledgements

This journey would not have been possible without the help of a great number of people. First I would like to thank my supervisor Prof. Paul Warburton. Ever since being a student in Paul's classes I have been fascinated by nanoelectronics and I am very grateful to him for welcoming me into such a stimulating research environment that he has fostered. His unwavering commitment to excellence, insightful critiques and kind support has significantly shaped my development as a researcher.

Next I wish to thank the group members who I looked to for guidance, especially when I started out in my PhD. I thank Dr. Louis Fry-Bouriaux for his generous mentorship. Louis taught me a great deal inside and outside the laboratory through his expertise and dedication. I could not have asked for a better mentor to learn the craft of experimental science from. I would also like to thank Dr. Gioele Consani for insights into quantum circuit simulations and Dr. Jamie Potter for his guidance and tips on all the quirks of the cleanroom. I would like to thank my fellow group-mates, Nuttamas Tubsrinuan and Leon Guerrero, it has been a pleasure working alongside you in the lab and bouncing ideas off each other; Natasha Feinstein and Robert Banks, I am glad to have shared this experience with you and to grow with you. It has been a thrill to have gone on this adventure with all of you.

I am indebted to the technical staff who keeps the LCN cleanroom running. I thank Steve Etienne, Vijayalakshmi Krishnan, Dr. Suguo Huo, Lorella Rossi, and

Rohit Khanna for always being available to offer technical assistance and advice. I would also like to thank my colleagues in the QuanCAP project, Dr. Jonathan Williams, Dr. Freya Johnson and Dr. Asem Elarabi, for all the fruitful discussions that has enhanced the quality of my work.

A special thanks to my friends and family who grounds me and who I can always rely on. I want to say thank you to my parents, for always believing in me, for motivating me, and helping me pursue the things they know I am capable of; my siblings for always being there for me and for inspiring me. None of this would have been possible without your unconditional love and support.

Contents

List of Symbols

E_C Single charge electrostatic potential energy

E_J Josephson coupling energy

E_L Inductive energy associated with a single flux quantum

E_S Quantum phase slip energy

I_c Josephson junction critical current

J_c Critical current density

L_J Josephson inductance

L_k Kinetic inductance

S_{21} Forward transmission scattering coefficient

T_c Critical temperature

V_c Nanowire critical voltage

Z_{in} Input impedance

Z Characteristic impedance

Λ London phenomenological parameter

Φ_0 Magnetic flux quantum

Φ_{ext} Externally applied flux

List of Symbols

β_L SQUID screening parameter

β_c Stewart-McCumber parameter

$\hat{H}_q$ Qubit Hamiltonian

$\hat{Q}$ Charge operator

$\hat{U}$ Schrieffer-Wolff projector

$\hat{\Phi}$ Flux operator

$\hat{a}$ Lowering operator

$\hbar$ Reduced Planck's constant

λ_L London penetration depth

ω_c Josepshon junction characteristic frequency

ω_p Josepshon junction plasma frequency

ω_q Qubit frequency

ω_r Resonator frequency

ϕ_{ext} Normalized externally applied flux

ϕ Josephson junction gauge-invariant phase different

$\sigma_{x,y,z}$ X,Y and Z Pauli matrices

φ Cooper pair wavefunction phase

$\vec{A}$ Magnetic vector potential

$\vec{B}$ Magnetic field

$\vec{E}$ Electric field

$\vec{j_s}$ Supercurrent density

List of Symbols

ξ_{GL} Ginzburg-Landau coherence length

f_z Reduced flux

f_i Idler frequency

f_p Pump frequency

f_{res} Resonance frequency

f_s Signal frequency

g Resonator-qubit coupling strength

h Planck's constant

m_s Cooper pair mass

n_s Cooper pair density

q_s Cooper pair charge

Acronyms

3WM Three-wave Mixing

4WM Four-wave Mixing

AC Alternating Current

AWG Arbitrary Waveform Generator

BCS Bardeen-Cooper-Schrieffer

CPB Cooper Pair Box

CPW Coplanar Waveguide

cQED circuit Quantum Electrodynamics

CW Continuous Wave

DC Direct Current

DI De-ionised

DUT Device-Under-Test

EBL Electron-Beam Lithography

ENIAC Electronic Numerical Integrator and Computer

FFT Fast-Fourier Transform

FWHM Full Width at Half Maximum

HEMT High Electron Mobility Transistor

ICP Inductively-Coupled Plasma

IPA Isopropyl Alcohol

JJ Josephson Junction

JPA Josephson Parametric Amplifier

LAMH Langer-McCumber-Halperin

LCN London Centre for Nanotechnology

LO Local Oscillator

MOSFET Metal-Oxide Field-Effect Transistor

PCB Printed Circuit Board

PMMA Poly(methylmethacrylate)

PVD Physical Vapor Deposition

QA Quantum Annealing

QND Quantum Non-Demolition

QPS Quantum Phase-Slip

RCSJ Resistively and Capacitively Shunted Junction

RF Radio Frequency

RIE Reactive-Ion Etching

SEM Scanning electron microscopy

Acronyms

SQUID Superconducting Quantum Interference Device

SW Schrieffer-Wolfe

TAPS Thermally Activated Phase Slips

TEM Transmission Electron Microscopy

TWPA Travelling Wave Parametric Amplifier

VNA Vector Network Analyser

List of Figures

List of Tables

Chapter 1

Introduction

1.1 Introduction

The technological advancement of digital computers has been dramatic, evolving from the massive, room-sized machines of the 1940s such as the ENIAC, to today's compact and powerful devices such as smartphones, laptops, and embedded systems that are ubiquitous in our everyday lives. With the advent of silicon integrated circuits and progressive miniaturization of MOSFETs, digital circuits have become not only significantly smaller in size but also substantially more complex, enabling their vast information processing capabilities. In spite of this, they are not well-suited for solving all types of computational problems. Certain tasks, such as simulating large quantum systems, are thought to be computationally intractable for classical computers[1], requiring exponentially increasing storage space and processing time to return a solution. This limitation has motivated the exploration of alternative computing paradigms, as solving these hard problems could yield significant innovations in technology and deepen our understanding of fundamental science. One such paradigm is quantum computing.

The discovery of several quantum algorithms that provide distinct computational advantages over classical ones greatly accelerated interest in quantum computing. Notable early examples include Shor's algorithm for integer factorization[2]

and Grover's algorithm for searching unsorted databases[3]. Shor's algorithm, for example, can factor large numbers exponentially faster than classical methods, allowing it to break widely used RSA encryption. Quantum computers can also be programmed to perform quantum simulations, that is, to efficiently and accurately predict the physical and chemical properties of materials, enabling the discovery and design of new materials[4][5] and pharmaceutical drugs[6].

Quantum computation is carried out by manipulating quantum bits, or qubits, which play an analogous role to bits in classical information processing. Qubit states can be manipulated in a discrete manner, through a sequence of operations called quantum gates, or alternatively their evolution can be carried out continuously, with this approach termed adiabatic quantum computation.

Qubits have been made out of various physical systems, with the main platforms being trapped ions, neutral atoms, silicon spin qubits, superconducting qubits and photonic qubits. Among these various implementations, each has its own advantages and drawbacks. Qubits based on natural physical systems have the longest coherence times, as in the case of approaches based on photons, atoms and ions which have coherence times in the order of minutes due to their weak interactions with the environments. These systems require specialized equipment for qubit control, and approaches to manufacture the technology at scale remains to be proven[7][8][9]. Silicon spin qubits, on the other hand, have coherence times up to a few milliseconds. These systems utilized nanostructures with dimensions of a few nanometres to confine electrons. The structure is known as a quantum dot, which behaves as an artificial atom[10]. This is an attractive candidate for building a quantum computer due to its compact size, and the support of mature semiconductor nanofabrication techniques, with the main challenge to this approach being the requirement of very precise control signals to operate the devices[11][12]. Superconducting qubits have typical coherence times on the order of 100 μs, but are also operated with much shorter gate times, in the tens of nanoseconds[13]. These type of qubits are artificial atoms based on the quantum states of

either the charge or flux degree of freedom in a superconducting circuit, allowing for excellent flexibility in the design and engineering of qubits, coupling elements and other classical peripheral devices[14][15]. This thesis aims to contribute towards this area of research.

Superconducting circuits have emerged as one of the most promising platforms for building quantum computers, leading to widespread adoption by some of the world's largest technology companies. One of the key advantages of this approach is the ability to leverage fabrication techniques used in conventional integrated circuit manufacturing, such as photolithography, thin-film deposition, and etching, which can be scaled for mass production. A superconducting circuit is composed of various elements such as capacitors, inductors, and Josephson junctions. Through careful design and arrangement of these components, engineers can precisely control key qubit properties. These circuits can be designed to be operated in the GHz frequency range, enabling integration with existing conventional RF electronics. To maintain their quantum properties, these circuits must be cooled to cryogenic temperatures, typically around 10 milliKelvins, which can be achieved using commercial dilution refrigerators. This requirement opens up a new demand for low-temperature RF electronics, which play an important role as part of the control and measurement subsystems for quantum processors.

1.2 Thesis Outline

This thesis is structured as follows. In Chapter 2, we give an introduction to the background theory needed to understand the operation of superconducting devices. We give a description of superconductivity and then introduce the constitutive relations of the Josephson junction (JJ) and quantum phase-slip (QPS) nanowire. We also discuss some relevant quantum circuits such as the Cooper pair box, RF SQUID flux qubit and QPS transistor.

1.2 Thesis Outline

Chapter 3 provides the context and motivation for the work presented in the thesis. Here we describe the limitations of coupling elements currently implemented in quantum annealers and the utility of a JJ-based tuneable nonlinear capacitor. Then we provide a description of parametric amplification and discuss the scope for a novel design of a parametric amplifier using the nonlinear capacitance of a QPS nanowire.

Chapter 4 presents the numerical simulations of the tuneable YY coupler for flux qubits. We discuss the design criteria and challenges in the physical implementation of the coupler. We described the design of an experimental test which would allow us to verify and characterise the device.

Chapter 5 builds on the goals of Chapter 4 and presents the development of a new fabrication process for Al-based JJs in the LCN cleanroom. We describe our backsputtering and oxide growth methods used to prepare the JJ interface and oxide barrier, and present experimental results from our device characterisation in a dilution refrigerator which show that we can produce nonhysteretic JJs using our process.

Chapter 6 concerns fabrication and measurement of two NbN-based nonlinear resonators. The first device contains a single nanowire shunting a quarter wavelength resonator, and I present experimental results on its nonlinear behaviour, mixing properties and amplification. The second device is a electrostatically-gated variant of the first, which has two nanowires. With this device we demonstrate the periodic tuning of the resonance frequency of the device by a gate voltage which we attribute to the nonlinear capacitance of the nanowires.

Chapter 7 we conclude the thesis with a summary and outlook of the work presented.

Chapter 2

Background Theory for Superconducting Quantum Devices

2.1 Superconductivity

First observations of superconductivity were seen when experiments in the low-temperature lab of Kamerlingh Onnes in 1911 found that the electrical resistivity of metals such as mercury, tin and lead suddenly disappeared when cooled below a critical temperature T_c. Another characteristic property of superconductors which marks them as a different thermodynamic state from metals is the expulsion of magnetic fields below the critical temperature as discovered by Meissner and Ochsenfeld in 1933.

The first theoretical efforts to understand the new state were phenomenological theories that did not seek to provide a microscopic description, but explained the experimental observations. One such successful model was the electromagnetic theory of superconductors of F. and H. London[16]. To describe the vanishing resistance and persistence of electrical current, Ohm's law is replaced by the first London equation,

$$\vec{E} = \Lambda \frac{\partial j_s}{\partial t}, \tag{2.1}$$

with the phenomenological parameter

$$\Lambda = \frac{m_s}{n_s q_s^2}, \tag{2.2}$$

where q_s, n_s, and m_s are the charge, number density, and mass of the carriers and $\vec{j}_s$ is the density of the superconducting current (supercurrent). On the other hand, the expulsion of magnetic fields is a consequence of the second London equation

$$\nabla \times \vec{j}_s = -\Lambda \vec{B}, \tag{2.3}$$

which leads to exponentially decaying magnetic fields within the superconductor,

$$\nabla^2 \vec{B} = \frac{1}{\lambda_L^2} \vec{B}, \tag{2.4}$$

where $\lambda_L^2 = \frac{\Lambda}{\mu_0}$ is the London penetration depth of a superconductor.

With the development of quantum theory, it became recognized that superconductivity is a macroscopic quantum phenomenon, with the charge carriers described by a phase-coherent quantum wavefunction[17]. Ginzburg and Landau's theory[18] was based on such an approach which describes the transition from the normal to superconducting phase in terms of an order parameter $\psi(\vec{r}, t) = |\psi(\vec{r}, t)| e^{i\varphi(\vec{r}, t)}$, representing a wavefunction of the superconducting electrons so that $n_s = |\psi(\vec{r}, t)|^2$ [19].

Another key advancement is the first microscopic theory of superconductivity, BCS theory[20] due to Bardeen, Cooper and Schrieffer, describing the formation of a condensate at low temperatures, where all the charge carriers in the superconductor occupy the same quantum-mechanical ground state. This was shown

to be possible because of the formation and condensation Cooper pairs, pairs of electrons in a metal bound by electron-phonon interactions[21]. The pairing mechanism gives rise to an energy gap 2Δ which is required to create a pair of excitations from the superconducting ground state[22][23]. This gap is temperature-dependent but far below T_c BCS predicts $\Delta(T=0) = 1.764 k_B T_c$, where k_B is Boltzmann's constant. This has found quantitative agreement with various experiments, such as the low-temperature specific heat of vanadium specimens[24], the absorption of electromagnetic energy by superconducting films[25] and the tunnelling of electrons across an oxide layer to a normal metal[26].

Manifestations of the quantum mechanical nature governing superconductors have dramatic physical consequences. The macroscopic wavefunction and the fact that charge carriers have twice the elementary charge is demonstrated in the phenomenon of flux quantization within a superconducting loop, where magnetic flux threading the loop can only take discrete values in units of the magnetic flux quantum $\Phi_0 = \frac{h}{2e}$, where h is Planck's constant. From quantum mechanics, the phase gradient of a wavefunction in the presence of a magnetic field $\vec{B} = \nabla \times \vec{A}$ is[27]

$$\nabla\varphi = \frac{1}{\hbar}\left(\frac{m_s}{q_s n_s}\vec{j}_s + q_s\vec{A}\right), \tag{2.5}$$

where $\hbar = \frac{h}{2\pi}$ is the reduced Planck's constant, q_s is the charge of the carrier, $\vec{j}_s$ is the supercurrent density and $\vec{A}$ is the vector potential of the magnetic field. Around a multiply-connected superconductor, the wavefunction must be single-valued, so that upon integrating around the loop once, the phase difference must be a multiple of 2π, and

$$\oint(\nabla\varphi)\cdot d\vec{l} = 2\pi n = \frac{q_s\Lambda}{\hbar}\oint\vec{j}_s\cdot d\vec{l} + \frac{q_s}{\hbar}\oint\vec{A}\cdot d\vec{l}, \tag{2.6}$$

where n is the winding number of the wavefunction. For a sufficiently thick superconductor, taking a contour deep inside the material for which $\vec{j}_s = 0$, the above equation gives the flux quantization condition

$$\Phi = n\Phi_0, \tag{2.7}$$

where $\Phi_0 = \frac{h}{q_s}$. This was found to be the case with $q_s = 2e$ by the measurements of trapped flux in thick cylindrical superconductors in 1961 by Deaver and Fairbank[28] around the same time as Doll and Näbauer[29]. For cases where $\vec{j}_s$ cannot be taken to be zero, the condition is modified so that the quantity on the right hand side of (2.6) called the fluxoid, is quantized, so that

$$n\Phi_0 = L_k I + \Phi, \tag{2.8}$$

where for a loop of length l and cross-sectional area A, the quantity $L_k = \frac{\Lambda l}{A}$ is the kinetic inductance of the superconductor[27].

2.2 Superconducting Circuit Elements and Devices

2.2.1 Josephson Junctions

Josephson junctions (JJ) are to superconducting circuits what p-n junctions are to semiconductor electronics. First theorized in 1963 by Josephson[30], the effect was experimentally demonstrated soon after in the same year by Anderson and Powell[31]. A JJ is a tunnel junction consisting of two superconducting electrodes separated by a thin insulating barrier through which Cooper pairs can tunnel. The constitutive relations for a JJ are[30]

$$I = I_c \sin\phi, \tag{2.9}$$

$$V = \frac{\hbar}{2e}\frac{d\phi}{dt}, \tag{2.10}$$

where $\phi = \varphi_2 - \varphi_1 - \frac{2\pi}{\Phi_0}\int_1^2 A_z dz$ is the gauge-invariant phase difference across the JJ. When $V = 0$ a dc supercurrent can flow across the junction with a maximum value of I_c, while for $V_0 \neq 0$ the current oscillates at the Josephson frequency $\omega_0 = \frac{2eV_0}{\hbar} = 483.6\ \text{MHz}/\mu\text{V}$. Under ac driving, such as when induced by microwave irradiation, the IV curve exhibits steps at constant voltages. With the ac voltage component $V = V_0 + V_1 \cos(\omega_1 t)$, the phase evolves as

$$\phi(t) = \phi_0 + \omega_0 t + (\frac{2e}{\hbar\omega_1}) \sin\omega_1 t, \tag{2.11}$$

so that after using the expansion of the sine of a sine in terms of the Bessel functions of the first kind, the current,

$$I(\phi(t)) = I_c \sum (-1)^n J_n(\frac{2eV_1}{\hbar\omega_1}) \sin(\phi_0 + \omega_0 t - n\omega_1 t), \tag{2.12}$$

has a dc component if $\omega_0 = n\omega_1$, at constant dc voltages $V_0 = \frac{n\hbar\omega_1}{2e}$ known as Shapiro steps in the IV characteristic[32].

Furthermore, the constitutive relations (2.9), (2.10) define a nonlinear Josephson inductance

$$L_J = \frac{\Phi_0}{2\pi I_c \cos\phi}, \tag{2.13}$$

which is periodic in ϕ. In practical junctions, the ideal behaviour given by Eq. (2.9) and (2.10) is supplemented by including a shunt resistance R describing the dissipation presented in the finite voltage state, and a shunt capacitor C for the geometric capacitance due to the separation of the electrodes[33]. This is known as the resistively and capacitively shunted junction (RCSJ) model shown in Figure 2.1a, and the constant current bias IV characteristic is given by the solutions to the differential equation

$$I = I_c \sin\phi + C\frac{\Phi_0}{2\pi}\ddot{\phi} + \frac{\Phi_0}{2\pi R}\dot{\phi}. \tag{2.14}$$

Here the bias current I is equated to the sum of currents through the ideal junction, shunting resistance and capacitance. This equation can be seen through the lens of Lagrangian Mechanics, with kinetic energy $K(\dot{\phi}) = \frac{CV^2}{2} = \frac{C\dot{\phi}^2}{2}$ and potential energy $U(\phi) = -E_J \cos\phi - \frac{I\Phi_0}{2\pi}\phi$. The potential can be visualised in Figures 2.1b and 2.1c, and is known as the tilted washboard potential. Below the critical current in Figure 2.1b, the phase oscillates about a local minimum to give zero average voltage. On the other hand in Figure 2.1c, the bias is above the critical current, the phase is in the running state, as it rolls down the potential, leading to finite voltage. Rearranging (2.14), we have

$$\begin{aligned} i = \frac{I}{I_c} &= \sin\phi + \frac{1}{\omega_p^2}\ddot{\phi} + \frac{1}{\omega_c}\dot{\phi}, \\ &= \sin\phi + \frac{\beta_c}{\omega_c^2}\ddot{\phi} + \frac{1}{\omega_c}\dot{\phi}, \end{aligned} \tag{2.15}$$

where $\omega_p = \sqrt{\frac{2\pi I_c}{C\Phi_0}}$ is the plasma frequency, the frequency at which the phase oscillates about the minimum, $\omega_c = \frac{2\pi I_c R}{\Phi_0}$ is the characteristic Josephson frequency with $V = I_c R$ and $\beta_c = (\frac{\omega_c}{\omega_p})^2 = \frac{2\pi I_c R^2 C}{\Phi_0}$ is the Stewart-McCumber parameter. When $\beta_c < 1$, the junction is said to be overdamped and the phase is quickly trapped in the potential minimum when the bias current is reduced below I_c. This results in a non-hysteretic IV characteristic as shown in Figure 2.1d for $\beta_c = 0.656$ with $I_c = 10\ \mu A$, $R = 6\ \Omega$ and $C = 0.6\ pF$. In the underdamped case $\beta_c \geqslant 1$, the phase continues rolling down the potential, even when the bias current is less than the critical current. The results is a hysteretic IV curve, as shown by the normalized current-voltage characteristics for $\beta_c = 2, 20, 200$ in Figure 2.1e. The arrows indicate the direction in which the current is changed. For $\beta_c = 2$, the return current enters the zero voltage state at a lower current than the critical current. A hysteresis loop occurs, with the size of the loop increasing with β_c.

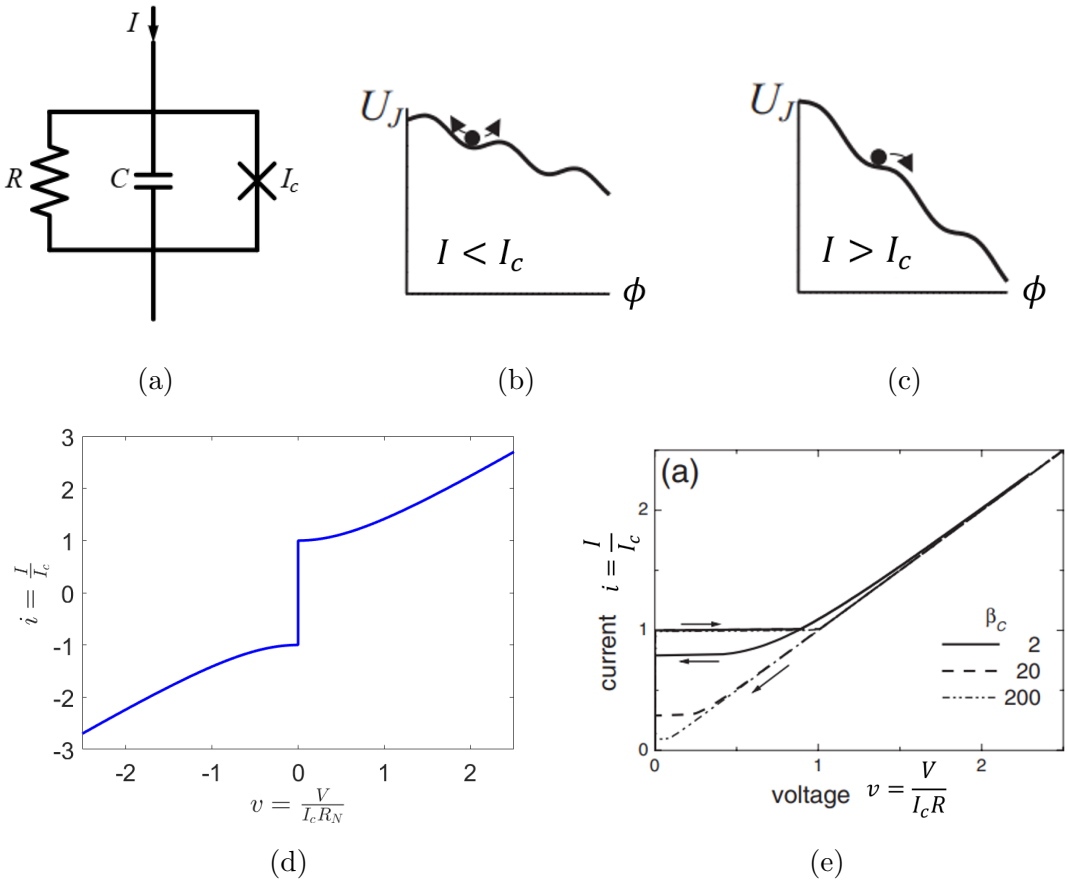

Figure 2.1: (a) Circuit of the RCSJ model of the Josephson junction, the circuit element represented by a cross is an ideal Josephson junction. (b) Low current bias regime $I < I_c$ leads to an oscillating phase about a fixed point. (c) Exceeding the critical current $I > I_c$ leads to the running state. The change of phase over time leads to a voltage. (d) Four-quadrant non-hysteretic current-voltage characteristic in normalized units for a JJ with $\beta_c = 0.656$. (e) First quadrant of hysteretic current-voltage characteristics in normalized units of a JJ with $\beta_c = 2, 20, 200$. Figures adapated from [27].

2.2.2 DC and RF Superconducting Quantum Interference Devices (SQUIDs)

DC SQUID

When a JJ is part of a superconducting loop, the phase drop across the junction modifies the flux quantization condition (2.7) to give a relation between the total flux in the loop and phase difference across the junctions. Figure 2.2 shows a device called the DC SQUID, consisting of two JJs in a superconducting loop, operating based on this principle.

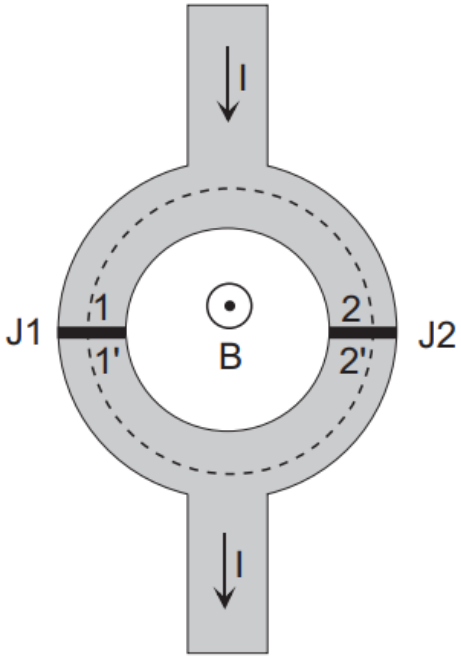

Figure 2.2: Device structure of a DC SQUID. The regions in grey are superconducting wires, while the black rectangles labelled J1 and J2 are tunnel junctions. An external magnetic field B gives rise to flux Φ_{ext} through the loop. The dashed line shows the integration contour. Figure is from reference [27].

The device is operated by applying an external magnetic field B, which gives rise to flux Φ_{ext} through the loop. Taking the phase drops into account when performing the integration (2.6) around the loop and across the junction yields a relation between the winding number of the wavefunction around the loop, n, the phase drop across the two junctions, ϕ_1 and ϕ_2 and the total flux of through the loop Φ, given by[27]

$$\begin{aligned} 2\pi n &= \frac{2\pi}{\Phi_0}\left[\Phi_{ext} + \Lambda(\int_2^1 \vec{j_s}\cdot d\vec{l} + \int_{1'}^{2'} \vec{j_s}\cdot d\vec{l})\right] + \phi_1 - \phi_2, \\ &= \frac{2\pi\Phi}{\Phi_0} + \phi_1 - \phi_2, \end{aligned} \tag{2.16}$$

where $\Phi = L_k I + \Phi_{ext}$ is the total flux through the loop. The DC SQUID behaves as an effective JJ, with a flux-tuneable critical current $I_{c,eff}(\Phi_{ext})$. In general, the value of this effective critical current can only be determined by solving the current-phase relation (2.9) for each junction and (2.16) numerically, but a simple expression exists for the case when L_k is negligible and when the two junctions are identical. In this case, the current through the two arms of the loop is

$$\begin{aligned} I &= I_c(\sin\phi_1 + \sin\phi_2), \\ &= 2I_c\cos(\frac{\pi\Phi_{ext}}{\Phi_0})\sin(\frac{\phi_1+\phi_2}{2}), \end{aligned} \tag{2.17}$$

and the effective critical current of the DC SQUID is $I_{c,eff} = 2I_c|\cos(\frac{\pi\Phi_{ext}}{\Phi_0})|$, which can be tuned to zero. The effect of asymmetry in the junctions leads to decrease in the modulation depth of $I_{c,eff}$[27].

RF SQUID

A variant using only a single JJ in the loop is called the RF SQUID as shown in Figure 2.3.

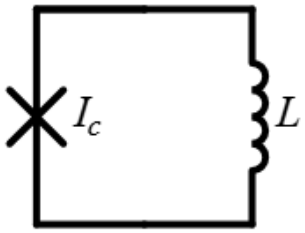

Figure 2.3: Circuit diagram of an RF SQUID.

The flux quantization condition for this device can be obtained by setting one of the phases in (2.16) to be zero. Considering the classical potential for the RF SQUID, we find

$$U(\phi) = E_L \left[\frac{\phi^2}{2} - \beta_L \cos\left(\phi + \phi_{ext}\right) \right], \tag{2.18}$$

with $\phi_{ext} = \frac{2\pi\Phi_{ext}}{\Phi_0}$, $E_L = \frac{\Phi_0^2}{4\pi^2 L}$, and $\beta_L = \frac{2\pi L I_c}{\Phi_0}$ is known as the screening parameter. The classical solution of the phase is found by minimizing the potential,

$$\frac{dU}{d\phi} = E_L \left[\phi + \beta_L \sin\left(\phi + \phi_{ext}\right)\right] = 0. \tag{2.19}$$

When $\beta_L < 1$, the potential has a global minimum and (2.19) gives only one solution. The result is a screening current that is periodic in external flux, following an oscillatory behaviour as shown in Figure 2.4.

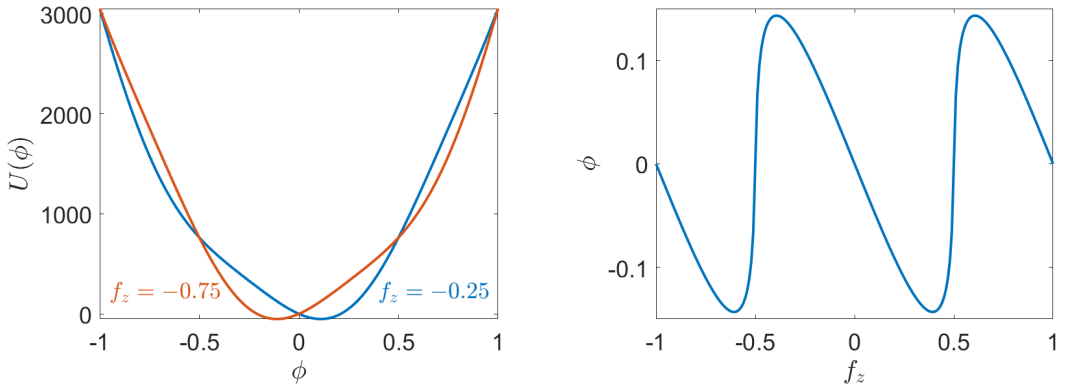

(a) (b)

Figure 2.4: (a) Classical RF SQUID potential for $f_z = -0.75$ and $f_z = -0.25$. The position of the minimum is given by the equation (2.19). (b) Self-flux curve for an RF SQUID from solving (2.19). $\beta_L = 0.9$ and $E_L = 155\ GHz$ in these plots.

In the opposite case when $\beta_L > 1$, there will in general be multiple minima in the potential, with it taking at low energies the form of a double-well potential when $f_z = \frac{\phi_{ext}}{2\pi} = \frac{1}{2}$. This situation is illustrated for $\beta_L = 1.3$ in Figure 2.5 for $f_z = 0.5$, $f_z = 0.5 + \delta f$ and $f_z = 0.5 - \delta f$ with $\delta f = 0.005$. Classically, the phase ϕ is localised at the minimum of the well, so Figures 2.5b and 2.5c corresponds to screening currents $\pm I_c \sin\phi$ flowing clockwise and anticlockwise in the loop. These two states underlie the operating principle of a flux qubit, playing the role of computational states, as discussed later. When treating the problem quantum mechanically, at the degeneracy point $f_z = 0.5$ where the minimum is degenerate as depicted in Figure 2.5a, the energy levels become split by an amount Δ due quantum tunnelling across the potential barrier separating the two wells. The energy eigenstates in this case become symmetric and antisymmetric superpositions of the two circulating current states. Biasing away from this point lifts the degeneracy and introduces energy asymmetry ϵ between the two states and favours one current direction.

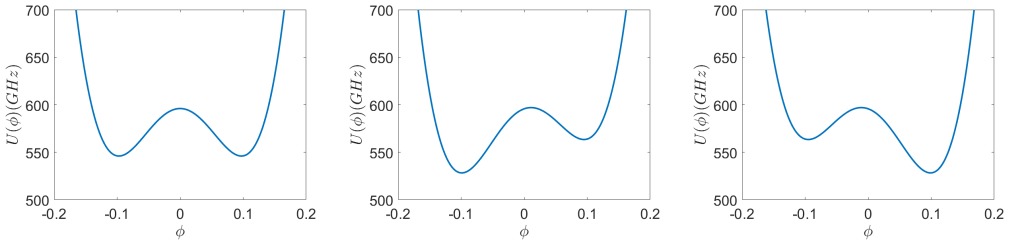

(a) $f_z = 0.5$ (b) $f_z = 0.505$ (c) $f_z = 0.495$

Figure 2.5: Classical potential of the RF SQUID in the double well regime for $\beta_L = 1.3$, $E_L = 458\ GHz$.

2.2.3 Quantum Circuits

The discussion in the previous section treated ϕ as a continuous variable which is valid in the case of large area junctions where $E_J \gg E_C$ when the phase is a good quantum number. Even in this case, the quantum mechanical nature of the phase can be exhibited, as shown in experiments demonstrating the quantum tunnelling of the phase through the JJ washboard potential[34], energy quantisation[35] and even coherent manipulation of quantum states in current-biased JJs[36]. With increased sophistication in device fabrication techniques and experimental instrumentation, it has become necessary and practical to consider circuits for which the number of Cooper pairs and the superconducting phase become quantum observables[37][38][39], obeying the commutation relation $[\hat{\phi}, \hat{n}] = i$. The quantum-mechanical treatment of superconducting circuits is used extensively in the design and operation of qubit circuits. The approach used is reminiscent of traditional, classical analysis of lumped-element electrical circuits, where the voltage and currents are specified across the element terminals but in the case of quantum circuits, the degrees of freedom in the circuit are represented by quantum operators, rather than classical variables. As in the standard method of canonical quantization, the classical Hamiltonian is first obtained, and the dynamical variables are then promoted to canonically conjugate quantum observables[39][40]. We first illustrate this by considering a quantum LC resonator and then discuss some important quantum circuits relevant to the rest of the thesis.

While in classical circuit analysis the constitutive relations of the inductor and capacitor, $V_L = L\frac{dI_L}{dt}$ and $I_C = C\frac{dV_C}{dt}$ are used, in quantum circuit analysis the time integral of voltages and currents are more commonly used, so that the relations become $\Phi_L = LI_L$ and , $Q_C = CV_C$, where $\Phi_L(t) = \int_{-\infty}^{t} V_L(t')dt'$ is the magnetic flux in the inductor and $Q_C(t) = \int_{-\infty}^{t} I_C(t')dt'$ is the charge on the positive terminal of the capacitor. By Kirchoff's laws at the common node, $I = -I_L = I_C$ and $V = V_C = V_L$. The energy of the LC resonator $E = \frac{1}{2}LI^2 + \frac{1}{2}CV^2$ may be expressed in terms of the branch charge $Q = \int_{-\infty}^{t} I(t')dt'$ and node flux $\Phi = \int_{-\infty}^{t} V(t')dt$ to obtain the classical Hamiltonian

$$H = \frac{\Phi^2}{2L} + \frac{Q^2}{2C}, \tag{2.20}$$

where (Φ,Q) are the canonical position and momenta which obey Hamilton's equations $\frac{\partial H}{\partial Q} = \dot{\Phi}$ and $\frac{\partial H}{\partial \Phi} = -\dot{Q}$. In canonical quantization, the variables (Φ,Q) are mapped to quantum mechanical operators ($\hat{\Phi}$,$\hat{Q}$) which obey the canonical commutation relations $[\hat{\Phi}, \hat{Q}] = i\hbar$ and the quantum Hamiltonian for the LC circuit is

$$\hat{H} = \frac{\hat{\Phi}^2}{2L} + \frac{\hat{Q}^2}{2C}, \tag{2.21}$$

which can be diagonalized in the occupation number basis, the eigenvectors of the operator $\hat{n} = \hat{a}^\dagger \hat{a}$, by introducing the lowering operator $\hat{a} = \frac{1}{\sqrt{2\hbar Z}}(\hat{\Phi} + iZ\hat{Q})$, with $Z = \sqrt{\frac{L}{C}}$. One can show that

$$\hat{H} = \hbar\omega(\hat{a}^\dagger \hat{a} + \frac{1}{2}), \tag{2.22}$$

where $\omega = \sqrt{\frac{1}{LC}}$ is the resonant frequency of the oscillator and the extra $\frac{\hbar\omega}{2}$ term in the Hamiltonian is the zero-point energy of the oscillator.

Cooper Pair Box

The Cooper pair box (CPB)[41][42][43][44] consists of charges that are coherently coupled from a superconducting island to a reservoir through a JJ. A gate voltage V_g can be applied to change the electrostatic potential on the island as shown in Figure 2.6a.

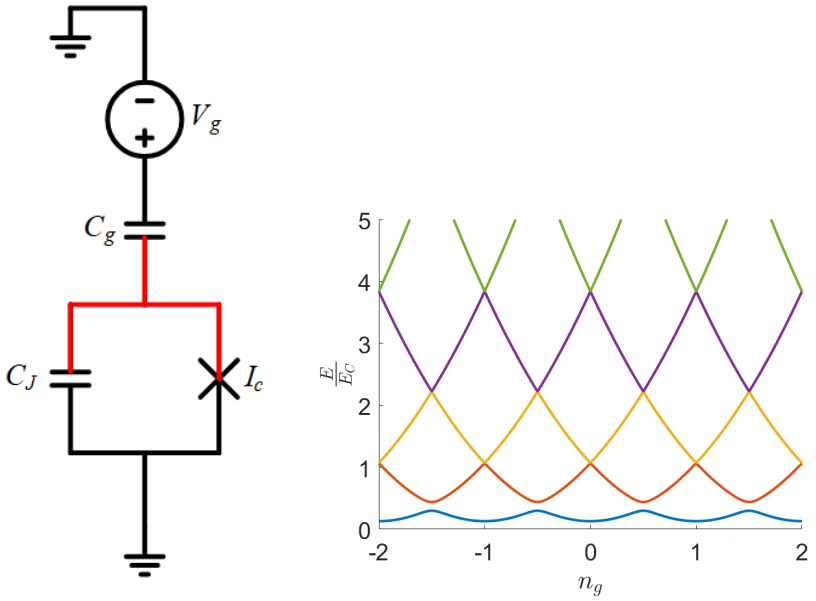

(a) (b)

Figure 2.6: (a) Circuit diagram for a Cooper Pair Box (CPB). (b) Energy spectrum normalized to E_C for a CPB with $C_g = 1\ fF$, $I_c = 10\ nA$, $C_J = 1.3\ fF$ and $\frac{E_C}{E_J} = 29$.

The electrostatic energy of an island with n Cooper pairs on the island is $E = 4E_C(n - n_g)^2$, where $n_g = \frac{C_g V_g}{e}$ is the normalised gate charge and $E_C = \frac{e^2}{2C_\Sigma}$ is the energy of a single charge held across total capacitance $C_\Sigma = C_g + C_J$, including the junction capacitance C_J. Thus, associated with this charging energy is a term in the CPB Hamiltonian[45][46]

$$\begin{aligned} \hat{H}_C &= 4E_C(\hat{n} - n_g)^2 \\ &= 4E_C \sum_n (n - n_g)^2 \left|n\right\rangle\left\langle n\right|, \end{aligned} \tag{2.23}$$

where n is the number of Cooper pairs that has tunnelled onto the island and $\hat{n} = \sum_n n \left|n\right\rangle\left\langle n\right|$ is the corresponding number operator. In addition to this, coherent tunnelling of Cooper pairs across the JJ contributes the Josephson coupling term in the Hamiltonian[47],

$$\hat{H}_J = -\frac{E_J}{2}\sum_n \Big[|n\rangle\langle n+1| + |n+1\rangle\langle n| \Big], \tag{2.24}$$

so that, the circuit is described by

$$\hat{H}_{CPB} = 4E_C \sum_n (n-n_g)^2 |n\rangle\langle n| - \frac{E_J}{2}\sum_n \Big[|n\rangle\langle n+1| + |n+1\rangle\langle n| \Big] \tag{2.25}$$

Without the E_J term, the spectrum consists of parabolas which cross at $n_g = \frac{1}{2}$. Under the presence of weak Josephson coupling $E_C \gg E_J$, the degeneracy is lifted by $2E_J$. The spectrum for $\frac{E_C}{E_J} = 29$ is calculated and plotted in Figure 2.6b.

While so far we have described the circuit in terms of the charge basis, the analysis could have been carried out in the phase basis. Phase states are $|\phi\rangle = \sum_n e^{in\phi}|n\rangle$, and one can verify that

$$\hat{H}_J |\phi\rangle = -E_J \cos\phi |\phi\rangle, \tag{2.26}$$

and neglecting the electrostatic component, the current operator associated with $\hat{H}_J$ is[48]

$$\begin{aligned} \hat{I}_J |\phi\rangle &= 2e\frac{d\hat{n}}{dt}|\phi\rangle = \frac{2e}{i\hbar}[\hat{n}, \hat{H}_J]|\phi\rangle \\ &= -i\frac{e}{\hbar}E_J \sum_n \Big[|n\rangle\langle n+1| - |n+1\rangle\langle n| \Big] |\phi\rangle \\ &= I_c \sin\phi |\phi\rangle \end{aligned} \tag{2.27}$$

where we recover the first Josephson junction with critical current $I_c = \frac{2e}{\hbar}E_J$.

Flux Qubit

The flux qubit[49][50][51][52][53] is a superconducting loop interrupted by JJs. The simplest version is illustrated in Figure 2.7, which is a RF SQUID with a loop of inductance L, a single JJ of critical current I_c and junction capacitance C_J.

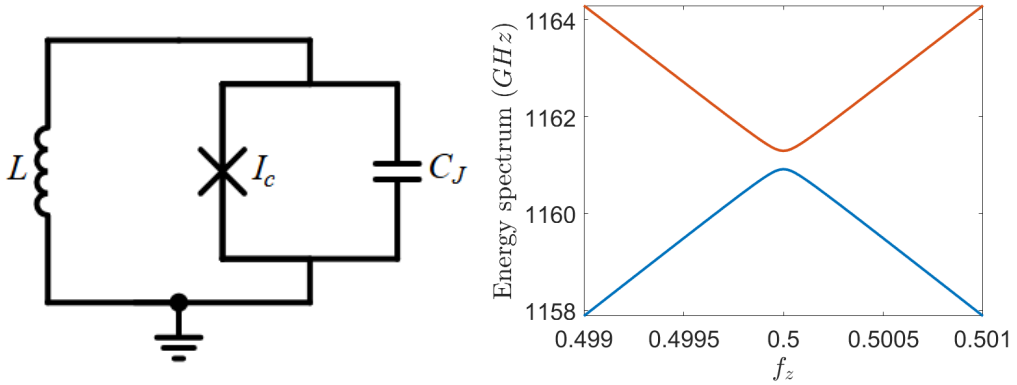

(a) (b)

Figure 2.7: (a) Circuit diagram for a RF SQUID flux qubit. (b) Low energy spectrum for a flux qubit with $L = 0.3\ nH$, $I_c = 1.2\ \mu A$ and $C_J = 24\ fF$.

The loop is associated with energy $E_L = \frac{(\Phi-\Phi_{ext})^2}{2L}$, where Φ is the total magnetic flux through the loop and Φ_{ext} is an applied external magnetic flux. By flux quantization in a RF SQUID loop (2.16) the Hamiltonian of the flux qubit becomes

$$\begin{aligned}\hat{H} &= \hat{H}_C + \hat{H}_L + \hat{H}_J \\ &= \frac{\hat{Q}^2}{2C_J} + \frac{\hat{\Phi}^2}{2L} - E_J \cos\left(\frac{2\pi(\hat{\Phi}+\Phi_{ext})}{\Phi_0}\right),\end{aligned} \tag{2.28}$$

which may be seen to be equivalent to (2.21) apart from the last term. Using the same definitions as the quantum LC oscillator, we obtain the energy spectrum by representing and diagonalizing the Hamiltonian in the harmonic oscillator basis[54]

$$\hat{H} = \hbar\omega(a^\dagger a + \frac{1}{2}) - \frac{E_J}{2}\left(\exp\left[i\frac{2\pi}{\Phi_0}\sqrt{\frac{\hbar Z}{2}}(a+a^\dagger)\right]e^{i\frac{2\pi\Phi_{ext}}{\Phi_0}} + h.c.\right), \tag{2.29}$$

where h.c. is the hermitian conjugate of the first term in the parenthesis. The two lowest energy eigenvalues are plotted for a flux qubit around the degeneracy point in Figure 2.7b. If we retain only the two lowest energy eigenstates, the system may be described by a two-level system,

$$\hat{H} = \frac{1}{2}(\epsilon\hat{\sigma}_z + \Delta\hat{\sigma}_x), \tag{2.30}$$

where the $\hat{\sigma}_x$ and $\hat{\sigma}_z$ are the X and Z Pauli matrices defined in the computational basis $\{|\uparrow\rangle, |\downarrow\rangle\}$[39][55]. Historically, this two-level Hamiltonian describes a spin-$\frac{1}{2}$ particle under the influence of magnetic fields, where ϵ is the longitudinal field that corresponds to the energy difference between the two spin states, and Δ is the transverse field which can be driven to induce spin-flips.

For a flux qubit, the computational basis states subject to preparation, manipulation and readout correspond to states of circulating currents. Thus, the computational basis states for the RF SQUID qubit are defined in terms of the current operator $\hat{I} = \frac{\hat{\Phi}}{L}$ and are made up of linear combinations of the energy eigenstates, given by relation[54]

$$\begin{aligned} \hat{I}_p\,|\uparrow\rangle &= +I_p\,|\uparrow\rangle\,, \\ \hat{I}_p\,|\downarrow\rangle &= -I_p\,|\downarrow\rangle\,, \end{aligned} \tag{2.31}$$

where $\hat{I}_p = \hat{P}_0\hat{I}\hat{P}_0$ is the current operator projected onto the low energy subspace with projector $\hat{P}_0 = |E_0\rangle\langle E_0| + |E_1\rangle\langle E_1|$. It is also of note that the charge operator $\hat{Q} = -i\sqrt{\frac{\hbar}{2Z}}(a - a^\dagger)$ is off-diagonal and imaginary in the computational basis, since $\langle m|\hat{a}|n\rangle = \sqrt{n}\delta_{m,n-1}$, where $|n\rangle$ are eigenvectors of $a^\dagger a$. Expanding the charge operator matrix element in this basis,

$$\begin{aligned} \langle E_i|\,\hat{Q}\,|E_j\rangle &= \sum_{m,n}\langle E_i|m\rangle\langle m|\,\hat{Q}\,|n\rangle\langle n|E_j\rangle\,, \\ &= -i\sqrt{\frac{\hbar}{2Z}}\sum_n \sqrt{n}\Big(\,\langle E_i|n-1\rangle\langle n|E_j\rangle - \langle E_i|n\rangle\langle n-1|E_j\rangle\,\Big), \end{aligned} \tag{2.32}$$

shows that the diagonal elements $\langle E_i|\hat{Q}|E_i\rangle$ are equal to zero, while off-diagonal elements are in general nonzero, but imaginary. Hence, in the low energy subspace, $\hat{Q}_p = \hat{P}_0\hat{Q}\hat{P}_0 \propto \hat{\sigma}_y$, which is a useful relation when considering capacitive coupling.

2.3 Quantum Phase-Slip Nanowires

As the transverse dimensions of a superconducting wire approach the Ginzburg-Landau coherence length ξ_{GL}, the wire loses its superconducting character. These types of wires exhibit finite resistance below T_c, attributed to fluctuations in the order parameter[56][57]. The finite voltage is generated by suppressing the magnitude of the order parameter at some point along the wire to zero, so that the phase is allowed to change by $\pm 2\pi$. Under constant current, by (2.10), these phase-slip events occur at an average frequency $\frac{2e\bar{V}}{h}$[33].

Phase slips may occur due to thermal or quantum effects. Thermally activated phase slips (TAPS) were the first to be modelled by Langer-Ambegaokar-McCumber-Halperin (LAMH) theory[58][59] which fitted well with residual resistance measurements of tin whisker crystals just below T_c[60][61]. As the temperature is decreased far below T_c, experiments with thin In[62] and PbIn[63] wires revealed a crossover point where the resistance of the wires diverges from the LAMH prediction. As TAPS drops quickly with temperature, this resistive tail is attributed to quantum phase slips (QPS), where the phase change is due to quantum tunnelling through the free energy barrier. Later measurements of nanowires showed that QPS can be so strong that the wire becomes insulating[64][65][66].

The tunnelling effect is analogous to the situation found in current-biased JJ discussed earlier, where quantum tunnelling of the phase can occur between adjacent minima of the tilted-washboard potential. This mechanism underlies the experimental observations of quantum phase slips in JJ arrays[67][68][69]. Figure 2.8 shows QPS in the two cases. (a) illustrates two successive potential wells of the JJ washboard potential, while in (b) δE_{ps} is the LAMH energy barrier, with U_C the condensation energy density, A_{cs} the cross-sectional area of the wire and ξ the length. In both cases, phase slips can be activated across the barrier thermally, or may quantum tunnel through it.

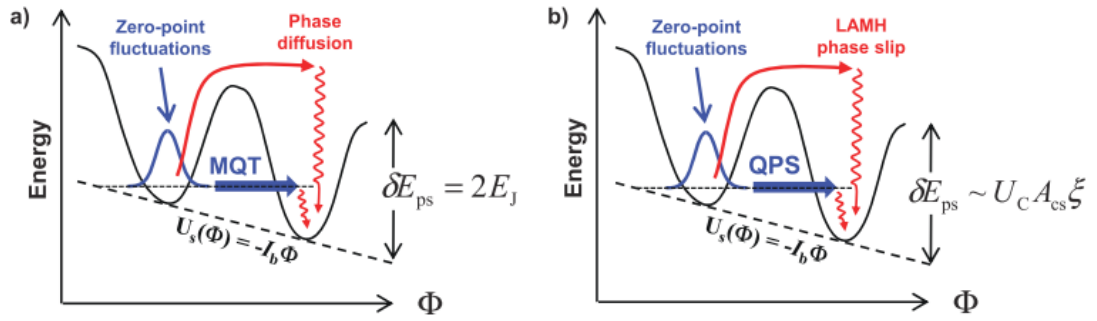

Figure 2.8: Thermal activation and macroscopic quantum tunnelling of the phase through a barrier for (a) Current-biased JJ. (b) Nanowire. Figures from [57].

These discoveries led to the proposal of the quantum phase-slip flux qubit[70]. Unlike a loop interrupted by a junction, the QPS flux qubit is a loop containing a nanowire, which, unlike a loop interrupted by a junction, can only change its phase by $\pm 2\pi$. From the phase-flux relation given by flux quantization (2.7), this corresponds to changing of flux in the loop by $\pm\Phi_0$. The Hamiltonian describing the circuit is

$$\hat{H}_{QPS} = E_L \sum_n (n-f)^2 \left|n\right\rangle\left\langle n\right| - \frac{E_S}{2} \sum_n \Big[\left|n\right\rangle\left\langle n+1\right| + \left|n+1\right\rangle\left\langle n\right| \Big], \tag{2.33}$$

where $f = \frac{\Phi_{ext}}{\Phi_0}$ is the magnetic flux applied to the loop, $E_L = \frac{\Phi_0^2}{2L}$ is the inductive energy of a flux quantum, n is the fluxoid number in the loop. Here

$$E_S = a\frac{l}{\xi} k_B T_c \frac{R_q}{R_\xi} \exp(-b\frac{R_q}{R_\xi}), \tag{2.34}$$

is the quantum phase slip energy[71], with ξ the coherence length, l the length of wire and a and b constants of order one. $R_q = \frac{h}{4e^2}$ is the resistance quantum and $R_\xi = R_n \frac{\xi}{l}$ is the normal resistance R_n of the wire over one coherence length. From this we see that QPS nanowires are fabricated from disordered superconducting thin films, that is, those for which R_ξ is large. Qubits based on QPS have subsequently been demonstrated experimentally through microwave spectroscopy

of InOx[72] and NbN[73]-based loops. Figure 2.9 shows the result of microwave spectroscopy of an InOx QPS flux qubit, which demonstrates the avoided crossing near half flux due to coupling between adjacent flux states.

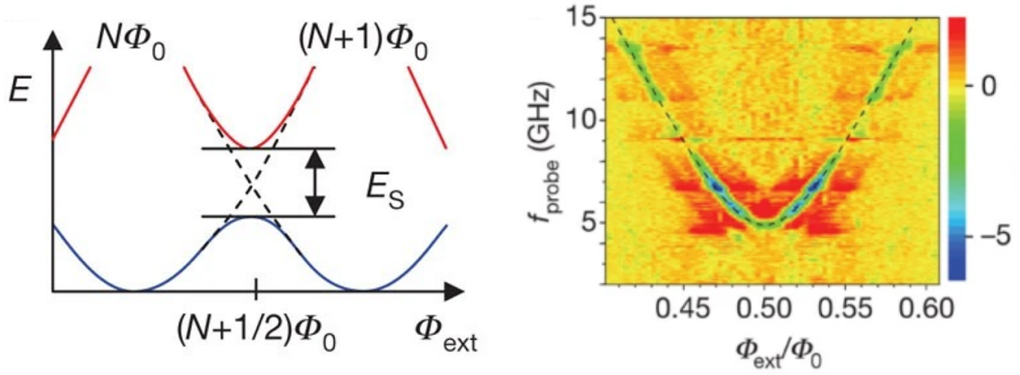

(a) (b)

Figure 2.9: (a) The energy spectrum of the QPS flux qubit. (b) Two-tone spectroscopy data with the expected energy splitting at $\frac{\Phi_{ext}}{\Phi_0} = 0.5$ due to quantum phase slips induced by the nanowire. Figures from [72].

The behaviour is dual to the CPB, where instead of the number of Cooper pairs, n labels the fluxoid number in the loop. Comparisons like this inspired the treatment of the QPS nanowire[74] as a superconducting circuit element dual to the JJ, with many JJ circuits having nanowire-based counterparts. The QPS junction has insulating behaviour up to a critical voltage, leading to a constitutive relation analogous to the first Josephson equation[74][57],

$$V = V_c \sin(2\pi q), \tag{2.35}$$

where $q = \frac{Q}{2e}$ is the normalised charge difference across the nanowire and $V_c = \frac{2\pi E_s}{2e}$ is the critical voltage. Analogous to the Josephson inductance, a QPS nanowire has capacitance

$$C_{NW} = \frac{e}{\pi V_c \cos 2\pi q}, \tag{2.36}$$

that is periodic in q.

Transport measurements have also demonstrated the duality, with IV curves[75][76][77] and constant current steps under microwave irradiation[78]. The dual to the SQUID has also been demonstrated in the QPS transistor[79][80] and QPS flux qubits for voltage-controllable phase-slip amplitudes[81]. Figure 2.10 shows a QPS transistor where the diamond-shaped element label is the symbol for a QPS nanowire. Figure 2.10b shows the dual Josephson relation, with the inset demonstrating gate-voltage tuneability for different bias voltages across the device.

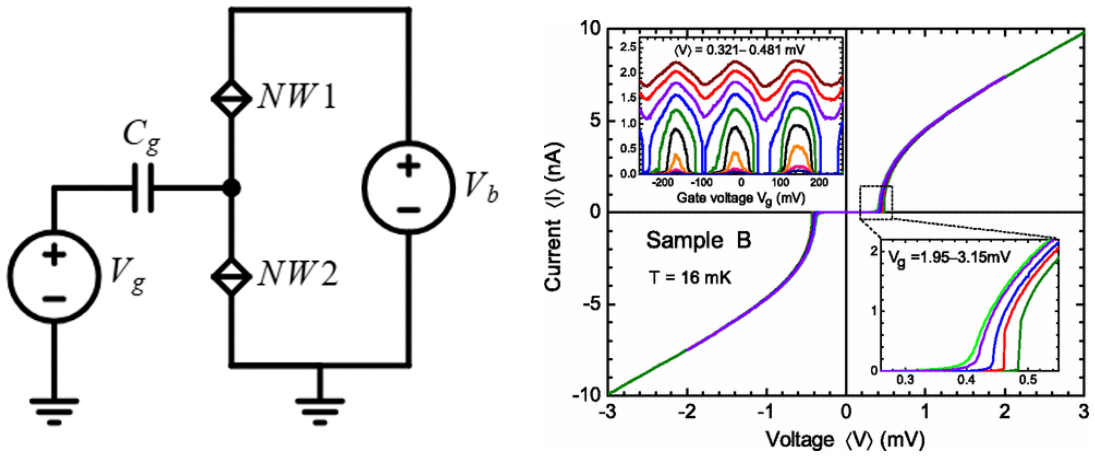

(a) (b)

Figure 2.10: (a) Device structure of the QPS transistor adapted from [79] showing the gate and bias voltage arrangement. The diamond-shaped element labelled NW1,2 is the symbol for a QPS nanowire. (b) IV characteristics from [79]. Inset shows gate voltage dependence for different bias voltages V_b.

2.3.1 Chapter Summary

To summarize, in this chapter we have introduced the theory necessary to understand circuit elements used to build superconducting and quantum circuits. First, we described the London equations, an early phenomenological model which sought to explain the vanishing electrical resistance and the expulsion of magnetic fields within the body of a superconductor. We also briefly highlighted the microscopic theory which governs superconductivity, BCS theory, which posits that the superconducting state is a quantum-mechanical ground state, consisting of paired electrons called Cooper pairs. This state is a condensate, meaning a large number of Cooper pairs are described by a single wavefunction throughout a superconductor. This is corroborated by the observations of macroscopic quantum phenomena, such as flux quantization in a superconducting loop.

We then discussed the superconducting tunnel barrier—the Josephson junction (JJ), in the classical regime, where the phase difference across the superconducting barrier was treated as a classical variable. Properties associated with classical junctions are the DC- and AC- Josephson effects, Shapiro steps and the nonlinear Josephson inductance. The RCSJ model governing practical junctions was also discussed. From the constitutive relations, we explained the behaviours of two types of superconducting quantum interference devices (SQUIDs). Next, we saw that a complete quantum treatment was needed to explain the energy spectra of two quantum circuits, the Cooper Pair Box (CPB) and flux qubit.

Last but not least, we introduced the superconducting nanowire, which shows increased resistance below the critical temperature. The appearance of a finite voltage is due to phase slips events, changes in the phase somewhere along the wire by $\pm 2\pi$, which can occur by thermal activation or quantum tunnelling. Far below T_c when quantum phase-slips (QPS) proliferate, the behaviour is dual to the tunnelling of Cooper pairs in JJs, with an ideal insulating behaviour. We further demonstrated this duality with the QPS flux qubit, which behaves like a CPB and the QPS transistor, dual to the SQUID.

2.3 Quantum Phase-Slip Nanowires

Equipped with the superconducting device theory of the circuits, in the next chapter, we motivate the work presented in this thesis. We start with motivating the first part of the thesis, which concerns the implementation of YY interactions between two flux qubits. This is in the context of quantum annealing, which we will give an overview of, and provide a review of the qubit coupling methods currently available in commercial annealers. As we shall see, the nonlinear capacitance of the JJ in the charging regime is a good candidate for a coupler providing the interactions desired. Next, we give a background review of the next part of the thesis, which is an experimental study for a new prototype of a QPS-based parametric amplifier, utilizing the nonlinear capacitance of the QPS nanowire. Some basic theory of parametric amplification is introduced and we give a short survey of superconducting parametric amplifiers.

Chapter 3

Motivation and Review

Having introduced the constitutive relations for Josephson junctions and quantum phase slip nanowires and some superconducting and quantum circuits, here we motivate the work discussed in the rest of the thesis. First, we consider the application of the JJ in the $E_c \gtrsim E_J$ regime, in the context of quantum annealing (QA). We will describe QA and its physical realisation in superconducting electronics and discuss the current state of the art in annealing hardware. We then provide background for using JJs in the charging regime as novel tuneable coupling elements in a quantum annealer. Next, we motivate the experimental study of the QPS nanowire parametric amplifier (paramp). We'll present the principles of parametric amplification and discuss different modes of operation in paramps that have been explored in the literature.

3.1 YY coupler for Quantum Annealing

3.1.1 Quantum Annealing

One exciting application of superconducting quantum devices arises from exploiting the manipulation of quantum states as methods of computing and information processing. Quantum annealing (QA) is a proposed protocol for solving optimization problems. The idea was first conceived as a variation of classical simulated

annealing, utilizing quantum fluctuations in place of thermal fluctuations in search for the global minima[82][83]. QA is based on the Ising Model, which is a physical model of ferromagnetism involving interactions between magnetic dipoles. In such systems, finding the configuration of spins which minimizes the total energy is difficult. In fact, it has been shown that there exists polynomial-time mappings from the Ising model to NP-complete problems[84]. The implementation of QA is thus highly desirable as a test-bed for encoding and potentially solving these computationally difficult problems.

In QA, one has in mind a problem which can be encoded as a Hamiltonian, which can be represented in our quantum annealer where the solution is encoded in the ground state of the Hamiltonian. In an optimization problem, the goal is to find the arguments of a given function which leads to the minimum of that function. In QA, the Hamiltonian of the system plays the role of the function, and states play the role of the arguments. The protocol relies on the adiabatic theorem in quantum mechanics, which asserts that when a quantum mechanical system is in its ground state, a varying Hamiltonian will lead the state to evolve so that it remains in the ground state provided the variation is slow enough. With a quantum annealer, the idea is to initialize the system in a trivial Hamiltonian, with a known ground state which can be prepared a priori, and with the controls on the annealer, change this Hamiltonian so that it reaches the problem Hamiltonian which encodes the problem of interest. This is operated so that the final state remains in the ground state, and the solution is found by reading out this state.

Commercial quantum annealers, for instance the processors manufactured by D-Wave, are made up of a network of superconducting flux qubits. The interaction between the qubits are mediated by couplers which can be sign and magnitude tuneable. The Hamiltonian implemented is the Transverse-field Ising Model

$$H(s) = H_i(s) + H_p(s) = \underbrace{A(s)\left[\sum_i \sigma_x^i\right]}_{H_i(s)} + \underbrace{B(s)\left[\sum_i h_i\sigma_z^i + \sum_{i<j} J_{i,j}\sigma_z^i\sigma_z^j\right]}_{H_p(s)}, \quad (3.1)$$

where $s = \frac{t}{t_f}$ is a dimensionless time parameter for a total annealing time t_f, and H_i and H_p are the initial and problem Hamiltonians respectively. At $t = 0$, the annealer is configured to give $A(0) \gg B(0)$ which initializes the system in the trivial ground state, where every qubit is in the superposition state $|-\rangle = \frac{1}{\sqrt{2}}(|\uparrow\rangle - |\downarrow\rangle)$. The Hamiltonian is then varied continuously throughout the annealing process, until in the end $A(1) \ll B(1)$ and the annealer is in the ground state of the problem Hamiltonian, provided the evolution is adiabatic.

3.1.2 Hamiltonian Engineering

As the two computational basis states are the persistent current states with circulating currents I_{p1} and I_{p2}, the ZZ coupling is determined by a mutual inductance M which gives rise to interaction energy $J = MI_{p1}I_{p2}$. In order to implement a tuneable mutual inductance as needed for QA, the interaction is mediated through an additional loop containing one or more JJs. One such implementation[85] by Harris et al. is shown in Figure 3.1. The circuit consists of three compound junction RF SQUIDs, where the single JJ of a simple RF SQUID has been replaced by a DC SQUID, allowing in-situ tuning of the Josephson energy. Two of these RF SQUIDs are operated in the double-well regime as flux qubits, and they are both coupled together inductively indirectly via the third SQUID, which is designed to be in the monostable regime with screening parameter $\beta_L < 1$.

When the qubits are coupled to the coupler loop of inductance L, through fixed mutual inductances M, the result is an effective mutual inductance $\tilde{M} = \frac{M^2}{L}$. With inclusion of a JJ, as in the case of the RF SQUID coupler[86] [87][88], the effective mutual inductance is altered to $\tilde{M} = M^2\chi$ where $\chi = \frac{dI_p^c}{d\Phi_{ext}^c}$ is the susceptibility

of the coupler, which determines the screening current I_p^c that circulates in the coupler loop when flux Φ_{ext}^c is applied to it.

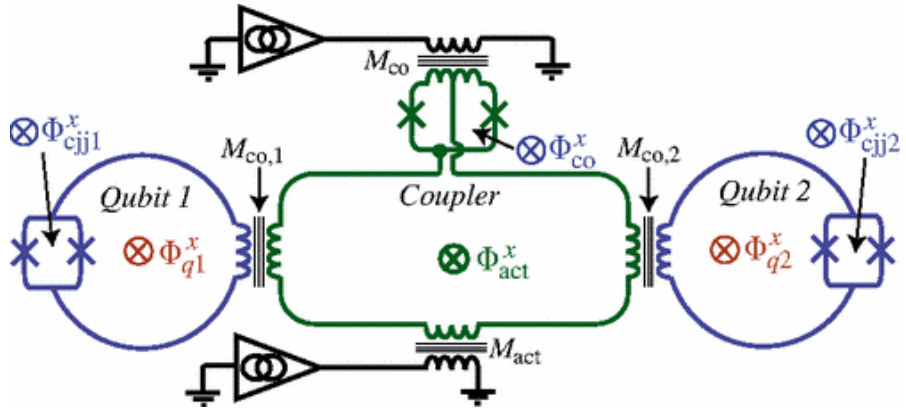

(a)

Figure 3.1: (a) Tuneable inductive coupling of two flux qubits from [85]. The coupler is an rf SQUID operated in the monostable regime with screening parameter $\beta_L < 1$.

While this approach has been fruitful in the study of Ising spin glasses, demonstrating quantum dynamics following the evolution of the Schrodinger equation, there remains scope for the capability of annealers to be expanded, particular since the computation represented by (3.1) is known to not be universal. This limitation can be overcome by the inclusion of different coupling terms, such as terms involving $\sigma_x^i\sigma_x^j$ and $\sigma_y^i\sigma_y^j$, which would allow an annealer to simulate arbitrary Hamiltonians[89]. The introduction of these terms also makes the Hamiltonian nonstoquastic, which causes particular difficulty for classical solvers[90], an area where quantum annealers may be able to prove a computational advantage[91][92].

To engineer the new interaction terms, a natural candidate comes from coupling the charge degrees of freedom between flux qubits since $\hat{Q} \propto \sigma_y$. YY interactions have been implemented in [93], where it was demonstrated on flux qubits coupled with a capacitor. Although this makes the Hamiltonian nonstoquastic, a tune-

able implementation is needed to make the term programmable. Such a tuneable differential capacitance was considered by Averin and Bruder for coupling charge qubits[94], based on a small JJ in parallel with the qubits. The JJ is in the regime $E_C \gtrsim E_J$, similar to a Cooper Pair Box (CPB), but with a much higher excitation energy so that it remains in the ground state and the coupler excited states do not mix with the qubit computational subspace. Just like a CPB, a gate voltage can be applied to it which periodically modulates the ground state energy, leading to an effective capacitance $C_{eff} \approx \frac{dQ}{dV}$[95].

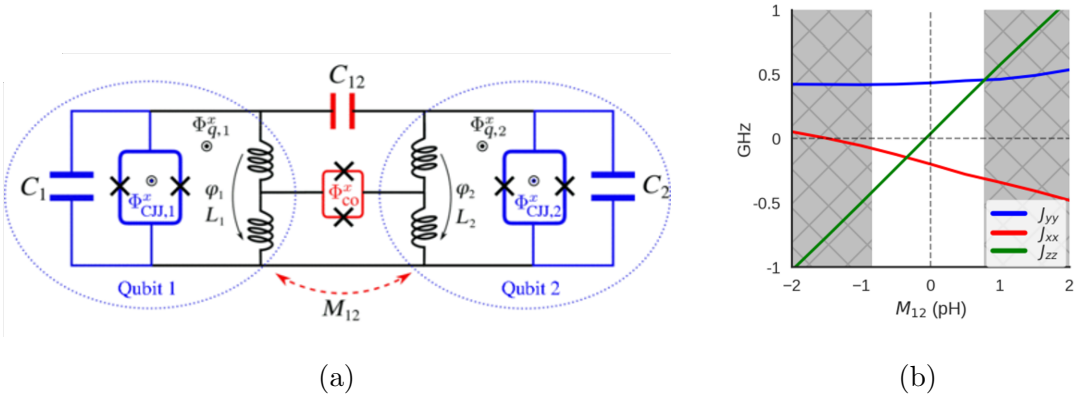

(a) (b)

Figure 3.2: (a) Tuneable inductive and fixed capacitive coupling of two flux qubits. (b) Interaction terms in the two qubit Hamiltonian extracted from measurements. From [93].

Although analyses of the effective capacitance of a CPB coupler have been reported in the literature, they have predominantly treated the case of mediated coupling between charge qubits. The situation where the coupler mediates the coupling between flux qubits is not *a priori* clear. Furthermore, the relation between the circuit parameters and the qubit Hamiltonian is not an obvious one, so one must in general resort to numerical methods. This is the subject of the next chapter where we consider numerical simulations of capacitively coupled flux qubits.

3.2 QPS Nanowire Parametric Amplifier

Before we move on to the next chapter, we will motivate the application of the QPS nanowire in the design for a parametric amplifier (paramp) for the second part of this thesis. With the growth of superconducting electronics as a promising platform for quantum information and computing, ultra-low-noise amplifiers have become indispensable components as the first stage of amplification at the output end of a measurement system. They are operated at cryogenic temperatures ($\approx$10 mK) and at the core of such an amplifier is a non-linear superconducting element. To this end, superconducting paramp designs have so far been based on the nonlinearity of the inductance of a JJ[96][97] or high-kinetic inductance films[98][99][100]. Recent progress in the duality of QPS nanowire-based circuits with their JJ counterparts, suggest paramp designs based on the non-linear capacitance of the QPS nanowire. This is an attractive alternative since nanowires have a simpler, single-layer fabrication process compared to JJs, which requires precise engineering of the oxide barrier. The high impedance of nanowire-based devices could also prove complimentary to JJ-based electronics, opening the possibility of using both types of paramp together depending on application, or even allowing hybrid designs containing both JJs and nanowires to be realised.

3.2.1 Parametric Amplification

The classic example of this parametric amplification is a child on a swing. By changing the position of their legs at specific points of the motion, the child modulates the natural frequency of the swing. By doing so at a specific frequency, the oscillations are amplified. The same principle applies in electronics, where a parametric amplifier consists of a resonance circuit which achieves gain by either varying the inductance or capacitance.

Here we may make the distinction between two general types of superconducting parametric amplifiers found in the literature. The first type is a parametric

oscillator where the nonlinear element is modulated directly, through a separate control line. The amplitude of a signal obeys

$$\ddot{x} + 2\gamma\dot{x} + \omega^2(t)x = F\cos\omega_s t, \tag{3.2}$$

where $\omega(t)$ is a time-dependent natural frequency of the oscillator controlled by the pump tone of frequency ω_p, and for small perturbations $\omega^2(t) = \omega_0^2(1 + A\sin\omega_p t)$. The solutions to this equation exhibit gain for the signal, with maximum gain occuring when $\omega_p = 2\omega_s$[101]. Furthermore, the system also generates sum and difference frequencies $\omega_i^{\pm} = \omega_p \pm \omega_s$. The difference frequency is called the idler and is also amplified in this process when it falls within the resonance linewidth[102]. The mixing process in this mode of operation is known as three-wave mixing (3WM), as depicted in Figure 3.3a.

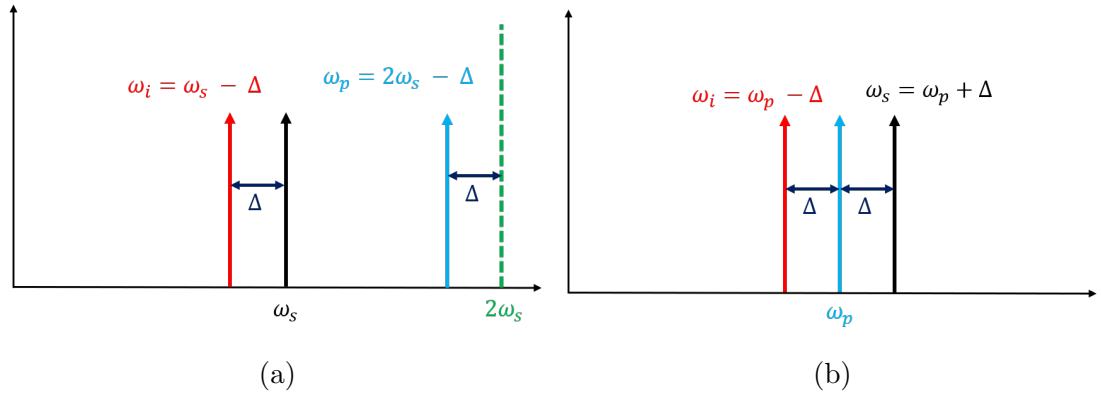

Figure 3.3: Figures show the frequency relationships in (a) three- and (b) four-wave mixing processes. The signal is depicted in black, the pump in blue and idler in red.

The second type of paramp uses the intrinsic nonlinearity of an element in the resonator to generate amplification. These devices do not use dedicated lines which independently drive the nonlinear element, but instead operate by pumping

the nonlinear resonator near its resonance frequency. Nonlinear driven oscillators of this kind are described by the Duffing Equation

$$\ddot{x} + 2\gamma\dot{x} + \omega_0^2 x + \beta x^3 = F\cos\omega t, \tag{3.3}$$

where β is a parameter which determines the degree of nonlinearity. Approximate solutions to the differential equations may be found iteratively[103] about the harmonic solution $x_0 = A\cos(\omega t - \phi)$ by successive integration to obtain a series containing harmonics of ω. It may be shown the amplitude and phase of the fundamental is related to the driving amplitude by the relation[104]

$$\begin{aligned} F^2 &= \left((\omega_0^2 - \omega^2)A + \frac{3}{4}\beta A^3\right)^2 + (2\gamma\omega A)^2, \\ \tan\phi &= \frac{2\gamma\omega A}{(\omega_0^2 - \omega^2)A + \frac{3}{4}\beta A^3}, \end{aligned} \tag{3.4}$$

The amplitude can be solved as a polynomial in either ω or A to obtain the frequency response of the oscillator being driven at ω_0. The solution to equation 3.4 is plotted in Figure 3.4. As the drive amplitude increases, the minimum of amplitude response starts leaning towards the left until eventually at a critical point, $F_c = \sqrt{\frac{256\gamma^3}{9\sqrt{3}}\frac{\omega_0^3}{|\beta|}}$[104], the oscillation amplitude becomes multivalued.

Furthermore, under the application of two tones, (a pump x_p, and a signal x_s, which is of much smaller amplitude) and expanding (3.3) to first order in x_s, one can show that the signal obeys

$$\ddot{x}_s + 2\gamma\dot{x}_s + \omega_1^2(A,t)x_s = F_s\cos\omega_s t, \tag{3.5}$$

where $\omega_1^2(A_p,t) = \omega_0^2\left(1 - \frac{A_p^2}{4}\right)\left[1 - \frac{\frac{A_p^2}{4}}{1-\frac{A_p^2}{4}}\cos(2\omega_p t - 2\phi)\right]$, where ω_p is the frequency of the pump. This can be recognized as the equation for a parametric oscillator with $\omega^2(t) = \omega_0^2(1 + f_0\sin(2\omega_p t))$. In this case, the amplification occurs when $\omega_p = \omega_s$ and harmonics are generated at sum and difference frequencies

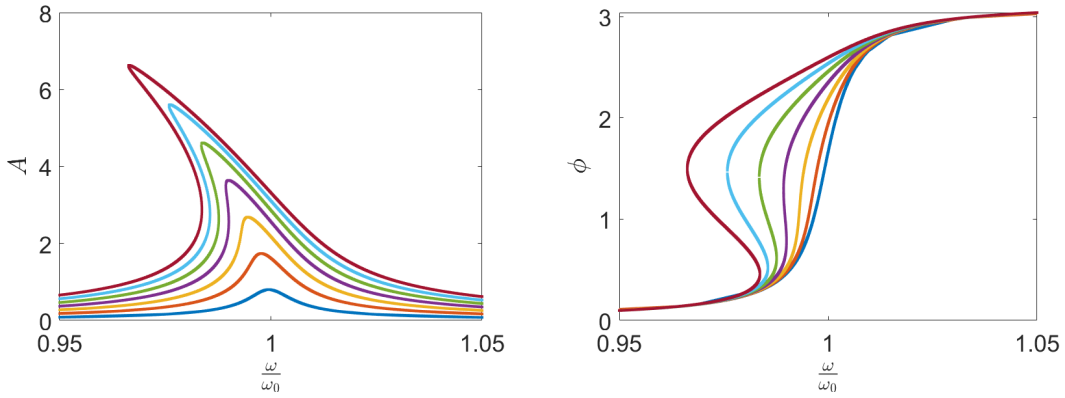

Figure 3.4: The amplitude A and phase ϕ of the driven nonlinear oscillator response with normalized parameters $\frac{\beta}{\omega_0^2} = -0.005$, $\frac{\gamma}{\omega_0} = 0.005$ for equally spaced drive amplitude F from $0.25F_c$ to $2F_c$.

$\omega_\pm = 2\omega_p \pm \omega_s$ which is known as degenerate four-wave mixing (4WM), as shown in Figure 3.3b.

Devices using both modes of operation can be found in the literature and in practice, sometimes with both capabilities on the same device, though 3WM-type devices are typically more complex due to needing specific biasing arrangements. SQUID-based Josephson Parametric Amplifier (JPA)[96][105] are devices which can be operated in both modes, with a simple design, consisting of a resonator and a SQUID loop. In the 3WM mode, the DC SQUID provides the nonlinear inductance tuneable by flux. The circuit diagram of this device is shown in Figure 3.5, where a separate pump line is used to bias and modulate the SQUID inductance.

JPAs have seen widespread applications due to their quantum-limited noise performance[106] at over 20 dB gain, with many later designs improving the amplifier's performance in bandwidth and saturation power. These strategies include

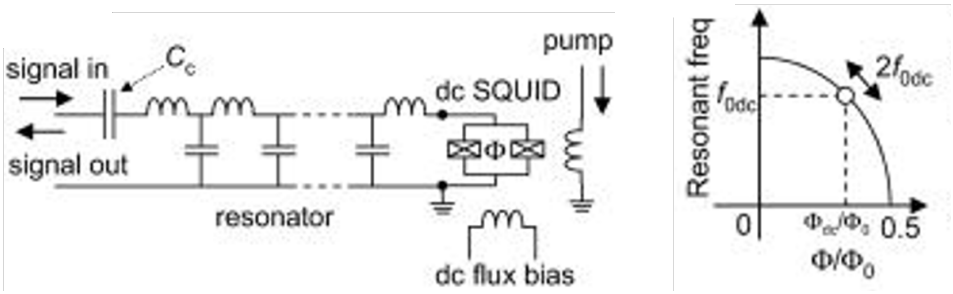

(a) (b)

Figure 3.5: (a) Flux-driven Josephson Parametric Amplifier (JPA) consisting of a DC SQUID at the end of a resonator. A separate pump line is used to modulate the nonlinear inductance. (b) Flux response of the resonance frequency. The paramp is operated by choosing a fixed bias Φ_{dc} and applying pump at twice the natural frequency of the resonator f_{0dc}. From [105].

using SQUID arrays to make the center frequency tuneable[107] and transforming the JPA input impedance[108]. A recent approach[109] using a combination of these techniques demonstrated promising results towards multiplexed readout of quantum processors. Quantum-limited amplification is needed for dispersive readout of superconducting qubits due to the low microwave probe powers required to mitigate transitions out of the qubit's two-level subspace[110]. The JPA has excellent gain and noise performance, and with its simplicity in fabrication, it is an attractive choice for such an application. On the other hand, JPAs typically suffer from having low saturation powers, at around the -100 dBm level[111] and narrow bandwidths on the order of 100 MHz.

A popular JJ-based distributed amplifier is the Josephson travelling wave parametric amplifier (JTWPAs)[112][113] [114]. It offers wideband amplification over several GHz, but at the cost of increased noise. JTWPAs contain thousands of JJs in a series array and requires periodic phase matching elements[115][116] to achieve optimal gain. The complexity of the circuit also makes the design and fabrication challenging.

3.2 QPS Nanowire Parametric Amplifier

While the developments in JJ-based devices have had the benefit of the maturity of JJ technology, QPS-based devices have only emerged relatively recently. Because of this paramps based on the nonlinear capacitance of the QPS nanowire have so far remained unexplored. With QPS devices exhibiting higher input impedance and with the relative ease of fabrication, they would be a valuable new tool in the superconducting paramp design toolbox. This is the topic of Chapter 6 in our experimental study of single-nanowire and gated two-nanowire nonlinear resonators.

Chapter 4

Numerical Simulations of Superconducting Quantum Circuits

As we have mentioned in the previous chapter, an implementation of a tuneable YY interaction could enhance the performance and extend the capabilities of quantum annealers. We also showed in the introduction that for flux qubits, a YY interaction term in the qubit Hamiltonian arises from the coupling of their charge degrees of freedom. In this chapter, we focus on the study of a variable capacitor first considered for the controlled coupling of charge qubits by Averin and Bruder[94] applied to flux qubits. The coupler has the same device structure as a Cooper Pair Box (CPB), that is, it has a superconducting island shunted to ground through a Josephson junction (JJ) in the charging regime ($E_C \geqslant E_J$).

To find the circuit dependences of the qubit Hamiltonian, we use a numerical simulation and qubit reduction method discussed by Consani and Warburton[54]. First, we illustrate the method using two flux qubits coupled by a fixed capacitor and show that the capacitive coupling gives rise to a YY interaction term in the qubit Hamiltonian. Next, we simulate the full circuit where the two flux qubits are coupled by the voltage-tuneable capacitor. Using the simulated results, we

designed a physical chip layout and discuss experimental methods that can be used to verify the simulations presented here.

4.1 Two Flux Qubits Coupled by a Capacitor

4.1.1 Circuit Hamiltonian

To describe the method used for numerical simulation, we begin by considering the circuit consisting of two flux qubits coupled by a fixed capacitor shown in Figure 4.1. We derive the Hamiltonian of the circuit with the help of quantum network theory[37][38], which describes the quantum behaviour of superconducting circuits, analogous to nodal analysis in electrical circuits.

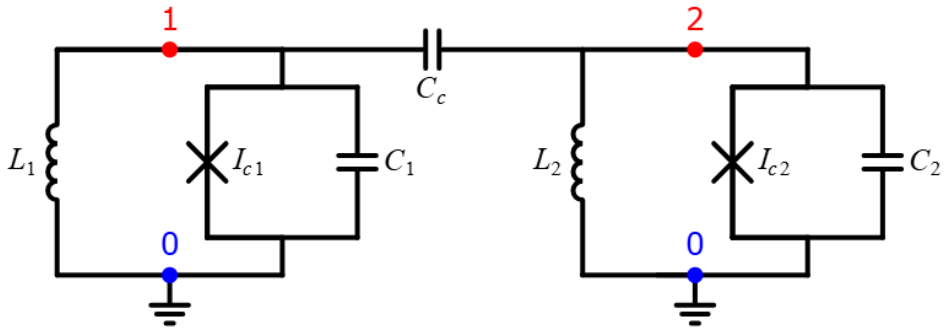

Figure 4.1: Two flux qubits coupled by a fixed capacitor C_c.

Here each node is assigned a node flux, given by the time integral of the voltage $\Phi = \int_0^t V(t')dt'$, which plays the role of a position coordinate in classical mechanics[38]. The kinetic energy term in the circuit Lagrangian is then

$$\begin{aligned} T &= \frac{1}{2}\dot{\vec{\Phi}}^T \boldsymbol{C} \dot{\vec{\Phi}} \\ &= \frac{C_1\dot{\Phi}_1^2}{2} + \frac{C_2\dot{\Phi}_2^2}{2} + \frac{C_c(\dot{\Phi}_1 - \dot{\Phi}_2)^2}{2} \end{aligned} \tag{4.1}$$

where

$$\boldsymbol{C} = \begin{pmatrix} C_1 + C_c & -C_c \\ -C_c & C_2 + C_c \end{pmatrix} \tag{4.2}$$

is the capacitance matrix of the circuit. The potential energy terms are given by

$$\begin{aligned} U(\Phi_1, \Phi_2) =& \frac{{\Phi_1}^2}{2L_1} + \frac{{\Phi_2}^2}{2L_2} - E_{J1}\cos\left(\frac{\hbar}{2e}(\Phi_1 + \Phi_{ext,1})\right) \\ & - E_{J2}\cos\left(\frac{\hbar}{2e}(\Phi_2 + \Phi_{ext,2})\right)). \end{aligned} \tag{4.3}$$

The conjugate variable to the node flux, the node charge can be obtained by $\vec{Q} = \boldsymbol{C}\dot{\vec{\Phi}}$, which satisfies the canonical commutation relations, $[\Phi_i, Q_j] = i\hbar\delta_{i,j}$. The Hamiltonian can then be constructed by $H(\vec{Q}, \vec{\Phi}) = T(\vec{\Phi}(\vec{Q})) - U(\vec{\Phi})$, which is, for the circuit we are considering,

$$H = \frac{1}{2}\vec{Q}^T\boldsymbol{C}^{-1}\vec{Q} + U(\Phi_1, \Phi_2). \tag{4.4}$$

The properties of this superconducting circuit can then be obtained by solving this Hamiltonian numerically. We may do so in the occupation number operator basis, which represents the operators as

$$\hat{Q}_i = i\sqrt{\frac{\hbar}{2Z_i}}(\hat{a}_i - \hat{a}_i^\dagger) \tag{4.5}$$

$$\hat{\Phi}_i = \sqrt{\frac{\hbar Z_i}{2}}(\hat{a}_i + \hat{a}_i^\dagger) \tag{4.6}$$

$$\hat{a}_i = \begin{bmatrix} 0 & \sqrt{1} & 0 & 0 & \dots & 0 & 0 \\ 0 & 0 & \sqrt{2} & 0 & \dots & 0 & 0 \\ 0 & 0 & 0 & \sqrt{3} & \dots & 0 & 0 \\ \vdots & \vdots & \vdots & \vdots & \ddots & \vdots & \vdots \\ 0 & 0 & 0 & 0 & \dots & \sqrt{n-2} & 0 \\ 0 & 0 & 0 & 0 & \dots & 0 & \sqrt{n-1} \\ 0 & 0 & 0 & 0 & \dots & 0 & 0 \end{bmatrix} \tag{4.7}$$

where $Z_i = \sqrt{\frac{\boldsymbol{C}^{-1}_{i,i}}{\boldsymbol{L}^{-1}_{i,i}}}$ is the characteristic impedance and $\hat{a}_i$ is the truncated lowering operator of the i-th harmonic oscillator mode.

4.1.2 Effective Qubit Hamiltonian

When considering superconducting circuits as being composed of qubits and coupling elements, it is useful to map the full circuit Hamiltonian to a low dimensional qubit Hamiltonian where their dynamics effectively take place. One attractive approach is using the Schrieffer-Wolff (SW) method[117][54] which involves calculating a unitary transformation which separates the high and low-energy subspaces. This is particularly well suited in numerical simulations for calculating qubit properties as a function of circuit parameters or bias conditions.

A circuit Hamiltonian can be decomposed into an interacting and non-interacting part, $\hat{H}_{circ} = \hat{H}_0 + \hat{H}_{int}$. In the previous example,

$$\hat{H}_0 = \frac{\hat{Q_1}^2}{2C'_{11}} + \frac{\hat{Q_2}^2}{2C'_{22}} + U(\Phi_1, \Phi_2), \tag{4.8}$$

where $C'_{ii} = \frac{1}{(\boldsymbol{C}^{-1})_{ii}}$ is the reciprocal of the i-th diagonal entry in the inverse capacitance matrix. The interacting terms arise due to the off-diagonal elements $C'_{ij} = \frac{1}{(\boldsymbol{C}^{-1})_{ij}}$,

$$\hat{H}_{int} = \frac{\hat{Q}_1 \hat{Q}_2}{C'_{12}}. \tag{4.9}$$

By diagonalizing $\hat{H}_0$ and $\hat{H}_{int}$, we can construct $\hat{P}_0 = \sum_0^{2^N-1} |E_i^{(0)}\rangle\langle E_i^{(0)}|$ and $\hat{P} = \sum_0^{2^N-1} |E_i\rangle\langle E_i|$ which are the projectors on the low-energy subspaces of $\hat{H}_0$ and $\hat{H}_{circ}$ respectively. The Schrieffer-Wolff transformation is then given by[117][54]

$$\hat{U} = \sqrt{(2\hat{P}_0 - \hat{\mathbb{I}})(2\hat{P} - \hat{\mathbb{I}})}, \tag{4.10}$$

which has the property that

$$\hat{H}_q = \hat{P}_0 \hat{U} \hat{H}_{circ} \hat{U}^\dagger \hat{P}_0 \tag{4.11}$$

is the effective qubit Hamiltonian. For the two qubit circuits considered in this chapter, we extract the four lowest energy levels from the full circuit Hamiltonian using this method. The effective qubit Hamiltonian can then be represented in the computational basis—the two persistent current states of the flux qubit—which is a linear combination of the energy eigenbasis[54]. The general two qubit Hamiltonian is then

$$\hat{H}_q = \sum_{i,j} h_{ij} \hat{\sigma}_i \hat{\sigma}_j \tag{4.12}$$

where $i, j = I, x, y, z$ and $\hat{\sigma}_i$ are the Pauli matrices. We refer to coefficients $h_{I(i\neq I)}$ and $h_{(i\neq I)I}$ as local terms, and $h_{(i\neq I)(i\neq I)}$ as interaction terms.

4.1.3 Simulation Results

We perform the numerical simulation of two flux qubits coupled by a capacitor. The flux qubits are identical and biased at half flux. The value of the coupling capacitor is changed from -5 fF to 5 fF, and the low energy spectrum is plotted in Figure 4.2. The solid coloured lines are from diagonalizing the full circuit Hamiltonian (4.4), while the black dashed lines are the eigenvalues from the qubit Hamiltonian, reconstructed from the Pauli coefficients shown in Figure 4.3. As expected, in the absence of any qubit interactions, the first excited state of the system is degenerate. As the magnitude of capacitance is increased, the energy levels split and the splitting is determined by the coupling strength. The coupling also has a loading effect on each qubit, manifesting as the changing X local term in the qubit Hamiltonian as shown in Figure 4.3a. The dominant effect of the capacitive coupling is to introduce a YY interaction as we expect, with the strength proportional to the value of the capacitance, while also introducing a much smaller XX interaction. Figure 4.4 shows a comparison between the YY term from the SW method and an analytical treatment using the two-level approximation from Chapter 2. Under this approximation, the charge operator is $\hat{Q} \approx |\langle E_0| \hat{Q} |E_1\rangle| \hat{\sigma}_y$, giving $h_{YY} \approx \frac{|\langle E_0^{(1)}|\hat{Q}_1|E_1^{(1)}\rangle\langle E_0^{(2)}|\hat{Q}_2|E_1^{(2)}\rangle|}{C_c}$, which agrees well with our numerical simulation here.

Thus using this method we are able to design qubit circuits by determining the appropriate values for the circuit components to obtain the desired qubit Hamiltonian. While in this case we determine the Pauli coefficients as a function of a fixed capacitance, the method also allows us to incorporate coupling elements including Josephson junctions with varying voltage biases. This is the subject of the next section, where we simulate a capacitive coupler which is tuneable in-situ with a voltage bias.

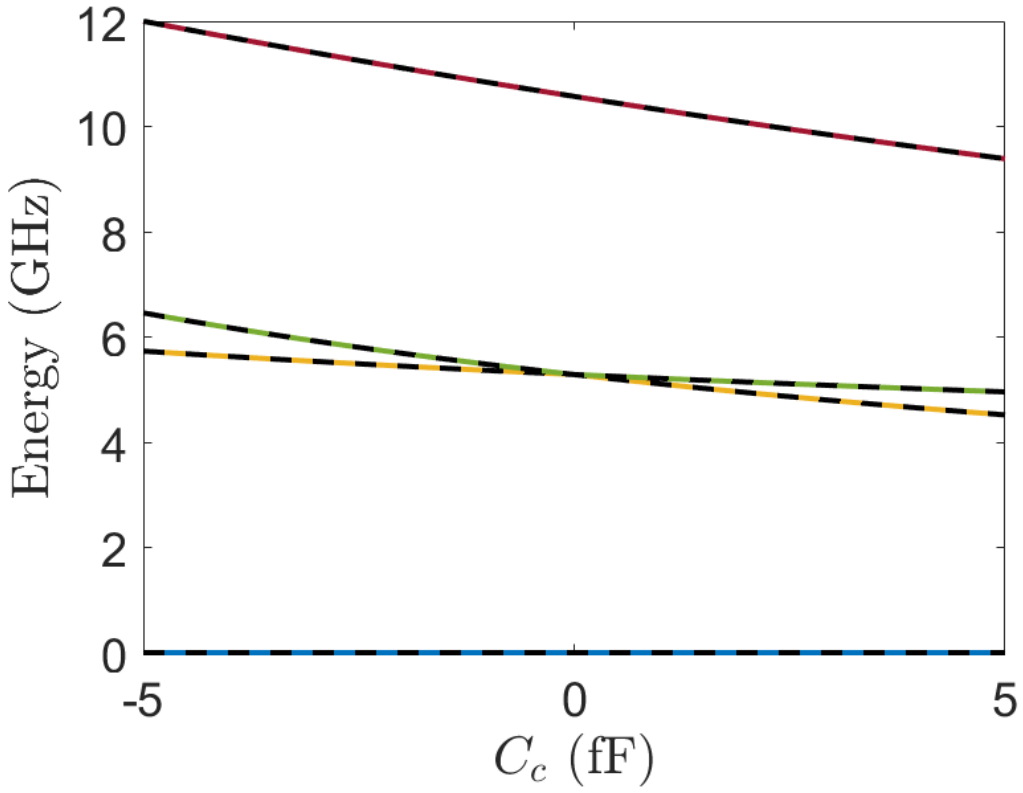

Figure 4.2: The energy spectrum of two flux qubits coupled by a fixed capacitor. The value of the coupling capacitance C_c is varied in the simulation. Coloured lines are the result of diagonalization of the full circuit Hamiltonian (4.4), while the dashed black lines are obtained from the reduced qubit Hamiltonian. Qubit parameters are $L = 300\ pH$, $C = 43\ fF$ and $I_c = 1.2\ \mu A$.

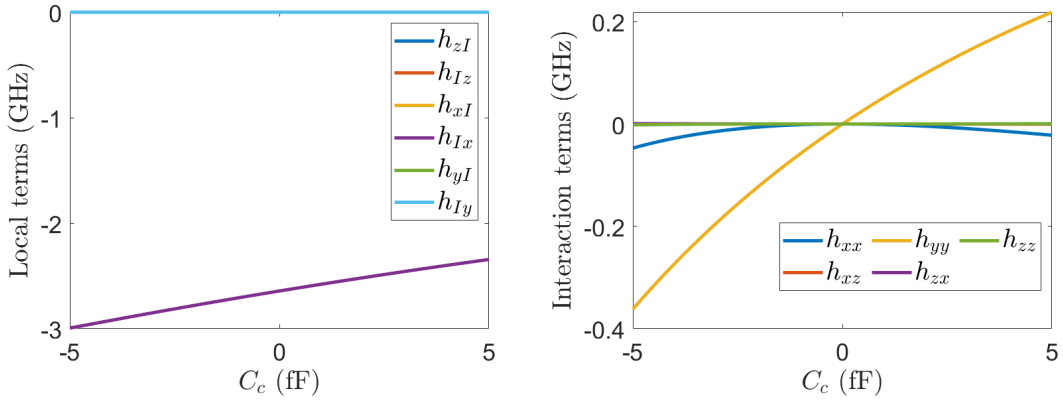

(a) (b)

Figure 4.3: Pauli coefficients for the two capacitively coupled flux qubits. (a) Local terms. (b) Interaction terms. Refer to caption of Figure 4.2 for device parameters. By symmetry of the circuit we have $h_{ij} = h_{ji}$ and some lines are stacked on top of each other. We have $h_{zI} = h_{yI} = h_{xz} = 0$ in these plots.

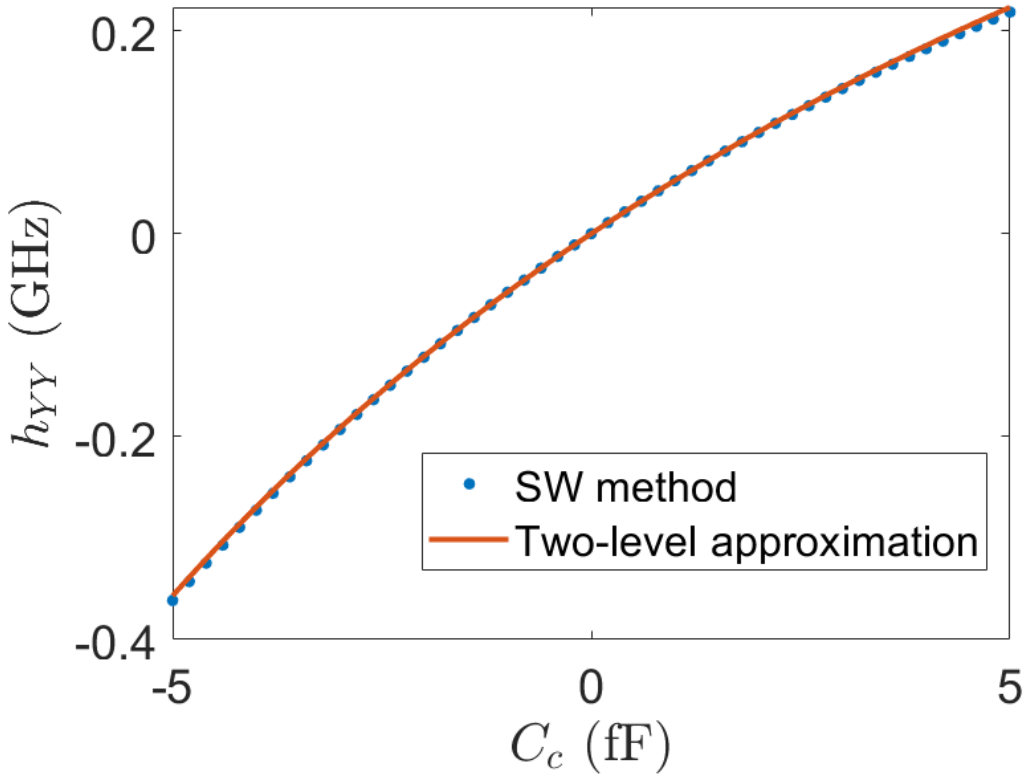

Figure 4.4: Plot of h_{YY} obtained using different methods. Blue points are from numerical simulation using SW reduction method, while orange line is from two-level approximation formula $h_{YY} \approx \frac{|\langle E_0^{(1)}|\hat{Q}_1|E_1^{(1)}\rangle\langle E_0^{(2)}|\hat{Q}_2|E_1^{(2)}\rangle|}{C_c}$.

4.1.4 Two Flux Qubits Coupled by the Tuneable YY Coupler

In this section, we consider the tuneable capacitive coupler, first analysed by Averin and Bruder for coupled charge qubits[94], as an implementation of a variable YY term in the qubit Hamiltonian for two flux qubits.

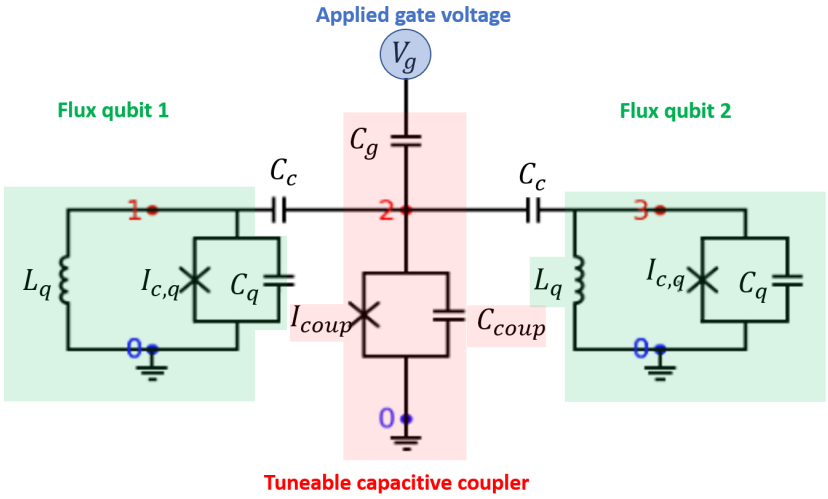

Figure 4.5: Two flux qubits coupled by a voltage-tuneable capacitive coupler. The coupler highlighted in red implements the functionality.

We simulate the circuit shown in Figure 4.5, which consists of two flux qubits each capacitively coupled to the proposed coupling element. The voltage of the island, on node two, can be varied through gate capacitor by an applied gate voltage. The Hamiltonian describing this circuit is

$$\begin{aligned} H =& \frac{{Q_1}^2}{2C'_{11}} + \frac{(Q_2 - Q_g)^2}{2C'_{22}} + \frac{{Q_3}^2}{2C'_{33}} + \frac{Q_1(Q_2 - Q_g)}{C'_{12}} + \frac{(Q_2 - Q_g)Q_3}{C'_{23}} + \frac{Q_1 Q_3}{C'_{13}} \\ & + \frac{{\Phi_1}^2}{2L_1} + \frac{{\Phi_3}^2}{2L_3} - E_{J1}\cos\left(\frac{\hbar}{2e}(\Phi_1 + \Phi_{ext,1})\right) - E_{J2}\cos\left(\frac{\hbar}{2e}(\Phi_2)\right) \\ & - E_{J3}\cos\left(\frac{\hbar}{2e}(\Phi_3 + \Phi_{ext,3})\right), \end{aligned} \tag{4.13}$$

where the subscripts on the operators label the node of the circuit, $Q_g = C_g V_g$ is the gate charge, and $C'_{ij} = \frac{1}{(\boldsymbol{C}^{-1})_{ij}}$, $(\boldsymbol{C}^{-1})_{ij}$ being the i,j-th element of the inverse capacitance matrix

$$\boldsymbol{C}^{-1} = \begin{pmatrix} C_q + C_c & -C_c & 0 \\ -C_c & C_{coup} + 2C_c & -C_c \\ 0 & -C_c & C_q + C_c \end{pmatrix}^{-1}. \tag{4.14}$$

The YY interaction must therefore arise from the term $\frac{Q_1 Q_3}{C'_{13}}$. But in order to maintain proper operation, we impose several design criteria. Firstly, the coupler is intended to remain in its ground state and its excited state does not participate during proper operation. Thus, we require the excitation energy of the coupler to be much higher than the qubit excitation energy. Since flux qubit excitation energies are typically engineered in the 5 - 8 GHz range, we would want our coupler excitation energy to be well above this, which we set to be at least 15 GHz. Secondly, the flux qubits in the simulations are designed with fixed screening parameter $\beta_L = \frac{E_J}{E_L} = 1.3$, which fixes the tunnel barrier height between the two potential wells of the RF SQUIDs to ensure that we remain in the double-well regime at all points in the simulation.

In normal operation, we expect the coupler to attain its maximum and minimum capacitances. To see this, we show the excitation energy of the coupler as a function of its Josephson energy, shown in Figure 4.6. In the charging regime

when $E_J \ll E_C$, the capacitance is given by $4e^2(\frac{\partial^2 E_g}{\partial Q_g^2})^{-1}$ [94], inversely proportional to the ground state curvature, which is largest at zero and half gate charge. In the cases we are considering where E_J and E_C of the coupler are on the same order however, this expression no longer holds and we must resort to numerical simulation. Nevertheless from these considerations we expect a tradeoff between the variability of the capacitance and the minimum gap of the coupler.

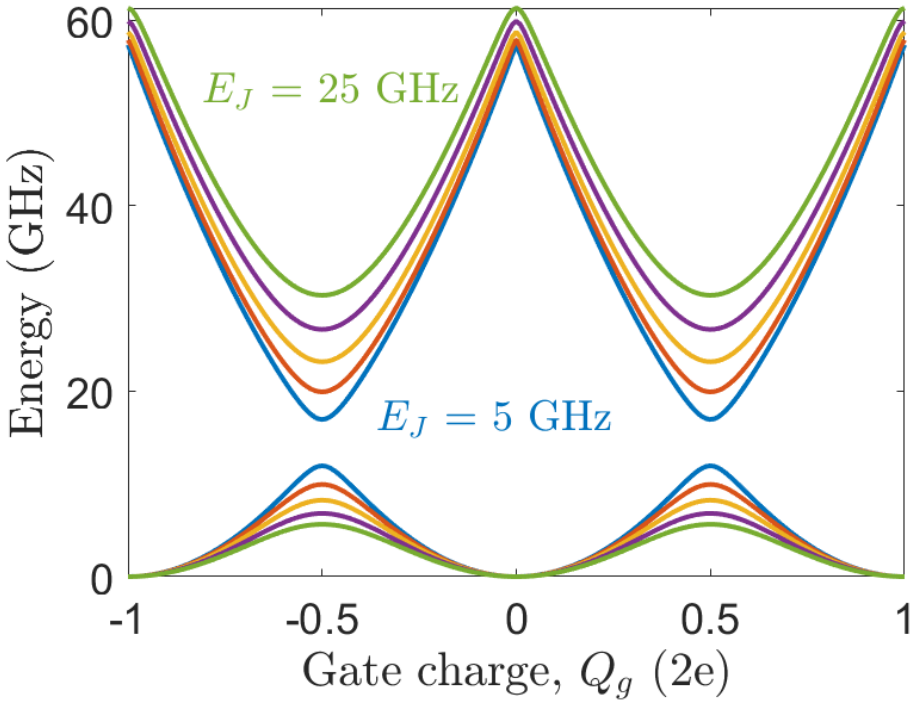

Figure 4.6: Energy spectrum of the coupler as a function of normalized gate charge. Spectrum for different Josephson energies are plotted, equally spaced from 5 GHz to 25 GHz with $C_g = 1\ fF$.

Dependences on the Critical Currents of the Circuit

In the plots that follow, we consider identical qubits, and we fix the shunting capacitance of the qubits to be 1 fF, flux biases at half-flux, critical current density

at 1.7 $\mu A \mu m^{-2}$ and a coupling capacitance with a value of 1 fF. These values were chosen so that the qubit excitation energy was within 4 to 8 GHz when biased at half flux, which are frequencies that are in an experimentally easily accessible range.

We then consider the qubit critical currents from 1 μA to 2 μA and coupler critical currents from 25 nA to 60 nA respectively. At each fixed set of circuit parameters, we extract the YY coefficient from the coupled qubit Hamiltonian at zero gate charge and at half gate charge, as well as the coupler excitation energy at half gate charge. These give the maximum and minimum YY interaction strength and minimum coupler gap respectively. Figures 4.7 and 4.8 show the dependences. Figures 4.7a and 4.7b show that the YY interaction changes sign when going from zero to half gate charge as expected. Furthermore, the coupler excitation energy shown in Figure 4.8 increases with increasing coupler critical current, but decreases with increasing qubit critical current. This could be understood as the minimum coupler gap being tuned by the Josephson energy of the coupler, while additional loading capacitance is introduced when increasing qubit junction sizes, lowering the effective E_c of the coupler. The YY interaction strength is generally on the order of a few MHz, with the largest magnitude at half gate charge. In this region, the interaction strength could reach a magnitude of up to 20 MHz. However, if we try to increase the interaction strength further by lowering the qubit or coupler I_c, then due to the closing coupler gap in this region, the interaction strength will exceed the spectral gap and the reduction method produces a spurious result[54]. In this region, the coupler excited state mixes with the qubit states and the circuit no longer operates as intended.

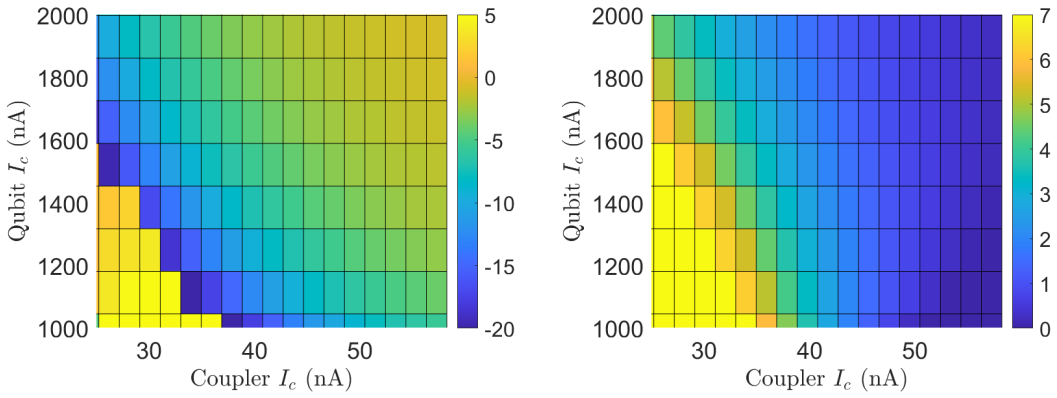

(a) (b)

Figure 4.7: Colour plot of YY interaction strength at fixed gate charge as function of the critical current of the qubits and coupler. The colour axis shows the strength of the YY interaction in MHz. (a) $Q_g = 0.5$. (b) $Q_g = 0$.

The simulation shows that there exists a regime where it is possible for the spectrum to be sufficiently gapped while at the same time giving significant values of the YY interaction strength. We now consider a point in the parameter space, with parameters for the circuit as shown in Table 4.1.

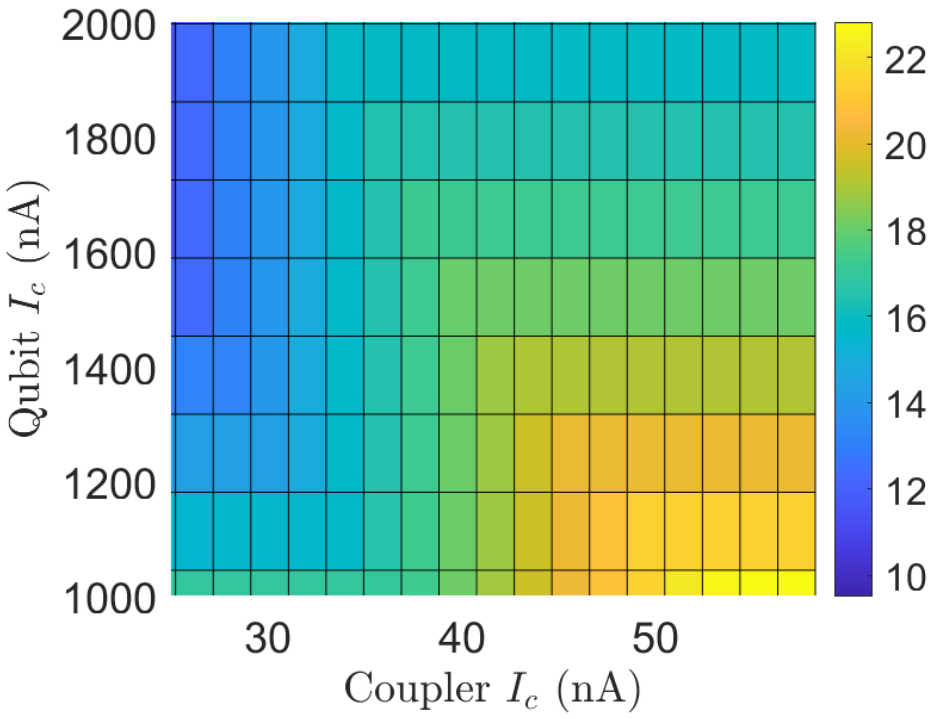

Figure 4.8: Colour plot of coupler excitation energy at $Q_g = 0.5$ as a function of the critical current of the qubits and coupler. The colour axis shows the energy gap in GHz.

Circuit element	Component value
$L_{q1,2}$	0.3 nH
$C_{q1,2}$	42 fF
$I_{cq1,2}$	1.2 μA
C_c	1 fF
C_{coup}	2 fF
I_{coup}	30 nA
C_g	1 fF

Table 4.1: The component values for circuit elements shown in Figure 4.5 used in the subsequent simulations.

We now consider the effect of varying the gate charge over one period for these fixed circuit parameters. The interaction terms from the qubit Hamiltonian are shown in Figure 4.9. The main contribution to the interaction between the two qubits is the YY interaction which can be changed from -20 MHz to about 7 MHz. In particular, it can be turned off at around $Q_g = 0.2$. ZZ and XX terms show also some dependence on gate charge, but are two orders of magnitude less than the YY term, with a maximum absolute value of 0.2 MHz, while all other interaction terms are zero. Figure 4.10 shows the effect on the qubit energy spectrum which accompanies the YY interaction. The first and second excitation energies are shown. When the interaction is zero, the two levels are degenerate. These energy levels are then split by $2h_{YY}$ when we tune the interaction strength. This suggests a method for experimental measurements as we shall see later.

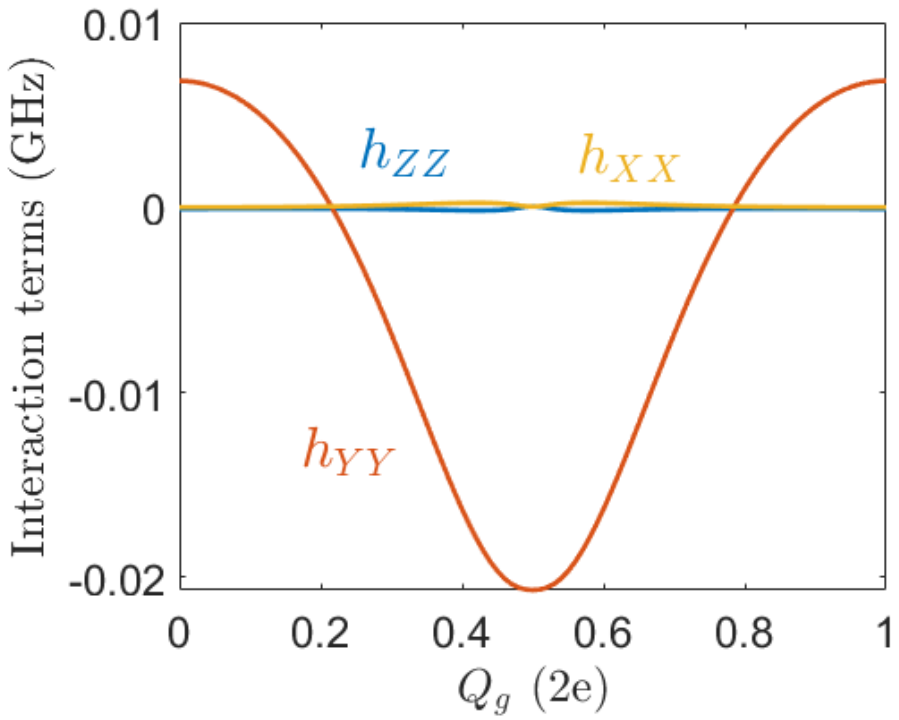

Figure 4.9: Interaction terms in the qubit Hamiltonian for circuit parameters in Table 4.1. The interaction terms in the Hamiltonian shows a dominant YY term that is tuneable across zero, which can be varied from -20 MHz to about 7 MHz across the full range. ZZ and XX terms are two orders of magnitude less than the YY term while all other interaction terms are zero.

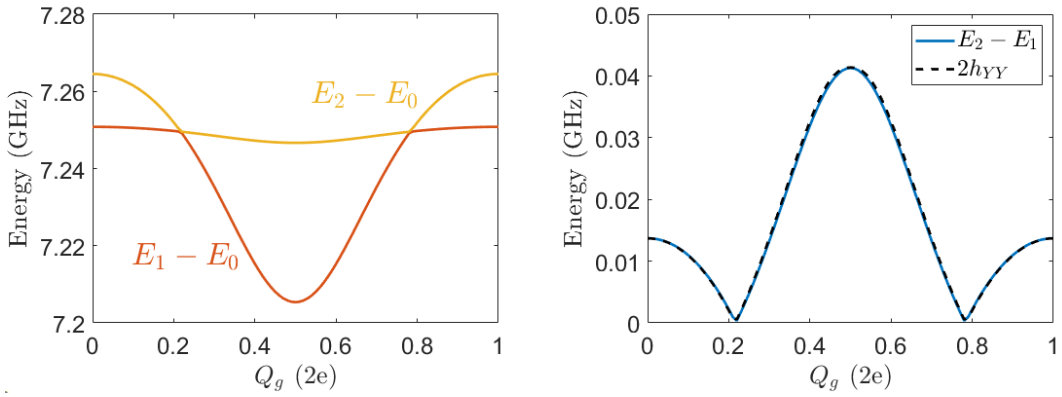

(a) (b)

Figure 4.10: (a) First and second excitation energy of the system with parameters in Table 4.1. (b) Solid line shows the splitting between the first and second energy levels of the system. Dashed line shows the twice the YY interaction strength.

4.2 Experimental Methods

In this section, we consider experimental methods which may be used to verify our circuit simulations presented in the previous section. We first consider a characterisation of the coupler by itself, then describe a protocol for measuring the YY interaction strength of the coupled qubit circuit. Based on these considerations, we design superconducting chips which could be used to implement these experiments.

4.2.1 Experimental Design for Tuneable Coupler Measurements

To characterise the coupling element, we consider the coupler capacitively coupled to a superconducting resonator. This arrangement allows a portion of electromagnetic energy to be coupled into and out of the resonator which is determined by the coupling capacitor. Figure 4.11a illustrates the design of the experimental chip. It shows a feedline coupled to multiple quarter-wavelength resonators of different lengths, which multiplexes the measurement setup. Each resonator is coupled to a superconducting island and a gate voltage is also coupled to the island via a capacitor C_{g1}, which induces the charge on the island. To model this device, we consider the lumped circuit equivalent of the resonator shown in green in Figure 4.11b. The superconducting island is node 1 in this model.

We can extract the resonance frequency using the methods described earlier. For the simulation results that follow, the coupling capacitance is 5 fF, the resonator has capacitance and inductance of 366 fF and 1.66 nH respectively while the junction has a critical current of 30 nA. Figure 4.12 shows the result of simulating the change in resonance frequency as a function of coupler gate charge. The dashed black line is the unloaded resonance frequency of the resonator, while the blue solid line is shifted down due to capacitive loading by the coupler which can be tuned periodically through the gate charge. The tuning is about 15 MHz which should be observable in experiment. As we shall see this is dependent on the

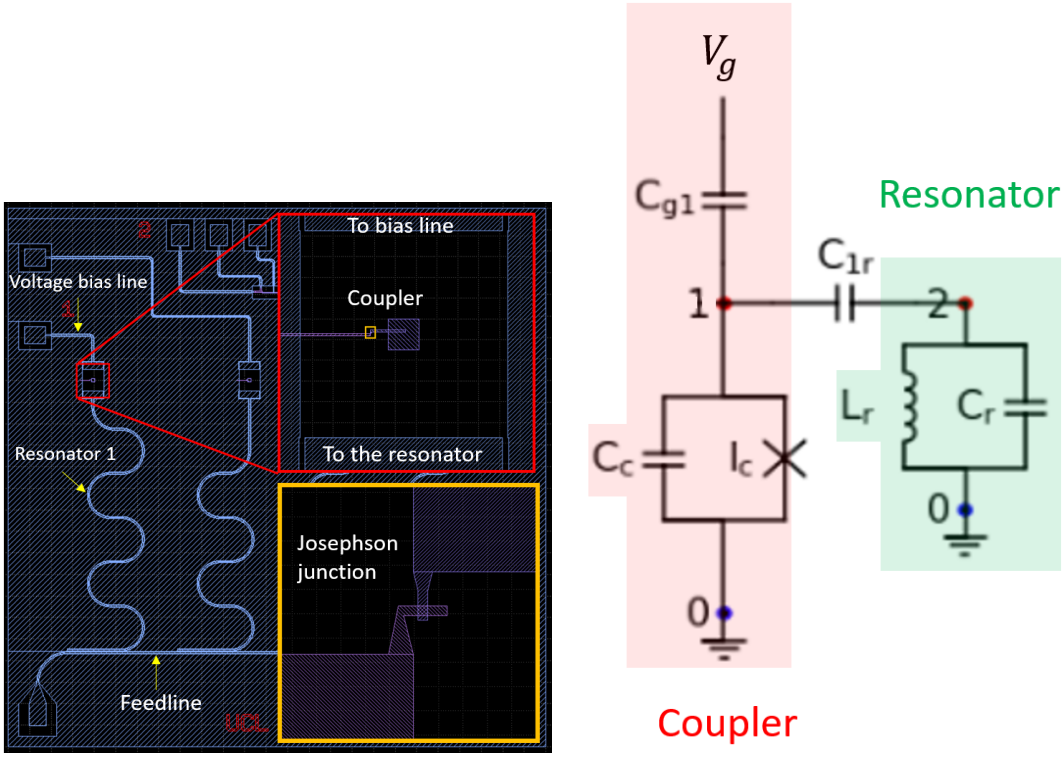

(a) (b)

Figure 4.11: (a) Design of the experimental superconducting chip. Red: Superconducting island magnified. Yellow: Josephson junction magnified. (b) Equivalent lumped circuit model of the coupler capacitively coupled to a microwave resonator.

junction fabrication parameters, which will determine the sizes of the junctions we need for the coupling element to possess the desired properties.

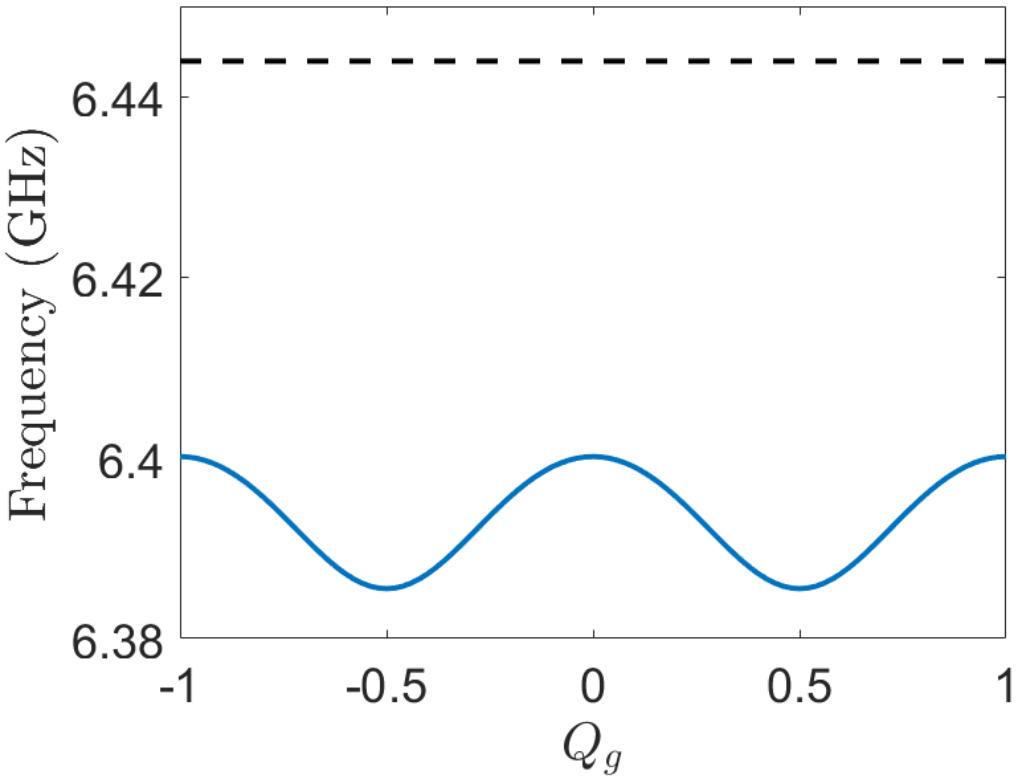

Figure 4.12: Resonator frequency as a function of coupler gate charge for circuit shown in 4.11b. Dashed black line: Unloaded resonator frequency. Blue solid line: Resonance frequency of the resonator-coupler system.

Fabrication Considerations

In practice, these circuit parameters cannot be specified exactly and the critical current of a Josephson junction may vary even on a single chip, widely thought to be due to the structural properties of the oxide barrier in aluminium junctions[118][119][120][121]. Taking this into consideration, we have designed our circuits to tolerate small deviations in junction parameters.

Figure 4.13 shows the variation in the properties of our circuit with respect to fabrication parameters. The key metrics we considered are the minimum gap of the coupler, plotted in solid lines, and the maximum shift in the resonance frequency, plotted in dashed lines. We consider both variations in the junction areas and critical current densities, J_c.

While J_c is a process dependent parameter which depends on the properties of the tunnelling barrier, the area is a better controlled design parameter. Thus, we seek to choose a set of junction areas which will maximize the yield of our devices. The red solid line shows our design requirement based on our metric. Assuming an average critical current density of 1.5 $\mu A \mu m^{-2}$ with a spread factor of two, we designed our chip with several junction areas so that at least one would satisfy these requirements simultaneously, indicated by the green region.

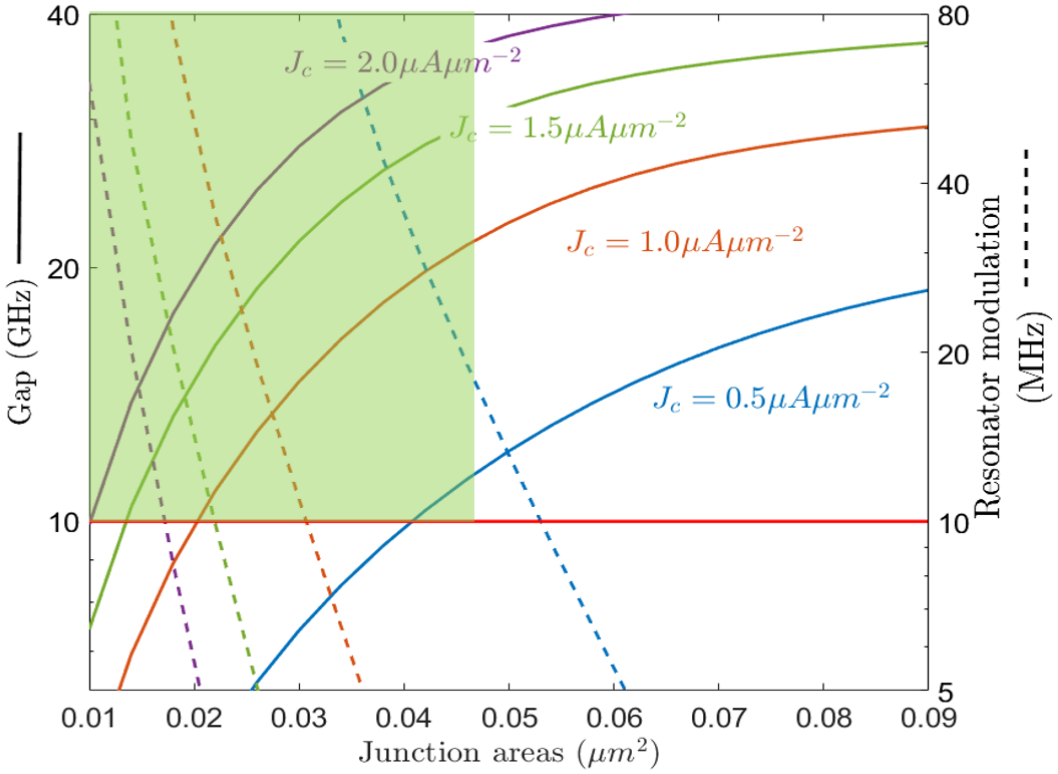

Figure 4.13: Plot shows the simulated minimum excitation energy of the coupler and the change in the resonance frequency of the resonator-coupler system as a function of junction areas. Solid lines: Minimum gap of the coupler obtained from simulation. Dashed lines: Modulation of the resonator-coupler system. Coloured lines indicate different critical current densities J_c, while the red horizontal line shows the minimum excitation energy and resonator modulation desired. The green region is the range of junction areas for which the requirement is satisfied for the range of J_c we expect from fabrication.

4.2.2 Experimental Design for Coupled Flux Qubits Spectroscopy

Superconducting qubit circuits are widely studied experimentally using the circuit quantum electrodynamics (cQED) architecture[122][123], where a qubit is coher-

ently coupled to a superconducting transmission line resonator and is used for non-invasive quantum non-demolition (QND) measurements[124]. The name derives from the study of light-matter interactions using the coupling between the dipole moment of an atom and a single mode of electromagnetic waves using optical cavities. This technique enables spectroscopic measurements of the energy spectrum of the system which we will now describe.

4.2.3 The Dispersive Hamiltonian

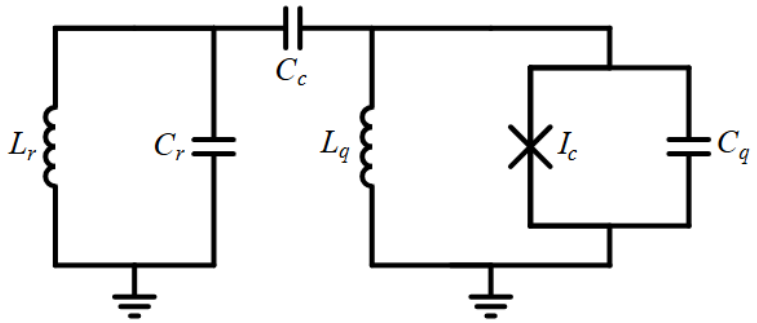

Figure 4.14: A flux qubit of inductance L_q, critical current I_c and capacitance C_q coupled through coupling capacitor C_c to resonator of inductance L_r and capacitance C_r.

We consider a flux qubit capacitively coupled to a superconducting resonator as shown in Figure 4.14. Using the methods described earlier in the chapter, properties of this circuit are given by the Hamiltonian:

$$\hat{H}_{circuit} = \frac{\hat{Q}_r^{\,2}}{2C_r'} + \frac{\hat{\Phi}_r^{\,2}}{2L_r} + \frac{\hat{Q}_q^{\,2}}{2C_q'} + \frac{\hat{\Phi}_q^{\,2}}{2L_q} - E_J \cos 2\pi\left(\frac{\hat{\Phi}_q + \Phi_{ext}}{\Phi_0}\right) + \frac{\hat{Q}_r \hat{Q}_q}{C_c'}, \qquad (4.15)$$

where the subscripts r and q refer to the resonator and qubit respectively. Due to the capacitive interaction, the capacitances $C_r' = C_r + \frac{C_q}{C_q+C_c}$, $C_q' = C_q + \frac{C_r}{C_r+C_c}$ and $C_c' = \frac{C_c(C_r+C_q)-C_rC_q}{C_c}$ undergo loading. In the two-level approximation of the

qubit, the qubit charge operator becomes proportional to the σ_y operator and the interaction strength between the resonator and qubit comes $g = \sqrt{\frac{2}{\hbar Z_r}}\frac{|\langle E_0|\hat{Q}_q|E_1\rangle|}{2C_c'}$, where $Z_r = \sqrt{\frac{L_r}{C_r'}}$. This leads to the Rabi Hamiltonian,

$$\hat{H}_{Rabi} = \hbar\omega_r(a^\dagger a + \frac{1}{2}) + \hbar\frac{\omega_q}{2}\sigma_z - \hbar g(a - a^\dagger)(\sigma^+ - \sigma^-). \tag{4.16}$$

For a typical set of parameters, g is of order 100 MHz, whereas the qubit frequency, ω_q and resonator frequency $\frac{\omega_r}{2\pi}$ are in the range $5-10$ GHz. This allows us to apply the rotating wave approximation by neglecting the terms which change the number of excitations in the system, so that $(a - a^\dagger)(\sigma^+ - \sigma^-) \approx a\sigma^+ + a^\dagger\sigma^-$. Under this approximation the Hamiltonian takes on the form of the famous Jaynes-Cummings Hamiltonian[125],

$$H_{JC} = \hbar\omega_r(a^\dagger a + \frac{1}{2}) + \hbar\frac{\omega_q}{2}\sigma_z - \hbar g(a\sigma^+ + a^\dagger\sigma^-) \tag{4.17}$$

This Hamiltonian has the property that the total number of excitations $n = a^\dagger a + \sigma^+\sigma^-$ is conserved. $\hat{n}$ commutes with the Hamiltonian $[H_{JC}, n] = 0$, so that only states with the same number of excitations interact. It has a simple block diagonal form in the energy eigenbasis,

$$H_{JC} = \begin{bmatrix} H_0 & 0 & 0 & 0 & \dots & 0 & 0 \\ 0 & H_1 & 0 & 0 & \dots & 0 & 0 \\ 0 & 0 & H_2 & 0 & \dots & 0 & 0 \\ \vdots & \vdots & \vdots & \ddots & \dots & \vdots & \vdots \\ 0 & 0 & 0 & 0 & \dots & 0 & 0 \\ 0 & 0 & 0 & 0 & \dots & H_{n-1} & 0 \\ 0 & 0 & 0 & 0 & \dots & 0 & H_n \end{bmatrix}, \tag{4.18}$$

where $H_0 = E_g$ and H_n is a 2 x 2 matrix of form

$$H_n = \begin{bmatrix} n\hbar\omega_r + E_g & -\hbar g\sqrt{n} \\ -\hbar g\sqrt{n} & (n-1)\hbar\omega_r + E_e \end{bmatrix}, \tag{4.19}$$

with eigenvalues $E_\pm = (n\hbar\omega_r + E_g + \frac{\Delta}{2}) \pm \frac{\hbar}{2}\sqrt{\Delta^2 + 4ng^2}$, where $\Delta = \omega_q - \omega_r$ is detuning.

We may further elucidate the result by applying the unitary transformation $U = exp(\frac{-g}{\Delta}(\sigma^+ a - \sigma^- a^\dagger))$. In the dispersive limit $\Delta >> g$, the interaction term can be expanded to second order using the Baker-Hausdorff lemma[126] which simplifies to $H_{int} = \frac{g^2}{\Delta}\hat{\sigma_z}(a^\dagger a + \frac{1}{2})$. The dispersive Hamiltonian now reads

$$H_{disp} = h\left[(f_r + \frac{g^2}{\Delta}\hat{\sigma_z})(a^\dagger a + \frac{1}{2}) + \frac{f_q}{2}\hat{\sigma_z}\right]. \tag{4.20}$$

We see that the frequency of the resonator now acquires a qubit-state dependent term. The bare resonance frequency is shifted due to this interaction by an amount $\delta f = \pm\frac{g^2}{\Delta}$ which depends on qubit state.

Numerical Simulation

We demonstrate numerical simulation of the full circuit Hamiltonian (4.15). Here we consider a flux qubit tuned near the flux-degeneracy point. Figure 4.15a shows the excitation spectrum of the resonator-qubit system. The coloured lines are from numerical diagonalization of the full circuit Hamiltonian, whereas the dashed black lines are the bare resonator and qubit levels. Since the qubit spectrum is approximately quadratic in flux, the reduced flux effectively determines the detuning from the resonator. We find that for a wide range of system parameters, the assumptions used to derive (4.20) hold, with the exception of where the bare qubit and resonator energy levels intersect. In this resonant regime, the interaction results in an avoided crossing, where the splitting is $2\sqrt{n}g$, n being the total number of quanta from (4.19). This is a signature in spectroscopic measurements of qubit-resonator systems, with spectral lines revealing a pattern as seen in Figure 4.15b,

which is often an important experimental tool to help characterise and design superconducting circuits.

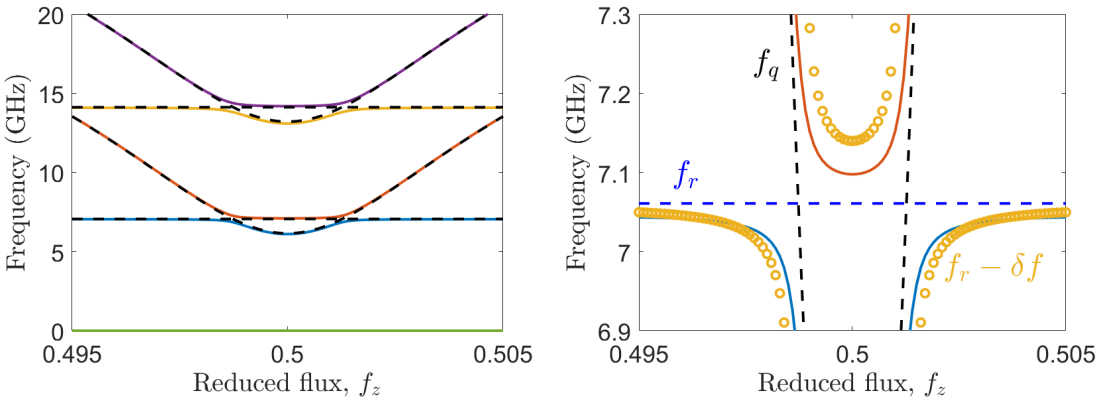

(a) (b)

Figure 4.15: (a) Solid coloured lines: Simulated energy spectrum of the qubit-resonator system as a function of applied flux to the qubit. Black dashed lines: Bare qubit and resonator frequencies in the absence of interaction. The degeneracy is lifted by the interaction, as shown by the coloured lines. (b) A close-up of the region where the avoided crossing occurs. Black dashed lines: Bare qubit frequency. The qubit frequency is quadratic in flux in this range, which appear as straight lines on this scale. Blue dashed line: Bare resonator frequency. Yellow circles: The shifted resonator frequency, $f_r' = f_r - \delta f$ expected from the Dispersive Hamiltonian (4.20). The flux qubit considered in the simulation has parameters as in 4.1, $C_r = 500\ fF$, $L_r = 1\ nH$ and $C_c = 10\ fF$.

4.2.4 Chip Design for Qubit Spectroscopy

While we may fit single-tone data to the numerical simulations as shown in Figure 4.15, there exists another method to measure the qubit transition frequencies directly using an additional RF tone to drive qubit excitations, known as two-tone spectroscopy. As a function of drive frequency ω_d, the qubit excited state population takes on a Lorentzian shape[127],

$$P_e = 1 - P_g = \frac{1}{2}\frac{n_s(2g)^2}{\gamma_1\gamma_2 + \delta_q^2\frac{\gamma_1}{\gamma_2} + n_s(2g)^2}, \tag{4.21}$$

where $\gamma_1 = 1/T_1$ and $\gamma_2 = 1/T_2$ are the inverses of the relaxation and dephasing times of the qubit, and $\delta_q = (\omega_q + \chi) - \omega_d$ is the detuning of the shifted qubit frequency to the drive[127]. By driving the qubit and monitoring the resonator transmission with a probe tone ω_r, one should therefore see a change in transmission when the RF drive tone is resonant with the qubit frequency i.e. $\delta_q = 0$.

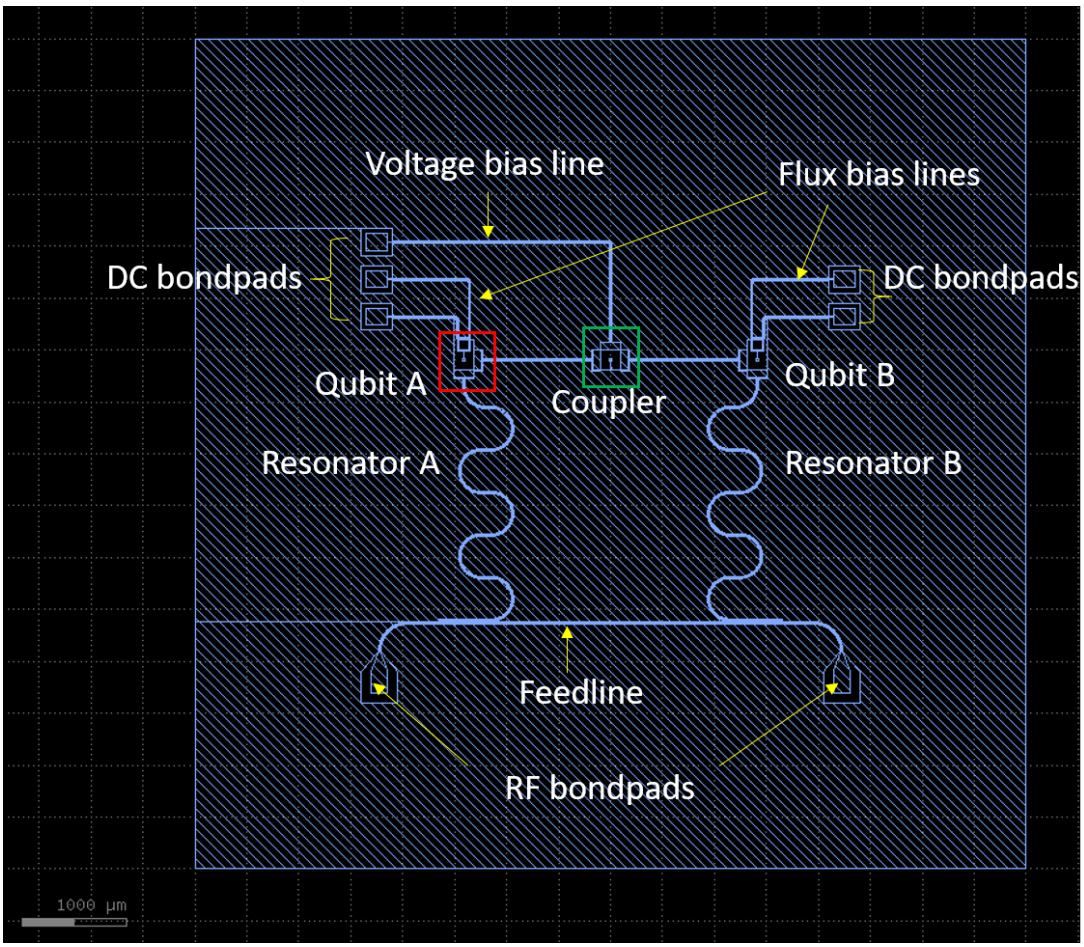

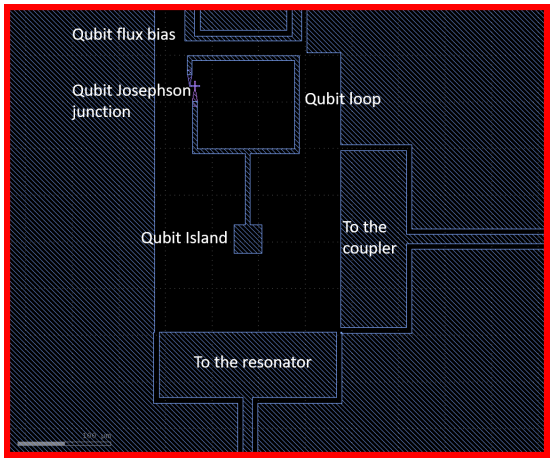

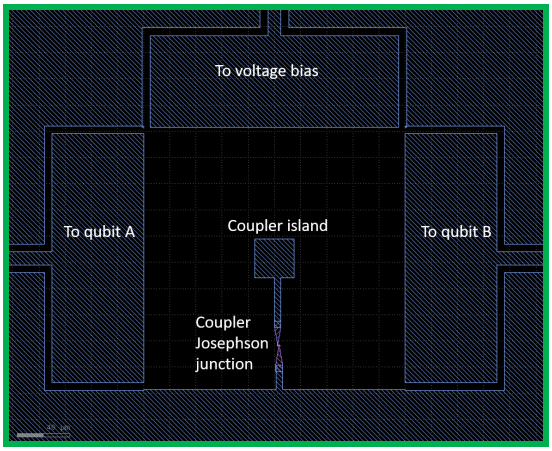

(a) (b)

Figure 4.16: Experimental chip designed to determine the interaction strength for the qubit-coupler-qubit system. (a) Close-up of the qubit. (b) Close-up of the coupler.

Chip Layout and Protocol

Here we describe an approach to measure the YY interaction strength of the coupled flux qubit system considered earlier in the chapter. This approach uses two-tone spectroscopy to measure the degenerate excitation energies of the coupled system, which is then split by the interaction. Coupled flux qubits measured using a similar technique have been discussed in Weber *et al.* [88], for characterising a tuneable inductive coupler.

Figure 4.16 shows the layout for the proposed experimental chip. A feedline couples inductively to two separate resonators. Two resonators are used to measure each qubit, and are designed to have different resonant frequencies. The flux qubits are capacitively coupled to the resonator and the coupler. Fluxes in the inductive loops of qubits A and B can be tuned in-situ by applying a current through the flux bias lines and the coupler gate charge can be tuned by applying a voltage between the voltage bias line and ground.
Table 4.2 gives the junction areas and qubit loop sizes used in the design to achieve the targeted circuit parameters described earlier in Table 4.1. The geometry of the mutual inductances are simulated using ANSYS Q3D solver, which gives a mutual inductance of approximately 20 pH between the qubit loop and the bias line.

Parameter	Name	Value
$A_{jj,q}$	Qubit JJ area	1x1.2 $(\mu m)^2$
$A_{loop,q}$	Qubit loop area	100x115 $(\mu m)^2$
$A_{jj,coup}$	Coupler JJ area	0.2x0.2 $(\mu m)^2$

Table 4.2: Table of designed geometric parameters.

Each qubit can first be characterised individually, by biasing the flux of one near half-flux, and the other near zero. Two-tone spectroscopy can then be performed on that qubit, which can be used to obtain useful information to calibrate further measurements. The two qubits may then be biased to be resonant and the

splitting is given by $2|h_{YY}|$, where h_{YY} is the YY-interaction strength we which to extract. The splitting is then be controlled by the gate voltage as illustrated in Figure 4.17. When the two qubits are not interacting, the resonators read out the qubit frequencies of each qubit individually, while when the interaction is switched on the split levels of both resonators are read out[88].

The approximate zero coupling condition is shown in (c), where qubit A is biased at half flux, and the flux of the qubit B is swept. Assuming identical qubits, the two levels intersect at half flux, although they can be arranged to intersect at different points by biasing the flux of qubit A differently. Different gate charges can then be applied which turns on the interaction. By measuring the splitting for different charge biases, we can construct the dependence of the YY interaction upon the charge bias, as shown earlier in Figure 4.10.

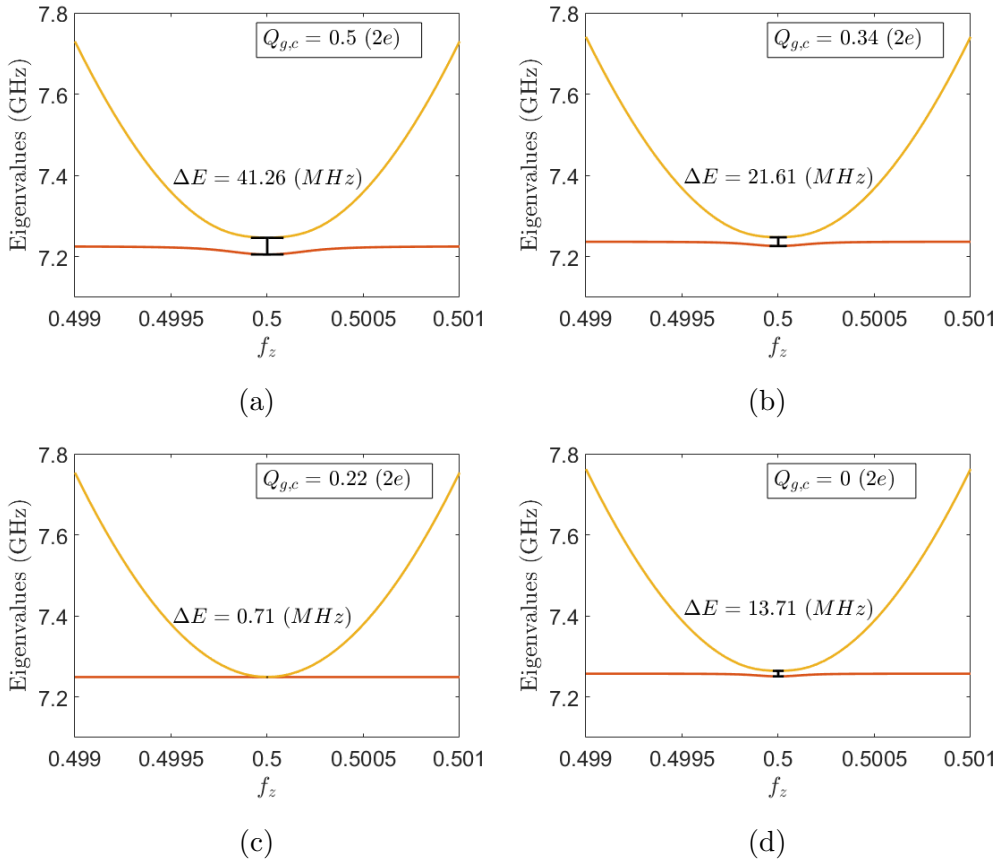

Figure 4.17: Figures show the energy spectrum of the two qubits when the flux applied to qubit A is varied about half flux. The four panels show the splitting of the degenerate levels when the gate charge Q_g is varied.

Chapter Conclusions

In conclusion, we have simulated a tuneable capacitive coupler suitable for applications using flux qubits such as in quantum annealing. We have shown that such a coupling element realizes a sign- and magnitude- tuneable YY interaction which can be varied in-situ using on-chip voltage bias through a gate capacitor applied to the coupler. The system spectrum is found from numerical simulations of the circuit Hamiltonian and the Pauli coefficients was extracted. From these simulations, we identify the tradeoffs one can make in the design of the circuit and chosen circuit parameters such that the YY interaction term is tuneable across zero through a range of about 30 MHz.

We then considered how the device can be verified experimentally, in particular designed a chip which would allow the coupler to be characterised by itself, before considering the problem of measuring the YY interaction strength in practice. By considering the characterisation of the coupler, we have also identified the sensitivity of the design to fabrication parameters, which we have incorporated into the simulation. We designed our experimental chip with different Josephson junction areas assuming a critical current density spread by a factor of two.

Finally, we discussed the cQED architecture and derived the dispersive Hamiltonian which describes the interaction between a superconducting resonator and qubit. The architecture enables continuous measurement of the qubit-resonator system. A direct approach of obtaining the qubit spectrum is by using an additional tone to excite the qubit, which changes the transmission of the resonator probe tone. Based on these techniques, we designed a superconducting chip to carry out qubit spectroscopy and described a protocol that can be used to experimentally determine the coupling strength. These chip designs and measurement protocols are a step towards future implementations of pairwise tuneable YY coupling for flux qubits which can be integrated with ZZ coupling currently available in quantum annealers.

Chapter 5

Fabrication of Josephson Junctions

In the previous chapter, we designed a new non-linear capacitive element suitable for coupling two flux qubits. To experimentally verify the design, the next step was to implement this design in hardware. This involves a crucial process for fabricating a Josephson junction (JJ). Such a process often requires specialized equipment to make the junction electrodes and oxide barrier. Even with the same equipment, many trial runs of the process are required to calibrate the junction parameters obtained, which may even drift over time. Moreover, there is often a large parameter space to explore in each step during the development of a new fabrication process. In this chapter, we determine the feasibility of fabricating JJs using the methods and equipment available at the cleanroom in the London Centre for Nanotechnology.

One common method of producing the Al-AlOx-Al structure of a Josephson junction is by using a shadow evaporation technique. The technique involves a stack of multiple layers of resist patterned as either a suspended bridge or with a significant undercut. This is achieved by using resists of different exposure sensitivities. The deposition is usually carried out in an evaporation chamber. The resist is designed so that at a certain angle, the deposition of the Al onto the substrate

will depend on the orientation of the sample. Due to the undercut, evaporation at an angle results in deposition on the resist walls at specific orientations.

In recent years, there has been growing interest in developing new junction fabrication techniques that do not involve angle-dependent deposition. This is because the angular dependence makes the method unsuitable for large scale wafer-scale manufacturing as it reduces junction area uniformity[128][129][130], requiring careful calibration to reduce the variability. An alternative approach which eliminates the angular dependence altogether is to make overlap junctions[131][132][133], which makes the two electrodes of the JJ in separate processing steps. Thus the method does not require specialized equipment for performing angular deposition, but instead uses standard deposition and lithography techniques. The process however involves breaking vacuum in between the deposition steps, so preparing a high quality interface and oxide layer becomes the main challenge of this technique. This is the subject of this chapter which explores the processes involved in fabricating overlap JJs.

5.1 Development of the Fabrication Process

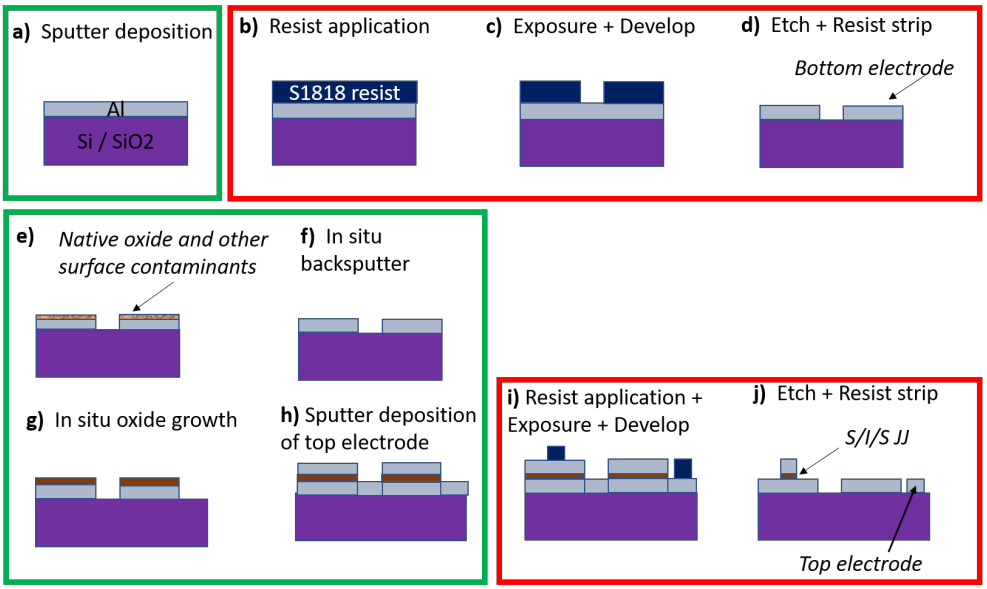

Figure 5.1: The overview of the Josephson junction fabrication process. The green boxes indicate processes taking place in the PVD-75 sputter system, while the red boxes indicate photolithography steps. First row shows the deposition and patterning of the first aluminum layer, second row shows the backsputtering after the sample is reintroduced into the chamber, while the third row shows re-oxidation, deposition and patterning of the second aluminum layer.

The outline of our fabrication process is as shown in Figure 5.1. Steps (a), (e), (f), (g) and (h) highlighted in green boxes take place within the sputter chamber under high vacuum, while steps (b), (c), (d), (i) and (j) highlighted in the red boxes are carried out externally. Steps (a), (b), (c) and (d) describe the deposition and patterning of the bottom electrode. First, a silicon substrate is prepared and cleaned then aluminum deposited by magnetron sputtering. The sample after the deposition is shown in (a). Next, the sample is then removed from the deposition chamber for resist coating which results in (b). The resist is then exposed using direct-write laser photolithography according to the designed layout and developed. The resist acts as an etch mask as depicted in (c), so that the aluminum

layer at the exposed regions can be etched away and the design pattern transferred onto it. The resist is then subsequently cleaned off using IPA and acetone solvent solution, leaving the bottom electrode as shown in (d).

Since the two electrodes are patterned in separate steps, the bottom electrode is exposed to the atmosphere and a native oxide layer with unknown composition is formed, as shown in process step (e), rendering the junctions unsuitable for making coherent quantum devices[134]. Because of this, it becomes necessary to introduce a cleaning step to remove this layer of contaminants before re-oxidising the bottom electrode. To achieve this, we used a backsputter cleaning technique to remove the unwanted material from the interface as shown in step (f). Steps (g) and (h) show the in-situ oxide growth of the bottom electrode and sputter deposition of the rest of the metal layer. This layer is patterned similarly to the first as shown in (i) and the S-I-S junction is formed from the overlap region masked by the resist as shown in (j).

The fabrication process is in contrast to the double shadow-evaporation technique, where the bottom electrode, oxide layer and top electrode of the JJ are all deposited in the same chamber under vacuum. Typically, another metal layer containing the main features of the circuit is patterned before junction deposition. So that in this case, since the junction leads must make contact with the metal layer, an argon milling step is usually introduced before deposition to ensure good contact is made between these layers.

In the next subsections, we describe each step of our fabrication process in detail.

5.1.1 First Layer Patterning

Our Al films are grown using magnetron DC sputter deposition in the Kurt J. Lesker PVD75 sputtering system. In magnetron sputtering, gas is flowed into a

high vacuum chamber where it is ionized by a high DC voltage. Sputtering occurs when the ions are accelerated towards a target of the desired material. Due to the high energy bombardment by the incident ions, atoms of the target material break free from the surface which travels toward the substrate where it is deposited. The magnetron focusses the plasma near the surface of the target which increases the sputter rate. An illustration of the sputtering process is shown in Figure 5.2.

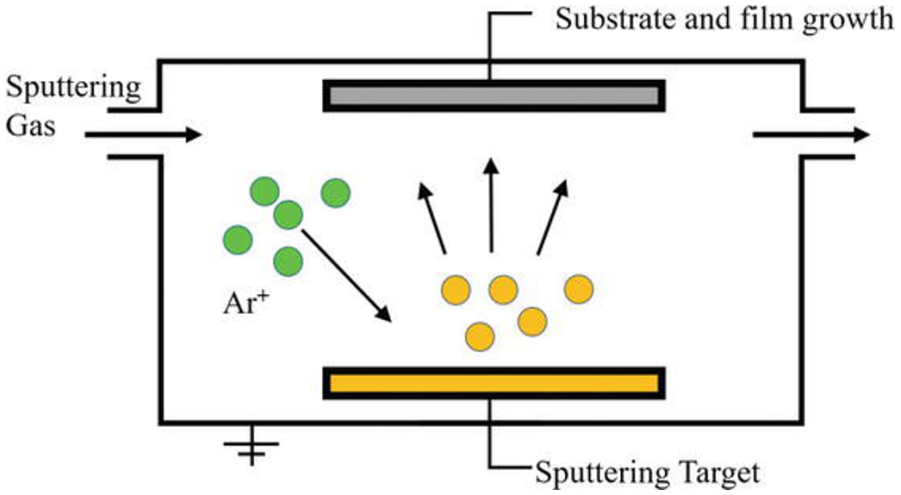

Figure 5.2: Illustration of the sputtering process. Argon ions are accelerated to the sputtering target. The chamber is maintained in vacuum so that the sputtered material is deposited onto the substrate.

Our sputter system contains mass flow controllers which are capable of controlling the flow rate of various gases into the chamber. Gases include argon and oxygen which we use in sample cleaning and oxide growth respectively. We use an aluminum target held onto one of the three 3" diameter sources. The sample holder and the target comes with controllable shutters to start and stop the sputtering process. The sample holder also has a motor which spins the sample to increase uniformity. It is also connected to a DC power source which allows us to direct the plasma onto substrate for sample cleaning.

We start our process by dicing a 4" thermally oxidized silicon wafer, with 100

nanometer thick SiO_2 into 8×8 mm^2 pieces using the Disco DAD 3230 Automatic Dicing Saw. Before the diced samples are ready for further processing, they are cleaned using acetone and isopropyl alcohol (IPA), sonicating in each for 5 minutes. To deposit the first Al layer, the sample is first stuck onto a carrier wafer using Kapton tape which is then loaded onto the sample holder of the sputtering chamber. The chamber is then pumped down to a low pressure before starting the automated DC sputter process.

The sputtering process starts with flowing Ar gas into the chamber to a set chamber pressure, and the power supply ramps up to the voltage set by our recipe. Once the desired pressure and bias voltage is reached, the sputter target is cleaned for 3 minutes, with the substrate shutter closed. After this, the substrate shutter is opened and the Al is sputtered for a fixed time until the desired thickness is achieved. For our particular process, the relevant sputter parameters are as follows:

Sputter parameter	Value
Typical base chamber pressure	2.4e-7 Torr
Sputter pressure	2.3 mTorr
Power	500 W
Ar flow rate	10 sccm
Sputter rate	11.6 nm/min
Sputter time	4 min 30 sec
Target film thickness	50 nm

Table 5.1: Sputtering parameters for Al deposition in the Lesker PVD75 system.

The low temperature electronic properties of an unpatterned Al film were measured using the four terminal measurement technique. The sample was wirebonded onto a sample holder, which was then mounted in the dilution refrigerator where it was cooled down to the milli-Kelvin range. The sample was found to be superconducting, with resistance dropping to zero at around 1.2K, the transition temperature of Al. The characteristic temperature-dependence of the critical cur-

rent was also observed.

In Figure 5.3a is the data obtained from performing temperature dependent measurements on the Al film. The temperature is controlled by the dilution fridge electronics which has a feedback loop which varies the electrical current flow through a resistor in the mixing chamber plate of the fridge to achieve the temperature set point. A triangular current waveform at $\pm 4\ mA$ peak current flows through the sample via one pair of electrodes, while voltage is measured on another. The green data points indicates an increasing current, while the red indicates decrease, as indicated by the arrows. The measurement shows a zero-voltage supercurrent, until about 2.1 mA, where it jumps suddenly into a resistive state. The critical current of the film is lower when going from the superconducting to resistive state, and higher when going from resistive to superconducting state. This could be due to resistive heating of the sample in the dissipative state. Figure 5.3b shows the measured temperature dependence of the critical current, which is given by an approximate parabolic shape.

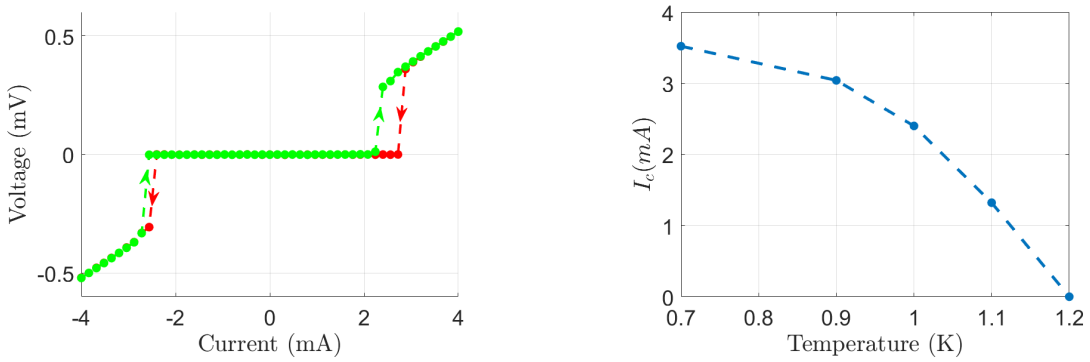

(a) (b)

Figure 5.3: The low temperature electronic properties of an unpatterned Al film. (a) Four quadrature measurement of the current-voltage characteristic of an unpatterned Al film. Green data points: Increasing current. Red data points: Decreasing current. (b) The critical current dependence upon the temperature for an unpatterned Al film.

5.1.2 Backsputter Cleaning

As the sample is transferred to different chamber for patterning, it is exposed to atmosphere. Therefore, it is necessary to perform a cleaning step before the controlled growth of the oxide layer. This cleaning step removes the native oxide layer which develops when the sample is exposed to air, and other contaminants which may be present at the interface due to the processing steps. This step can be performed in the sputterer where the oxidation and deposition of the second layer can take place subsequently without breaking vacuum. After the lithography of the first layer, the sample is loaded into the sputter system again. Before the growth of any addition material, we perform a back-sputter cleaning step. The procedure is analogous to sputtering - Ar is flowed into the sputter chamber, and a plasma is ignited. However, this time a DC bias voltage directs the plasma generated onto the sample. We found that this step heats the sample holder to a temperature of about 30°C. The backsputter recipe is shown in Table 5.2.

Parameter	Value
Backsputter pressure	5 mTorr
Backsputter Ar flow	18.7 sccm
RF power	100 W
DC voltage bias	500 V
Backsputter time	5 mins

Table 5.2: Backsputter parameters in the PVD75 for interface cleaning.

Figure 5.4 shows the temperature dependence of the resistance of a metallic contact with an area of 37.5 μm^2 measured in a dilution refrigerator. The metallic contact is made by backsputtering the first layer electrode, and depositing the second layer without any reoxidation. The resistance shows a linear decrease with slope of 0.038 Ω/K with temperature until about 70 K, where thermal scattering starts to be suppressed. The low temperature resistance is then constant which is expected from temperature independent defect scattering processes. At the critical

temperature of aluminum 1.2 K, the metallic contact undergoes a superconducting transition, however we note that the resistance remain nonzero.

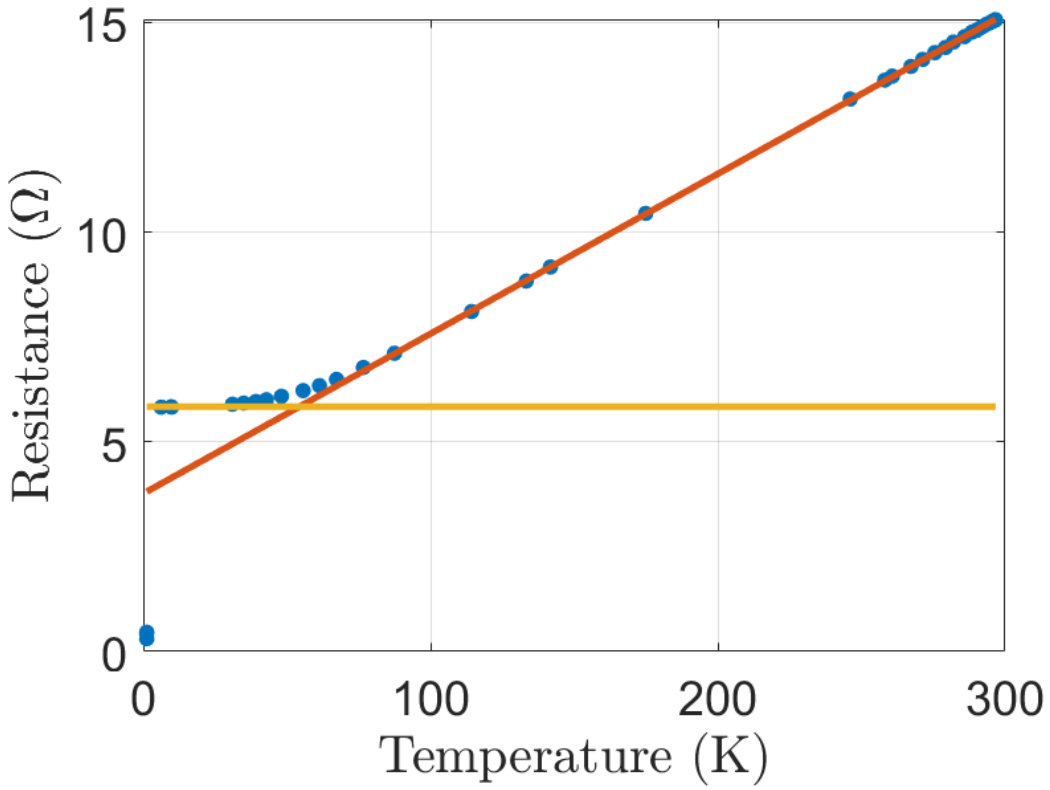

Figure 5.4: Resistance against temperature of a metallic contact with an area of 37.5 μm^2. Red line: Straight line fit with slope of 0.038 Ω/K. Yellow line: Indicates the low temperature resistance before the superconducting transition.

5.1.3 Oxide growth

The oxidation step determines the most crucial parameter in fabricating the JJ, that is the critical current density, J_c. J_c decreases exponentially with increasing oxide thickness, which makes its control challenging in a fabrication process. The value of J_c must also be taken into account in design as it determines the physically realisable $\frac{E_J}{E_C}$ associated with the junction. Process parameters that affect the oxide thickness are the oxygen flow rate, chamber pressure and the oxidation time. There have been empirical studies based on large numbers of junctions [135][136] which attempt to map these parameters to oxide thicknesses, which we use to base our oxidation parameters. We have tried Al oxide growth in both the low and high pressure regimes, eventually opting for the latter due to the improvement in the JJ yield observed in low-temperature measurements.

The samples are sputter-cleaned for the same duration before being oxidised. During the oxidation step, oxygen gas is flowed continuously with the vacuum valve throttled and pump running, achieving a controllable steady-state pressure. The recipes for the high and low pressure oxidation is presented in Table 5.3. In the low-pressure regime, to achieve the correct dose according to the relation found in [135], our oxidation times needed to be quite long for us to produce samples which exhibited a non-linear IV characteristics at low temperatures. Even then, the yield was quite low, only one in eight devices had JJ-like behaviour. Improvement in yield was found by increasing the oxidising pressure while exposing the samples for a shorter amount of time.

Parameter	Recipe 1	Recipe 2
Oxygen flow	10 sccm	10 sccm
Oxidation pressure	2.3 mTorr	75 mTorr
Oxidation time	4.5 to 45 mins	5 mins

Table 5.3: Oxidation parameters in the low and high pressure regimes in the PVD75.

First we characterised the room temperature resistances of the samples on a probe station. The samples had both bottom and top electrodes patterned, with different processing for the interface layer. Figure 5.5 shows their measured resistances. The highest resistances were observed for the unprocessed metallic contacts, associated with native oxide layer due to atmospheric exposure. After backsputtering, most of the native oxide is removed and this is reflected by the decrease of resistances by five orders of magnitude.

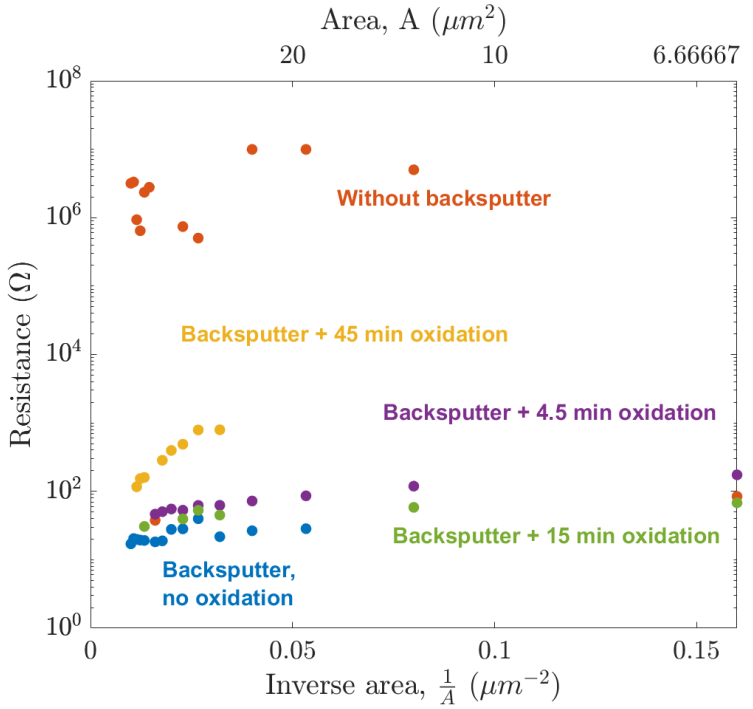

Figure 5.5: The resistance of samples under different processing conditions.

5.1.4 Direct Write Photolithography

We used photolithography to pattern the Al films. S1818 resist is spun onto the surface of the film. Once coated, the sample is baked at 115°C for 60 seconds. The resist is exposed in the Heidelberg DWL 66+ laser writing system. A list of parameters used for the exposure is summarized in the Table 5.4. The sample is developed in MF319 developer for 1m30s, in which the exposed region will dissolve. The unexposed region masks the metal layer during the etching step, whence the pattern is transferred onto the Al. Once etched, the sample is rinsed and inspected under the microscope.

Parameter	Value
Laser focus	-20
Laser Intensity	70%
Laser Power	60 mW
Exposure Count	2
Filter	50%

Table 5.4: Direct write photolithography parameters used in the Heidelberg DWL 66+ for exposing S1818 resist.

Figures 5.6a and 5.6b show optical micrographs of the sample after patterning the first and second layer respectively. Figure 5.7 shows the developed resist structures prior to etching the second layer.

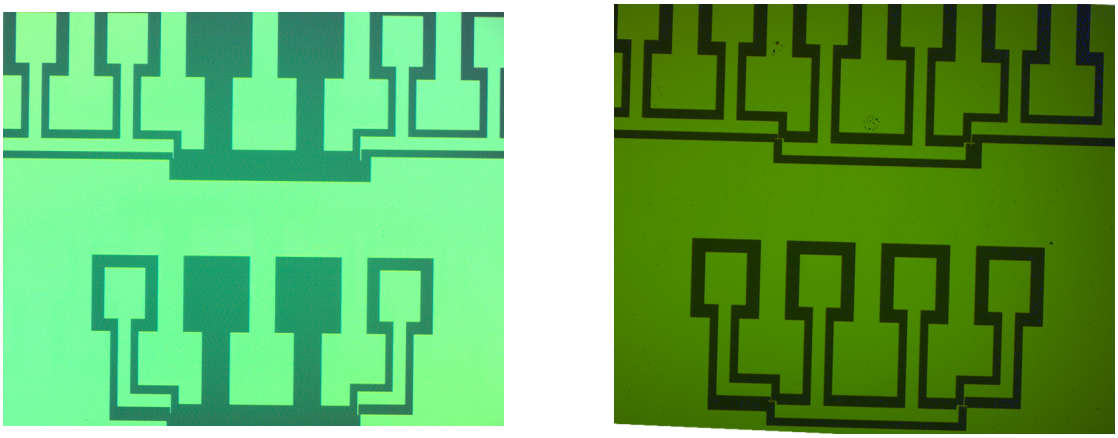

(a) (b)

Figure 5.6: Patterned aluminum films after (a) layer 1 and (b) layer 2 processing respectively.

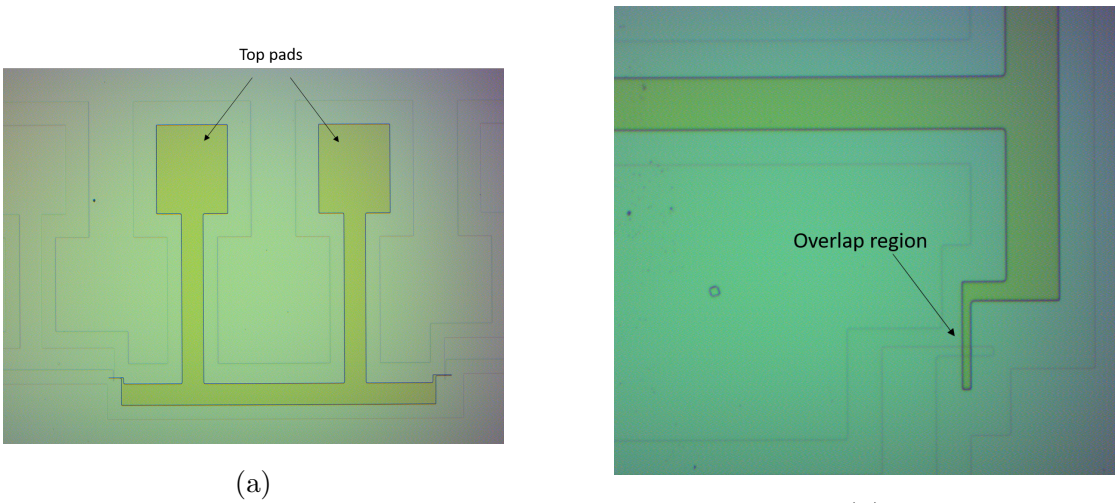

(a) (b)

Figure 5.7: Resist masks for layer 2 features. (a) Structure of the top electrodes and pads. (b) Zoom-in of the overlap region which forms the junction.

5.1.5 Electron-Beam Lithography

We also fabricated some samples using electron-beam lithography (EBL). A photolithography system is limited by the wavelength of the light used by the laser, which makes it unsuitable for writing sub-micron structures. Thus, EBL is needed for scaling down the junction to sub-micron sizes. The samples were fabricated in a Elionix ELS G100 system, which also writes the pattern onto the sample directly.

The EBL system is capable of producing a stable electron beam with an acceleration voltage of up to 100 kV. The acceleration voltage is a crucial parameter in a EBL system as it determines the size of the electron beam. This is not the only factor affecting the resolution however, because the electrons interact with the material being exposed. As the electrons are incident on the resist and the substrate, they may scatter or generate secondary electrons. Because of this, the region outside of the intended scanned pattern receives a non-zero dose, causing an effective broadening of the electron beam. This is known as the proximity effect. The electron beam can be deflected within a small region, known as a field. For features outside of the region, the stage is required to move. These movements are calibrated by the manufacturer so that patterns on different fields are stitched together as seamlessly as possible. The field is then written to by the beam in a grid of dots, in the manner of a vector scan.

Just like in photolithography, choosing a proper dose for the exposure is crucial. On the EBL system, this is adjusted by choosing a beam current, a dwell time on each dot and the spacing between the dots. This dose is measured in units of charge per area. The system is also capable of varying the beam current. This allows the design to be exposed in two steps, one for micron-scale features and one for nano-scale. A large current is used to expose the large features to speed up the exposure, while a small current is used for writing the finer features with precision. Tables 5.6 and 5.5 show the exposure parameters for small and large currents. The exposed resist is then developed in a 3:1 mixture of methyl isobutyl ketone (MIBK) and IPA for 45 seconds. Afterwards, the sample is soaked in IPA

for 30 seconds to stop the development.

Parameter	Value
High beam current	60 nA
Dot number	1,000,000 dots
Field size	1,000 μm^2
Scan/feed pitch	90 nm/dot
Areal dose	1,000 $\mu C/\mu m^2$

Table 5.5: High beam current dose settings used for EBL exposure in the Elionix ELS G100 system.

Parameter	Value
Low beam current	1 nA
Dot number	1,000,000 dots
Field size	500 μm^2
Scan/feed pitch	2 nm/dot
Areal dose	600 $\mu C/\mu m^2$

Table 5.6: Low beam current dose settings used for EBL exposure in the Elionix ELS G100 system.

5.1.6 Etching

After the resist has been patterned, an etching step is used to transfer the pattern into the metal layer. Two techniques for etching were considered for this project. First, we considered a wet etching method. This process involves immersing the sample into a chemical etchant in a beaker, for a fixed time. For our samples, we used a standard mixture of aluminum etchant which contains phosphoric acid, nitric acid, acetic acid and water as etchant. The etch rate is about 1 nm/s so for our 50 nm films we etch them for about one minute. This method results in an isotropic etch profile, as the solution will remove the metal in every direction. This characteristic makes the process unsuitable for etching small features, in which case a directional etch process is desired.

Reactive-ion etching (RIE) is one such technology which results in a highly anisotropic etch. We carried out our etch in a STS Inductively-Coupled Plasma Shallow Reactive-Ion Etch (ICP-SRIE) system. The system uses an inductively coupled plasma where the alternating fields used to generate the high density plasma are created by an induction coil and RF source in the vacuum chamber. Gas is flowed into the chamber, which ionizes and forms the plasma. For Al, the gases used are Cl_2 and BCl_3. Cl_2 reacts with Al to form Al_2Cl_6 and $AlCl_3$ which are volatile by-products that are pumped away from the chamber, while BCl_3 is used to etch any Al oxide which may have formed on the top layer.

Table 5.7 shows the parameters used for our RIE recipe and Table 5.8 shows the estimated etch rates of various materials from our calibration measurements.

Parameter	Value
Cl_2 flow rate	18 sccm
BCl_3 flow rate	5 sccm
Chamber pressure	3 mTorr
Coil power	400 W
Platen power	60 W
Etch time	35 s

Table 5.7: RIE parameters for etching Al in the STS ICP SRIE system.

Material	Estimated etch rate
Al	2.2 nm/s
SiO_2	0.5 nm/s
S1818	3.2 nm/s
PMMA 950 A4	4.4 nm/s

Table 5.8: RIE etch rates of different materials used in the process estimated using the recipe described in Table 5.7.

5.2 Josephson Junction Measurements

This section presents measurement results of JJs with junction areas in the 1 μm^2 to 100 μm^2 range, which can be described by the Resistive Capacitively Shunted Junction model discussed in Chapter 2. Results discussed in this sections are measured from samples fabricated using the EBL, RIE and oxide growth techniques described in the previous section.

5.2.1 Experimental Setup

The measurements were performed in a dilution refrigerator at base temperature which is about 15 mK. The fabricated chip is stuck onto a chip carrier using GE varnish, which is an adhesive with good thermal conductivity. The chip contact pads are then wire bonded onto the sample holder PCB which allows electrical connections to be made to the external measurement circuit. The chip carrier containing a wirebonded sample is shown in Figure 5.8. The sample space is enclosed in cylindrical shields to minimize stray magnetic fields affecting our experiments. The inner shield is made of aluminum, which expels magnetic field below its superconducting transition temperature. The outer shield is Amumetal A4K, a high permeability mu-metal alloy, which redirects magnetic fields away from the sample space.

NbTi+Cu (Niobium-Titanium + Copper) superconducting wires are used to connect the sample carrier to the DC lines built into the dilution refrigerator. These DC lines are routed to the top of the fridge where it is further routed through Fischer cables into the QDevil breakout box panels. Each wire comes out to a BNC connector on the panel situated in our experimental rack, which serves as the interface to our samples.

Current-voltage characteristics of the JJs are obtained using a four-point probe measurement method. A Keithley 6220 Precision Current Source and an Agilent 34410A Digital Multimeter was used as the current source and voltage monitor.

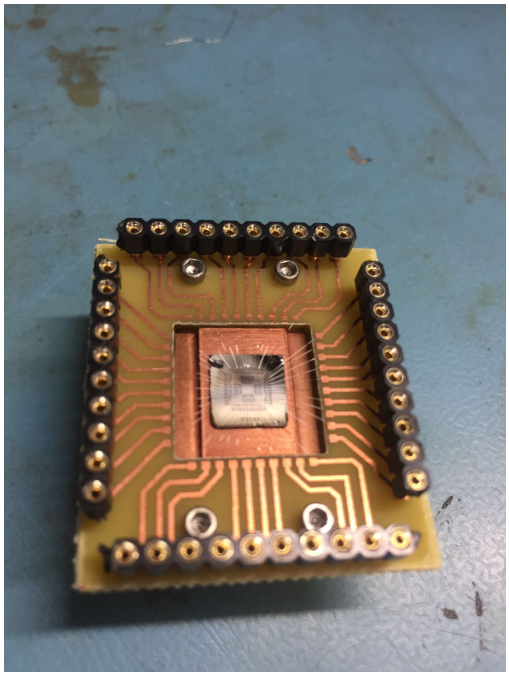

Figure 5.8: The chip carrier used for transport measurements of the JJs in the dilution refrigerator. The fabricated chip is wirebonded onto a PCB, 32 mm × 36 mm in size, with a 15 mm x 15 mm square cut-out of the middle.

The source is programmed to output a four-quadrant triangular digital waveform and the voltage is measured at each current setpoint.

5.2.2 Measured IV characteristics of JJs

Figure 5.9 shows the IV characteristics of JJs measured on the same chip. These junctions have different junction areas, 25 μm^2 and 100 μm^2 respectively. The IV curves were measured to be continuous and non-hysteretic, but show a supercurrent carrying, zero-voltage state. Furthermore, the IV curves show a positive curvature approaching the resistive state. Qualitatively, this indicates the presence of a Josephson supercurrent rather than a superconducting short. The critical currents were estimated to be 37.5 μA and 195 μA respectively by thresholding, using a threshold voltage of 3 μV. This gives us critical current densities of 1.48 $\mu A/\mu m^2$ and 1.95 $\mu A/\mu m^2$. The normal state resistances in the linear regime are

16 Ω and 5 Ω respectively. From these measurements, we observe that the junctions do not follow the Ambegaokar-Baratoff relation, instead the I_cR_N product is about 2 to 3 times higher than predicted. Furthermore, by fitting to the RCSJ IV curve using the standard junction capacitance density of 45 $fF/\mu m^2$, we find the Stewart-McCumber parameter to be $\beta_c \approx 27$, which is different from the expected $\beta_c \ll 1$ regime as we do not observe hysteresis.

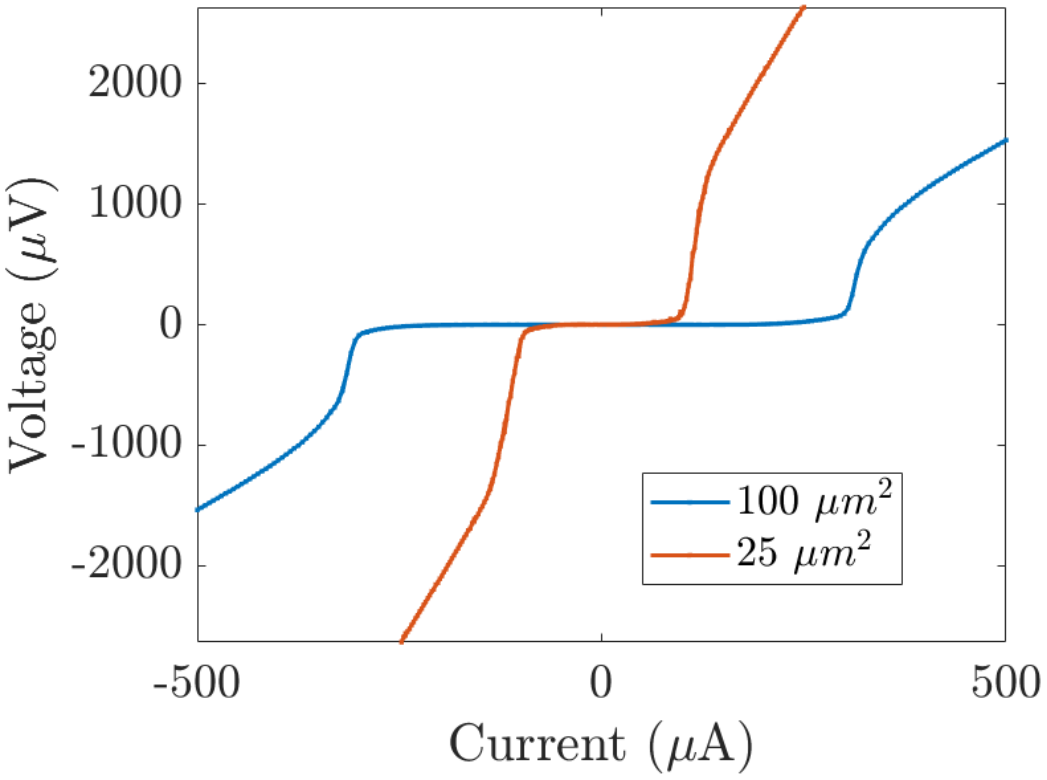

Figure 5.9: Current-voltage characteristics of Josephson junctions with areas 25 μm^2 and 100 μm^2. The junctions were part of the same chip measured at 10 mK.

Effect of RF Radiation

The junctions were also subject to RF irradiation by an unterminated coaxial cable suspended in the sample space close to the device. A RF source is then used

to supply the radiation at 1.391 GHz with powers ranging from -50 to -13 dBm. This frequency was chosen as it gave the largest voltage response near the critical current. Figure 5.10 shows the effect of RF upon the IV characteristic of the JJ at various powers. The critical current of the device decreases as the RF power is increased as shown in blue in Figure 5.11. Additionally, the zero-bias resistance of the junction also increases with RF power as shown in orange in Figure 5.11. The increase in slope in the superconducting phase can be understood in terms of the tilted washboard model, as the phase escaping from the potential barrier. There are two possibilities here, either the RF radiation induces quantum tunnelling of the phase through the barrier, or it could also be a thermal effect so that local heating at the sample induces thermal activation across the barrier. The Shapiro steps expected at about 2.9 μV based on Equation 2.12, were not observed, however.

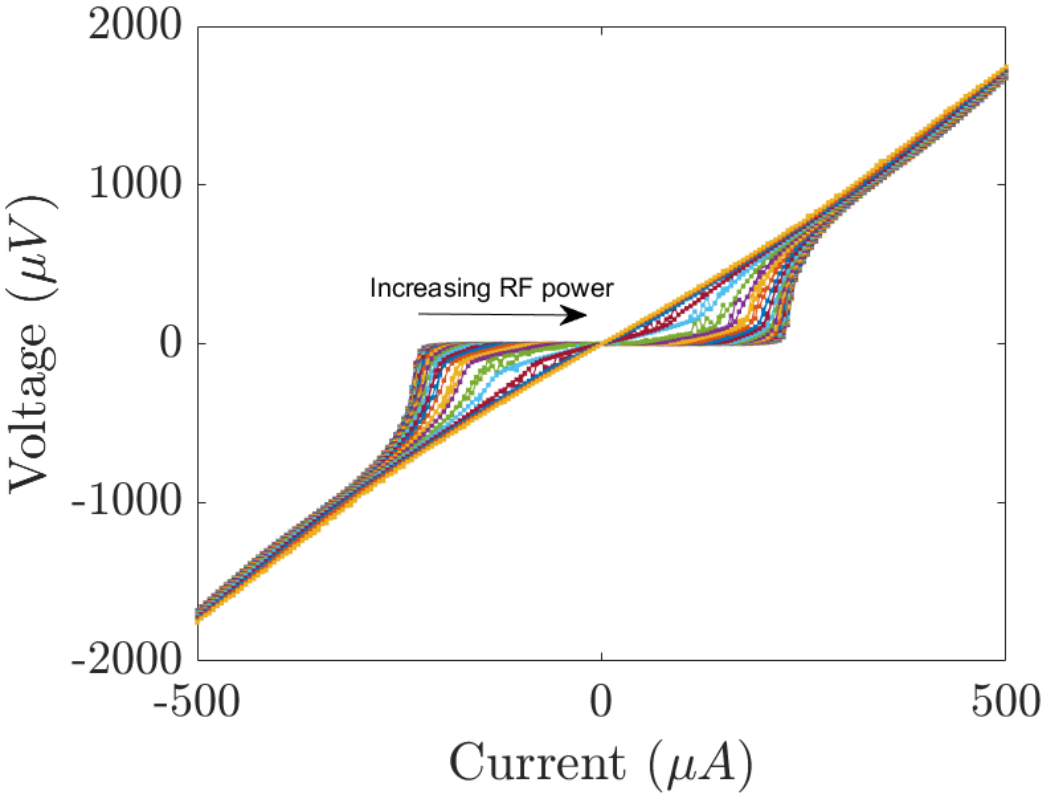

Figure 5.10: Current-voltage characteristics of a JJ with area 56.25 μm^2 under RF irradiation at 1.391 GHz with applied powers ranging from -50 dBm to -13 dBm. The critical current is suppressed as the power is increased.

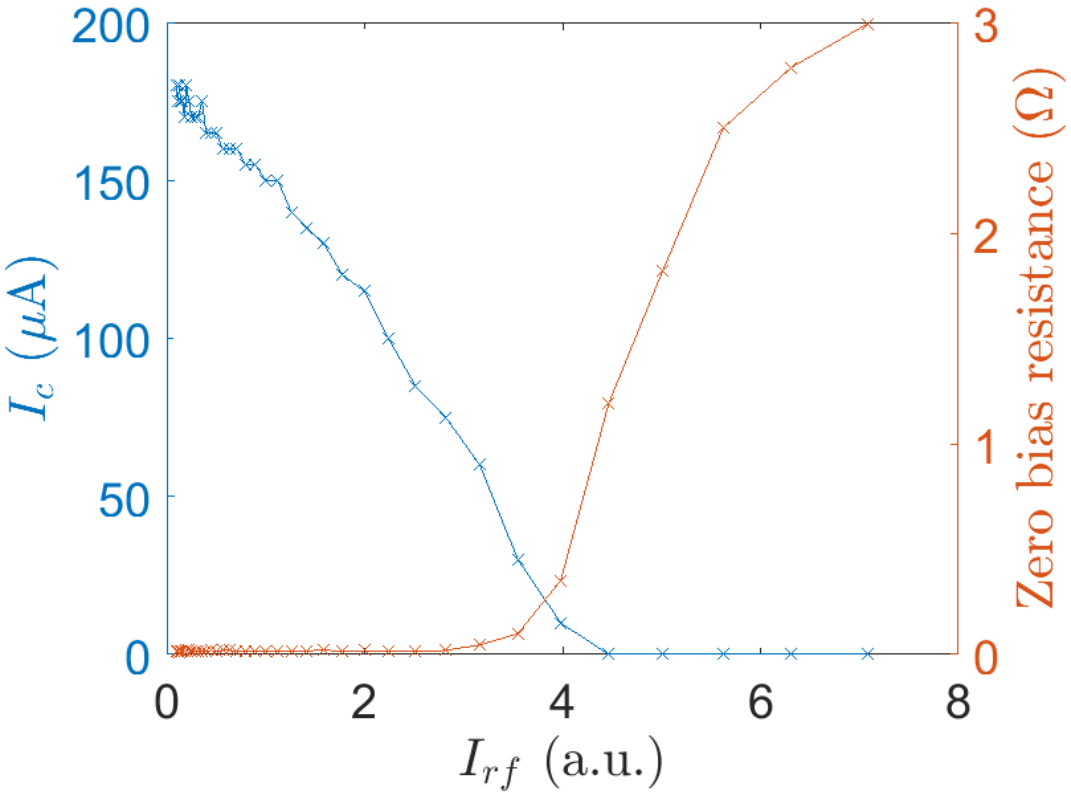

Figure 5.11: Critical current (in blue) and zero bias resistance (in orange) variation with applied RF current. Suppression of critical current and increase in zero-bias resistance due to RF fields coupling into junction

5.3 Discussion and Outlook

To conclude this chapter, we have developed a fabrication process for overlap Josephson junctions where the top and bottom electrodes are patterned separately in a sputtering system. We have characterised the resistances of samples with different processing conditions for the interface, in particular, using a back-sputter cleaning technique, we were able to significantly reduce the resistance of our metallic contacts. We were also able to perform a controlled oxide growth in both the low and high pressure regimes. In the low pressure regime, the oxide growth times needed to be quite long, for about 45 minutes, for some devices to exhibit a nonlinear IV characteristics at low temperatures. Only one in eight devices showed such characteristics. In the high pressure regime, we performed the oxide growth for five minutes, and the junction yield appeared to be improved greatly, most of the devices showed nonlinear IV characteristics. We have presented some representative current-voltage characteristics of these junctions, measured in a four-terminal configuration in the dilution refrigerator at 10 mK. We estimated the junction critical current density to be between 1 and 2 $\mu A/\mu m^2$, as needed for the capacitive coupler design in Chapter 4. We also found that irradiation by RF was able to suppress the critical current of the junction.

However, our junctions do not obey the Ambegaokar-Baratoff relation and have $I_c R_N$ products that are two to three times higher than theoretically predicted. This suggests that there are additional charge transport mechanisms across the barrier other than conduction via tunnelling, due to defects in the barrier such as weak points and pinholes[137]. This might also explain the higher β_c value obtained from our fit to the RCSJ model. As mentioned throughout the chapter, the engineering of the bottom electrode-oxide layer interface is crucial to determine junction properties. A common cause which degrades the interface quality are pinholes which causes short circuits through the oxide barrier. This could be caused by either increased surface roughness as a result of aggressive cleaning, or insufficient coverage by the oxide layer.

5.3 Discussion and Outlook

Although we were able to drastically reduce the resistance of our metallic contacts from backsputtering, the measured value is still on the order of a few ohms. This might be due to the increase in surface roughness or residual contaminants at the interface caused by redeposition in the chamber prior to the second layer being deposited. These causes cannot be ruled out without direct investigation into the structure of the tunnel barrier. Nevertheless, we have only systematically changed the backsputter time in this study, and the effect of backsputter pressure remains unknown. For instance, an approach in [138] by interleaving periods of cleaning with periods of rest to avoid sample heating allows sputter cleaning to take place for a longer time than ours. They also use a higher backsputter pressure $\approx$15 mTorr, but the system they used has a separate loadlock from the deposition chamber.

It is clear that the interface engineering remains a challenge and the process developed here is far from being a reliable route to high quality junctions for implementing the YY coupler circuits discussed in the previous chapter. This is in addition to design optimizations in the qubit-to-coupler and qubit-to-resonator couplings which might deviate from the simulations due to unaccounted stray capacitances in the geometry or systematic errors as a result of the fabrication process. We have anticipated some of these effects in the previous chapter, by simulating the stray capacitances to the ground plane and having designs to account for variations in JJ critical current density. Here it remains unanswered the question as to how best to make circuits that are tolerant to the inevitable imperfections caused by fabrication process.

In the next chapter, we shall describe the fabrication and measurement of QPS nanowire-based devices. The QPS nanowire is dual to the JJ, but has a much simpler structure in terms of fabrication. In particular, such interface engineering as described in this chapter is unnecessary as the entire structure of device is patterned in a single layer. From this perspective, devices based on nanowires are yet another route to achieve scalable superconducting and quantum circuits.

Chapter 6

Experiments on Quantum Phase-Slip Nanowire Devices

As we have seen in the introductory chapters, a quantum phase-slip (QPS) nanowire is a nonlinear capacitor. This property can be utilized as an element for a parametric amplifier. In this chapter, we report the development and experimental progress on the application of the QPS nanowire as a parametric amplifier. First, we discuss sample preparation and the fabrication of niobium nitride (NbN) nanowires using electron-beam lithography (EBL) and reactive-ion etching (RIE). We then present two variants of the prototype parametric amplifier— one with a single nanowire shunting the superconducting resonator, and a gate tuneable variant which consists of two nanowires in series. Next, we describe our experimental setup for carrying out RF characterisation of the samples at milliKelvin temperatures. Finally, we present and discuss the measurement results of both variants.

6.1 Device Fabrication

Our devices are made out of NbN on sapphire in a single-layer process. We clean the substrate and a thin layer of NbN is deposited, patterned and etched to form the features of our superconducting circuit. In this section, we describe the details of this process[139], developed by Dr. Jamie Potter, who kindly provided unpatterned NbN thin films for our devices.

6.1.1 NbN Deposition

The NbN thin film is grown on a polished sapphire wafer. The substrate was chosen as it is a low loss dielectric, and it is polished to improve the surface quality for further processing. The wafer is diced into 8 x 8 mm chips and they are first cleaned with de-ionised (DI) water to remove carbon dust. The chips are then placed into a beaker to be sonicated for five minutes each in acetone and then isopropanol (IPA). They are then blow dried with a nitrogen gun and placed into a plasma asher. The samples are ashed in O_2 plasma for 2 minutes to remove any organic materials from the substrate.

After preparing the substrates, they are transferred into a sputter deposition system. Similar to the sputtering process described before, deposition takes place in a chamber at high vacuum, and argon gas is flowed into the chamber where a high voltage ionizes it. The plasma is ignited and directed towards a niobium target. To deposit NbN, nitrogen gas is introduced in addition to argon in a 1:1 ratio which reacts with the niobium to form the compound. For our system, we first pump the system down to a base pressure of $4 \cdot 10^{-7}$ mbar and then both gases are flowed at 50 sccm to achieve a sputter pressure of $5 \cdot 10^{-3}$ mbar. The power used for sputtering is 150 W. The sample stage is water-cooled to keep the substrate at a constant temperature and rotated to coat the sample more uniformly. These parameters give us an estimated sputter rate of 10 nm/min. We verify this by sputtering for one minute and measure the film thickness to be 10 nm on a step profilometer.

6.1.2 NbN Patterning

To pattern the film, we perform electron-beam lithography (EBL) using poly(methyl methacrylate) (PMMA) resist as an etch mask for subsequent reactive-ion etching. The EBL process used for this is a two-beam current method with a larger 20 nA beam current for gross features and smaller 500 pA current for the nanowires. We spin-coated PMMA 950 A2 resist onto the sample and baked for 5 minutes at 180°C. The sample is then loaded into the Elionix ELS G100 system, where the resist is exposed in a pattern determined by the user's design. The parameters are shown in Tables 6.1 and 6.2 for the large and small current exposures. After the exposure has completed, the resist is ready to be developed in a mixture of methyl isobutyl ketone (MIBK) and IPA in a 3:1 ratio for 30 seconds. The sample is then soaked in IPA for a further 30 seconds to stop the development.

Parameter	Value
High beam current	20 nA
Dot number	500,000 dots
Field size	250 μm^2
Scan/feed pitch	60 nm/dot
Areal dose	800 $\mu C/\mu m^2$

Table 6.1: High beam-current dose settings used for EBL exposure in the Elionix ELS G100 system.

Parameter	Value
Low beam current	500 pA
Dot number	500,000 dots
Field size	250 μm^2
Scan/feed pitch	1 nm/dot
Areal dose	800 $\mu C/\mu m^2$

Table 6.2: Low beam-current dose settings used for EBL exposure in the Elionix ELS G100 system.

The sample is then transferred into a reactive-ion-etcher. For our recipe, we use CHF_3 and SF_6 to etch NbN, flowed at a rate of 35 sccm and 14 sccm respectively. The chamber pressure is maintained at 100 mTorr during the process. An RF power of 100 W is used to ignite the plasma and is directed by a DC bias voltage of 185 V towards the sample, which is in contact with a sample holder

water-cooled to 20°C throughout the etch. We first prime the chamber by running this recipe without the sample to prepare the surfaces of the chamber to improve the consistency of the etch recipe. To etch the sample, we load it into the process chamber and pump the chamber to base pressure. When that is completed, the automated etch process is then run.

6.2 Chip Design and Variants

6.2.1 Single-Nanowire Device

The first device variant is comprised of a feedline capacitively coupled to a quarter wavelength resonator. The resonator is shunted with the nanowire at its open-circuited end, where the amplitude of the voltage standing wave is maximum. This variant of the device was designed and fabricated by Dr. Freya Johnson. The device layout, shown in Figure 6.1, is designed using GDSII layout editor KLayout as depicted in the top row.

The blue box indicates the location of the nanowire, where a close-up is shown in the top right figure. The grey layer in the layout are parts exposed to the electron beam in the EBL system. The bottom row figures show scanning electron microscopy (SEM) images of the device after fabrication. The light grey areas show the exposed sapphire substrate after the NbN layer, shown in dark grey, has been etched. The yellow box shows a close-up of the nanowire which was measured to be about 30 nm in width, consistent with previous runs using the same method which had a linear offset to the fabricated width from the designed values[139]. The nanowire length is designed to be 200 nm. The rest of the CPW dimensions of the layout are shown in Table 6.3.

Parameter	Value
Feedline Width, w_f	50 μm
Feedline Gap, s_f	30 μm
Coupling Capacitor Length, l_c	50 μm
Resonator Width, w_r	10 μm
Resonator Gap, s_r	5 μm

Table 6.3: Designed CPW dimensions for the feedline, resonator and coupling capacitor to the resonator.

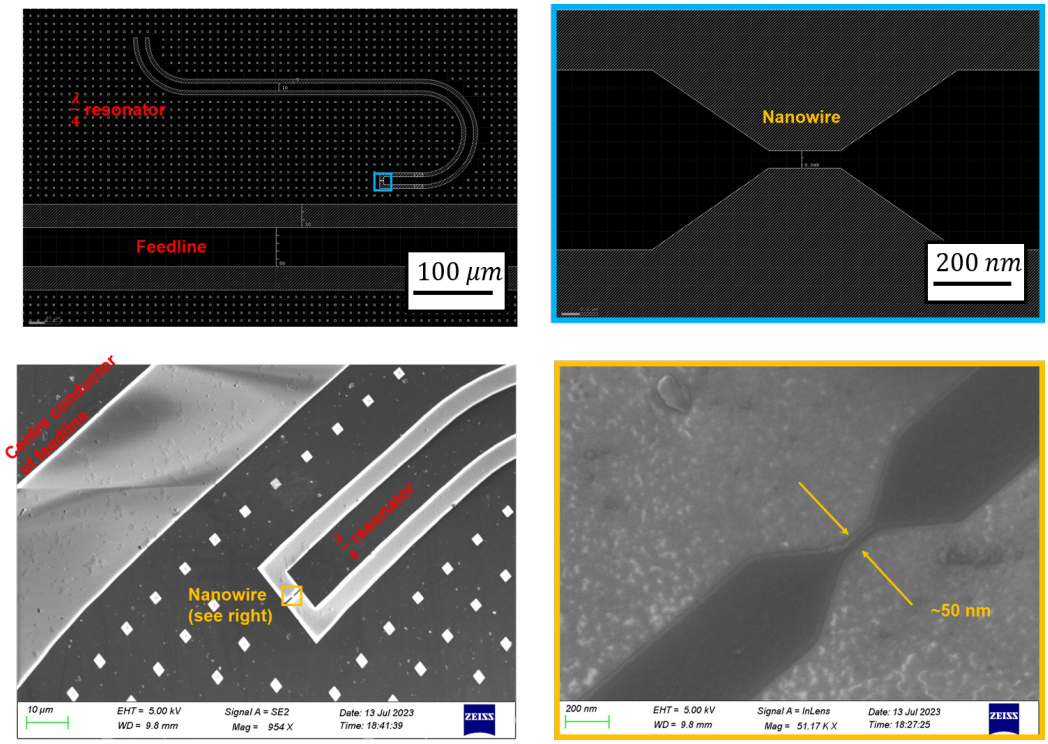

Figure 6.1: Design and scanning-electron micrographs of the single-nanowire device. Top left: Designed GDSII layout of the single-nanowire device showing the feedline capacitively coupled to a quarter-wavelength resonator. The regions shaded in grey correspond to those parts of the film which will be etched away. The blue box indicates the location of the nanowire. Top right: A close-up of the nanowire in the layout. Bottom left: SEM image of the fabricated device. Portions of the feedline and quarter-length resonator can be seen. Bottom right: A close-up of the yellow box shows the nanowire.

The capacitance of our resonator is estimated for our geometry using an analytical model derived from conformal mapping techniques[140][141]. The capacitance per unit length of a coplanar waveguide with centre conductor width w, separated from lateral ground planes by a gap s is

$$C_l = 4\epsilon_0\epsilon_{eff}\frac{K(k_0)}{K(k_0')}, \tag{6.1}$$

where k_0, k_0' are related to the geometry through

$$\begin{aligned} k_0 &= \frac{w}{w+2s}, \\ k_0' &= \sqrt{1-k_0^2}, \end{aligned} \tag{6.2}$$

and K is the complete elliptical integral of the first kind. The effective permittivity in general also depends on the geometry, but for our case is well approximated by $\epsilon_{eff} = \frac{1+\epsilon_1}{2}$, where ϵ_1 is the permittivity of the substrate[141]. The inductance of the line is mostly dominated by kinetic inductance, and inferred from previous characterisation of NbN thin film resonators[139]. The coupling capacitance, C_c, between the feedline and resonator, is simulated using Ansys Electronics Desktop 3D Electrostatic Analysis and found to be 0.58 fF.

Based on these estimates, we predict that the resonator has capacitance per unit length, $C_l = 135$ pF/m and inductance per unit length, $L_l = 27$ μH/m. We proceed by calculating the transmission line parameters of the resonator. From our estimates, the resonator has a characteristic impedance of $Z_0 = \sqrt{\frac{L_l}{C_l}} \approx 450\ \Omega$, the wavenumber is $\beta = \omega\sqrt{L_l C_l} = 377f\ m^{-1}$ where f is the operation frequency in GHz. Neglecting losses, the input impedance at node 1 as shown in Figure 6.2a can be found to be

$$Z_{in} = jZ_0 \frac{(b_c + b_{NW})\tan\beta l - 1}{b_c(1 - b_{NW}\tan\beta l)}, \tag{6.3}$$

where $b_i = \omega Z_0 C_i$, is the normalized susceptance of the capacitor C_i. The magnitude of Z_{in} is plotted as a function of frequency in Figure 6.2c where the black dashed line shows the resonance condition, which occurs when the input impedance is zero. The nanowire is indicated by the diamond-shaped symbol and we use $C_{NW} = 40$ aF in these simulations. The blue line is direct plot of relation (6.3), while the orange line is a plot of the input impedance, where the resonator is replaced with its lumped circuit equivalent, with $C = \frac{\pi}{4\omega_0 Z_0}$ and $L = \frac{1}{\omega_0^2 C}$ where ω_0

is the unloaded resonance frequency of the resonator, in the absence of coupling. This justifies the replacement of the transmission line resonator with the LC resonator as depicted in Figure 6.2b. Furthermore, from the relationship between the impedance matrix and scattering matrix of a two port[142], we find that the transmission coefficient is simply $S_{21} = \frac{2}{2+\frac{Z_0}{Z_{in}}}$, which is plotted in Figure 6.2d.

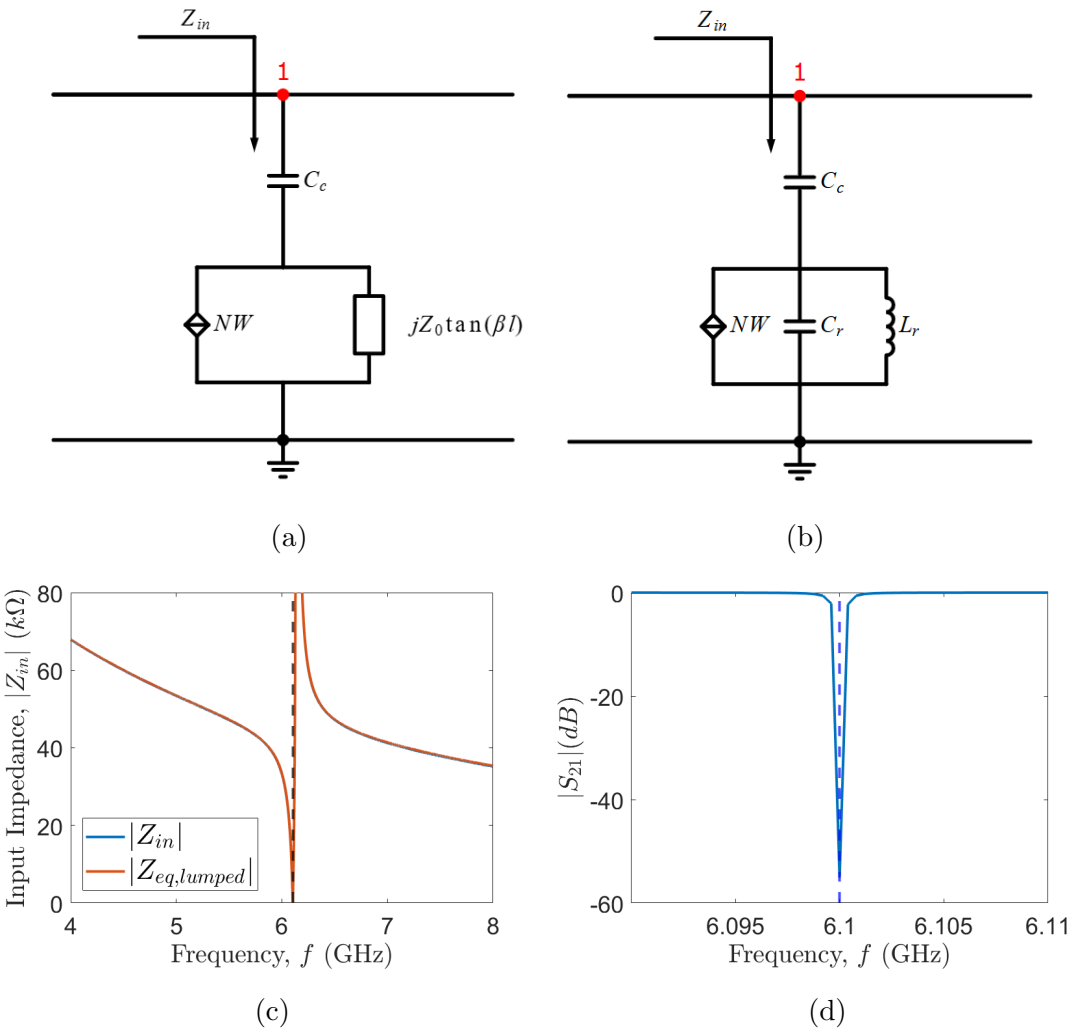

Figure 6.2: (a) Circuit model of the device at the node where the single-nanowire device couples to the feedline through coupling capacitor C_c. Here the impedance of a distributed-element resonator is shown and the nanowire is represented as a tuneable capacitor. (b) Circuit model of device with the resonator is replaced by its lumped-element equivalent. (c) Plot of the input impedance at node 1 calculated using the distributed-element impedance of the resonator (in blue) and using the lumped-element equivalent (in orange). Lines are stacked on top of each other. (d) Calculation of $|S_{21}|$ from the input impedance in the lumped-element model.

6.2.2 Gated Double Nanowire Device

The second variant we have fabricated is just like the first, except the single nanowire has now been replaced by two nanowires. The node connecting the two nanowires is a superconducting island that is made large enough to prohibit phase-slips. It is capacitively coupled to a gate electrode which allows us to apply a voltage that induces charges on the island. Figure 6.3a illustrates the layout of the device, where the blue box is enlarged in Figure 6.3c. The red layer is to be exposed, and the remaining black features represent the superconductor and nanowires. The SEM image of the completed device after fabrication is shown in Figure 6.3d. Following our discussion of the single nanowire case, the equivalent circuit of this device is shown in Figure 6.3b.

The capacitances from the island to other parts of the circuit have also been model using Ansys Electronics Desktop 3D Electrostatic Analysis, with $C_{i,gate} = 37\ aF$ and $C_{i,ground} = 76\ aF$.

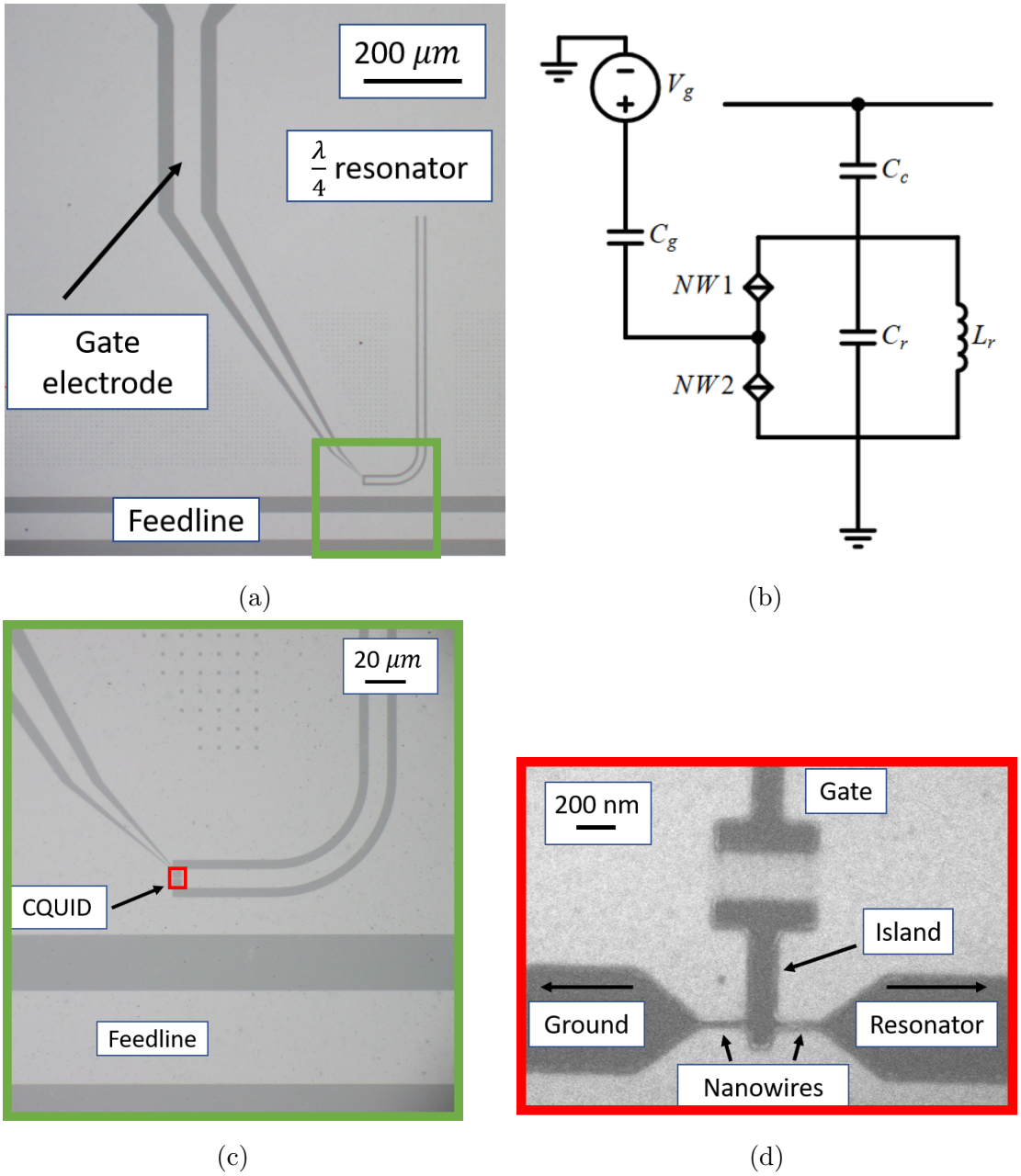

Figure 6.3: (a) Designed GDSII layout of the gated double nanowire device. The gate electrode is partially shown. Blue box shows the location of the two nanowires. (b) Circuit model of the device. An external voltage V_g is shown being applied through the gate electrode and gate capacitor C_g. (c) A close-up of the designed nanowires. The island between the two nanowires is coupled capacitively to the gate electrode. (d) SEM image of the gated double nanowire structure.

6.3 Experimental Setup

Here we describe the experimental setup used to obtain the subsequent measurement results. All our measurements are performed in an Oxford Instruments Triton 500 Dilution Refrigerator normally operated at 15 mK in the LCN Lab 2.06.

After fabricating the devices, they are mounted onto a sample box using GE varnish, which is an adhesive that maintains good thermal conductivity at cryogenic temperatures. The sample box contains a printed circuit board (PCB), which routes the signal from the sample to the external measurement apparatus. The sample box is also lined with Eccosorb, an absorber of electromagnetic energy. Wirebonds are placed to make the necessary connections from the sample to the PCB. The box is then covered and mounted onto the copper bracket that hangs from the mixing chamber plate of the dilution fridge. The sample space is then enclosed in two cylindrical shields to minimize stray magnetic fields affecting our experiments. The inner shield is made of aluminium, which expels magnetic field below its transition temperature. The outer shield is Amumetal A4K, a high permeability mu-metal alloy, which redirects magnetic fields away from the sample space.

RF signals in and out of the fridge are carried by semi-rigid coaxial lines as illustrated in Figure 6.4. The input line is heavily attenuated to reduce any noise generated by black body radiation which can couple to the input of sample. There is 60 dB attenuation in total, with 20 dB attenuators placed on the input line at the 4 K, 1 K and 100 mK stages. Additionally, the semi-rigid coaxial cables introduce about an extra 5 dB attenuation per stage, or 25 dB in total. To detect these weak signals through our samples, we place a travelling wave parametric amplifier (TWPA) right at the sample output which provides around 25 dB gain. This acts as a low noise amplifier which boosts our signal-to-noise ratio for further amplification at the later stages. The TWPA requires a pump tone which is supplied by a Rohde & Schwarz SGS100A RF source. An additional RF line is used to supply the pump to the TWPA, which is coupled to it via a directional coupler in the

sample space. The input and output to the TWPA are connected to cryogenic RF isolators which ensure that external noise does not propagate down into the TWPA from the output line, and that any signals at the input of the TWPA are not reflected back into the sample. A high electron mobility transistor (HEMT) on the 4 K plate provides another 20 dB gain.

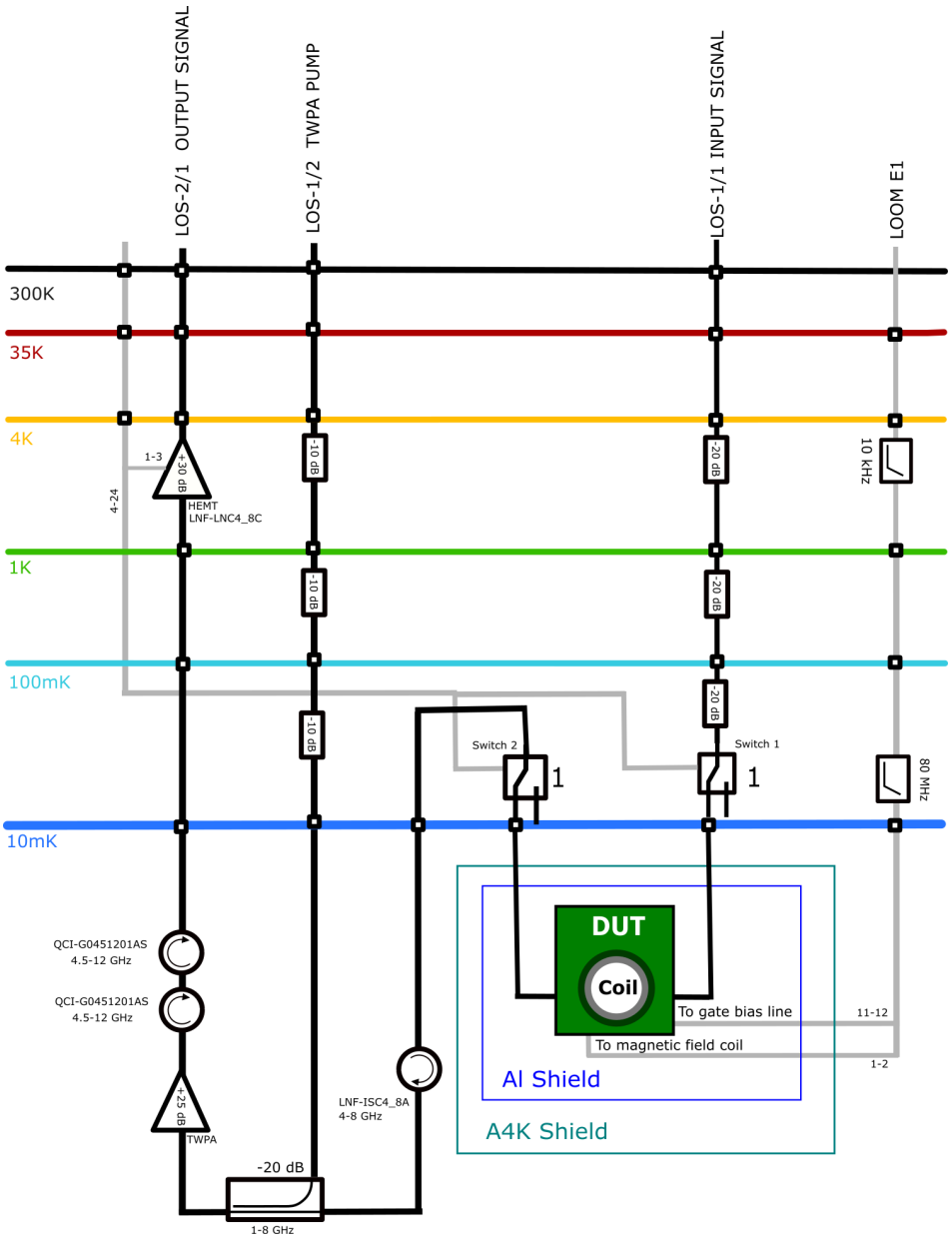

Figure 6.4: Experimental setup inside the Oxford Instruments Triton 500 Dilution Refrigerator. The input and output RF lines are shown connected to our device-under-test (DUT) inside the sample shields. A filtered voltage bias line is connected to our sample box, which is used to apply the gate voltage.

6.4 Measurement Results

6.4.1 Single-Nanowire Device Measurements

Low Power Resonance Curve

First we present the measurements of the transmission coefficient S_{21} through the single-nanowire device using the Keysight E5080A ENA Vector Network Analyzer. For a resonator in a notch configuration, the resonance curve is given by[143][144]

$$S_{21}(f) = ae^{i\alpha}e^{-2\pi if\tau}\left[1 - \frac{(\frac{Q_l}{|Q_c|}e^{i\phi})}{1 + 2iQ_l(\frac{f}{f_r} - 1)}\right], \tag{6.4}$$

where τ is the phase delay, α is the initial phase of the signal, and a is the attenuation (or gain) of the signal. These all account for parameters external to the resonator. The square bracketed expression is the S_{21} of an ideal resonator for this configuration. The probe frequency is f and resonance frequency is f_r. The loaded quality factor is Q_l and the coupling factor is $Q_c = |Q_c|e^{i\phi}$. The phase factor $e^{i\phi}$ accounts for the asymmetry of the resonance as a result of impedance mismatches in the input and output lines. This model is also used as the basis for fitting algorithms developed in [143], based on the resonance circle on the complex S_{21} plane.

Figure 6.5 shows the magnitude and phase of the S_{21} through the single-nanowire device. The cyan dots are measured VNA data and the solid red lines are from the fit. In this measurement, the VNA source power is -50 dBm. From the fitting model, we extract a resonance frequency of 5.0552 GHz and intrinsic quality factor of 9800. The resonance frequency is lower than the designed value of the quarter-length resonator, which is in the range of 6 to 7 GHz. The intrinsic quality factor, Q_i we find is about an order of magnitude lower than typical superconducting resonators reported in the literature. Even some NbN resonators fabricated in our cleanroom before had exhibited $Q_i > 10^5$, while other resonators with intrinsic quality factors on the order of 10^3 have also been observed, attributed to potential

contamination in the sputtering chamber[139].

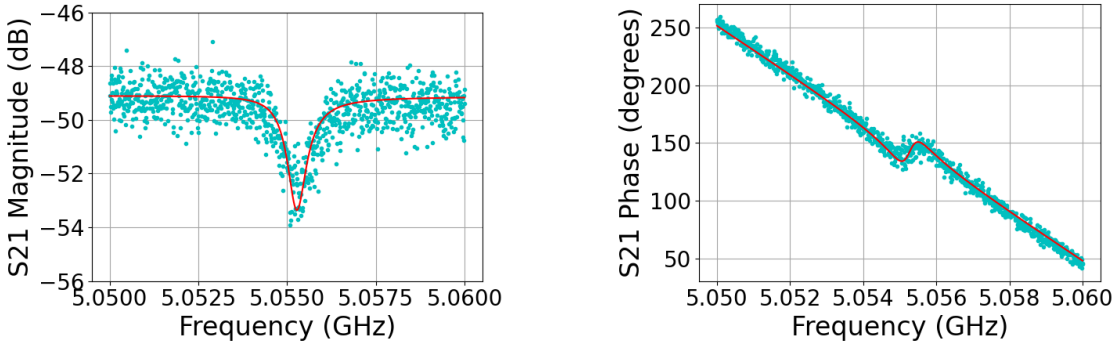

(a) (b)

Figure 6.5: Cyan dots show the measured S_{21} magnitude and phase of the gated device at -50 dBm VNA power and red curves show fit to the data using algorithm from [145].
(a) Magnitude of the S_{21}. (b) Phase of the S_{21}. The measurements are taken at 10 mK in a dilution fridge and the device is enclosed in a sample shield to minimize unwanted coupling to stray fields.

Nonlinear Power Dependence

The power dependence of the resonator was measured using a VNA, with powers from -50 dBm to -25 dBm in 1 dBm steps. The results are shown in Figure 6.6. Figure 6.6a shows a colour plot of the S_{21} magnitude from 5.05 GHz to 5.06 GHz with increasing VNA power in the vertical axis. Figure 6.6b shows a selection of these curves at different powers, demonstrating the decrease in resonance frequency by about 4 MHz as the power increased by 20 dB. This behaviour is characteristic of the driven Duffing oscillator discussed in the introduction, where the critical power occurs at -45 dBm, above which the resonance curve starts to distort.

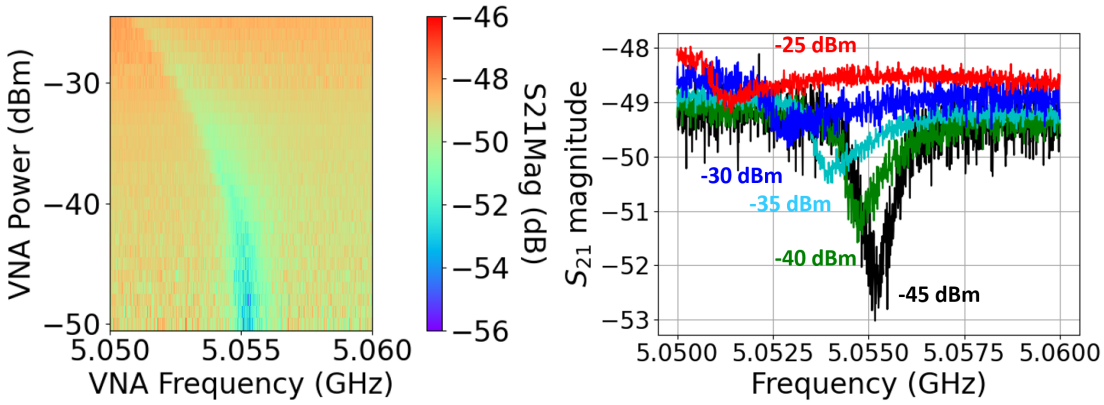

(a) (b)

Figure 6.6: Single-tone power dependence of the single-nanowire device. (a) Measurement of the power dependence of the S_{21} magnitude of the single-nanowire device. (b) S_{21} magnitude of the device for powers from -45 dBm to -25 dBm with a 5 dBm spacing.

Mixing

Figure 6.7 shows the VNA measurement of the single-nanowire device with a pump tone applied through a directional coupler. The pump frequency is varied in this measurement as shown in the vertical axis. The VNA power is -40 dBm and the pump power is -30 dBm (which includes coupling losses from the directional coupler). The pump tone is applied in a 10 MHz bandwidth centered at 5.055 GHz, which can be seen across the diagonal of the figure. To obtain the plot as shown, a pump frequency is set, then the VNA frequency is swept from 5.05 GHz to 5.06 GHz. When the pump frequency is near resonance, the resonance frequency changes discontinuously. It decreases suddenly, and as the pump frequency is further detuned, the resonance frequency returns to its original value, another indication of the nonlinearity in the resonator as seen earlier.

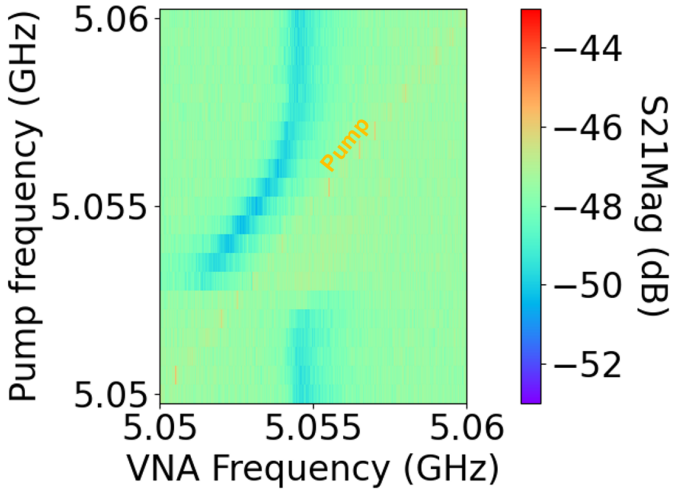

Figure 6.7: Pump-power dependence of the single-nanowire device in a two-tone experiment. Measurement of the S_{21} magnitude in response to an additional tone applied near the resonance frequency.

The VNA source and receiver frequencies are identical in this experiment, which means that only the transmission at this selected frequency is being measured. In order to measure any mixing products as a result of the interaction between the signal and pump tones, we measure the power spectrum of the device output. We

perform this experiment by combining the two tones through a directional coupler as before and measuring the output power using an Advantest R3271A Spectrum Analyser. Firstly the pump-power dependence is investigated. The pump tone is chosen to be near the resonance, fixed at 5.054 GHz, and the signal tone is set to be at a fixed detuning of +100 kHz from the pump. The signal tone is applied at a fixed power at -25 dBm, while the pump power is varied from -20 dBm to 5 dBm. Figure 6.8a shows the appearance of an idler tone as the pump power exceeds about -2 dBm. The idler and signal components are symmetric about the power tone, with the idler frequency being at $f_i = 2f_p - f_s$.

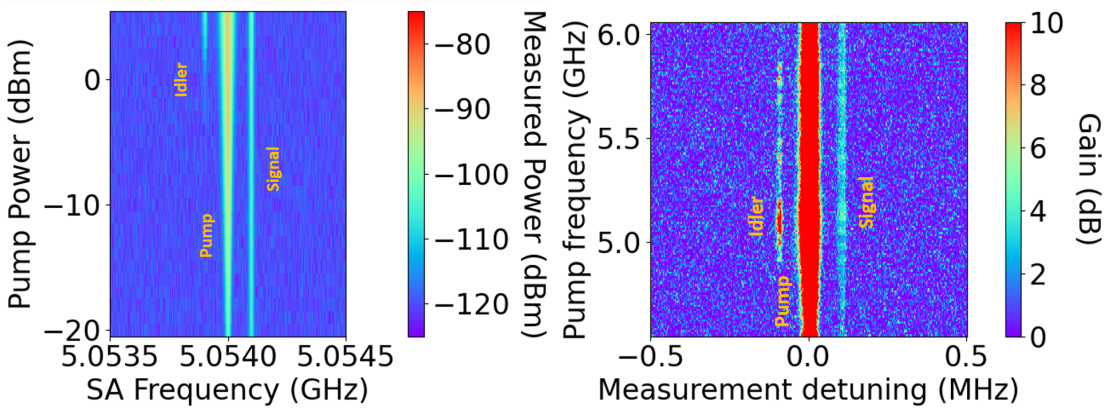

Figure 6.8: (a) Measurement of the pump-power dependence of the idler tone when the detuning between the signal and pump tones is fixed at 100 kHz.
(b) Measurement of the pump-frequency dependence of the idler tone. The detuning between the signal and pump is fixed, but both are swept across a broad frequency range.

Next, we investigate the frequency dependence of this effect. For this measurement, the pump and signal tones are kept at a fixed detuning of 100 kHz, while both are swept across a 1.5 GHz bandwidth. The pump power is fixed at 3 dBm, and the signal power at -25 dBm. The spectrum analyser then measures around a 1 MHz bandwidth centered on the pump frequency. Here we characterise the gain, which is obtained by subtracting the two-tone spectrum from the control

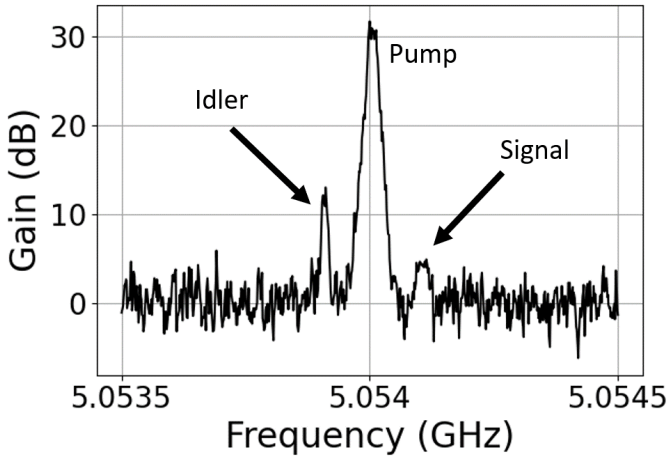

Figure 6.9: Measurement of the signal gain of the single-nanowire device. The data is a horizontal slice of the data in Figure 6.8b. The pump frequency is 5.054 GHz, pump power is 3 dBm, and the signal power is -25 dBm.

consisting of only the signal without any applied pump. The result is shown in Figure 6.8b and we see that the idler power is highest around the vicinity of the resonance frequency of the device, where the gain is about 5 dB. In Figure 6.9 we show a horizontal cross-section of the plot in Figure 6.8b at a pump frequency of 5.054 GHz where the idler gain is maximum.

Thus, we see that the mixing effect is most prominent in the spectral vicinity of the resonator and combined with the new generated frequency component, these results strongly suggest that a degenerate four-wave mixing process is induced by the nonlinear resonator. Although this is the case, we cannot yet attribute this nonlinearity to the nanowire capacitance, as there may be other sources of nonlinearity, such as in the kinetic inductance of the film, which has the same character, driven nonlinear by a large current. To show that the nanowire is responsible for this behaviour, in the next section we present results of experiments on a variant of this device, containing two nanowires and an island, to which a gate is capacitively coupled. This allows us to set the voltage across the nanowires directly.

6.4.2 Gated Double Nanowire Device Measurements

In this section we present measurements of the gate tuneable response of the gated double nanowire device. First we characterise the device using a VNA as before in the absence of any applied gate voltage. The power dependence is shown in Figure 6.10a. We found that the resonance frequency of this device was much lower than expected, resulting in lower transmission, band-limited by the circulators and HEMT at the output stage. The resonance frequency is 3.5475 GHz, with an intrinsic Q-factor of 4255, obtained from the fitting routine described earlier.

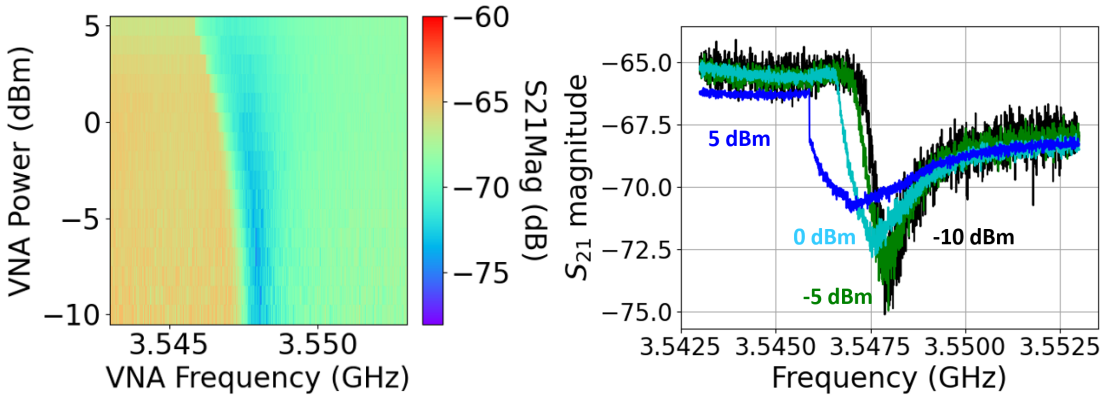

(a) (b)

Figure 6.10: (a) Measurement of the pump power dependence of the S_{21} magnitude of the gated double nanowire device. (b) S_{21} magnitude of the device for powers from -10 dBm to 5 dBm with a 5 dBm spacing.

Lock-In Detection

Next, we measure the response of the resonator as a voltage is applied to the gate of the device. We used a lock-in detection scheme, referenced to the frequency of the voltage applied to the gate, to improve the signal-to-noise ratio of our measurement. The measurement setup is shown in Figure 6.11. A continuous wave (CW) is generated by an R&S SGS100A SGMA RF source, which is split by the

power splitter. One output of the power splitter drives a MM1-0312HS Marki Microwave RF Double Balanced Mixer, while the other output is attenuated to a suitable power level by a programmable Vaunix LabBrick LDA 5018V Digital Attenuator to be sent through the feedline of our device-under-test (DUT). The frequency of this signal is set to be close to the operating frequency of the device around $f_{sig} = 3.545$ GHz. A Keithley 3390 Arbitrary Waveform Generator (AWG) supplies the sinusoidal voltage waveform that is applied to the gate contact, which is at a lower frequency at $f_{AWG} = 75\ Hz$. If the device responds non-linearly to the oscillating voltage, the amplitude of the output signal will be modulated, producing sidebands at $f_{sig} \pm f_{AWG}$, which are then demodulated by a double-balanced mixer, with the LO supplied from the same RF source as the signal. The resulting output of the mixer is then the envelope of the modulated signal, which is detected using a lock-in amplifier phase-locked to the AWG signal.

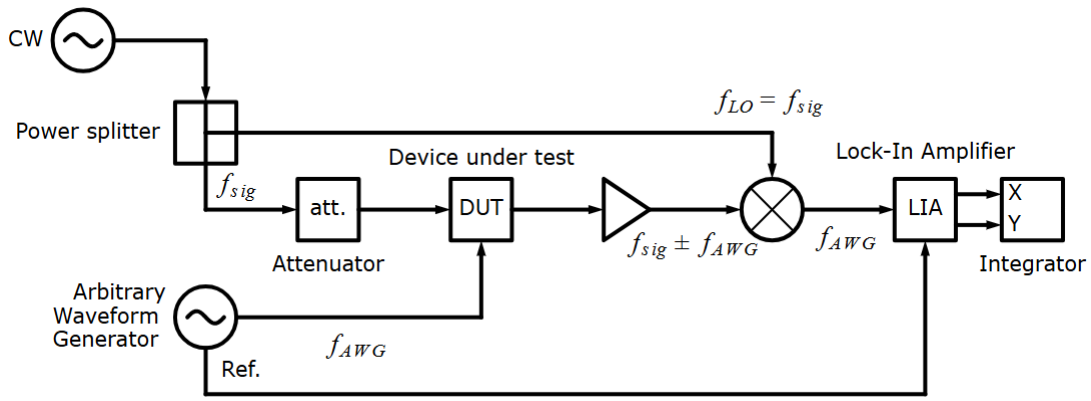

Figure 6.11: Schematic of the measurement setup for lock-in detection of the response of the device.

Input and Output Signals

The voltage supplied by the AWG can also be offset. Since the nanowires are voltage-tuneable capacitors, we can extract the capacitance change from the changes in resonator frequency. An example voltage waveform is shown in Figure 6.12, with an oscillating part that is fixed in frequency and amplitude, and an offset which changes stepwise over time.

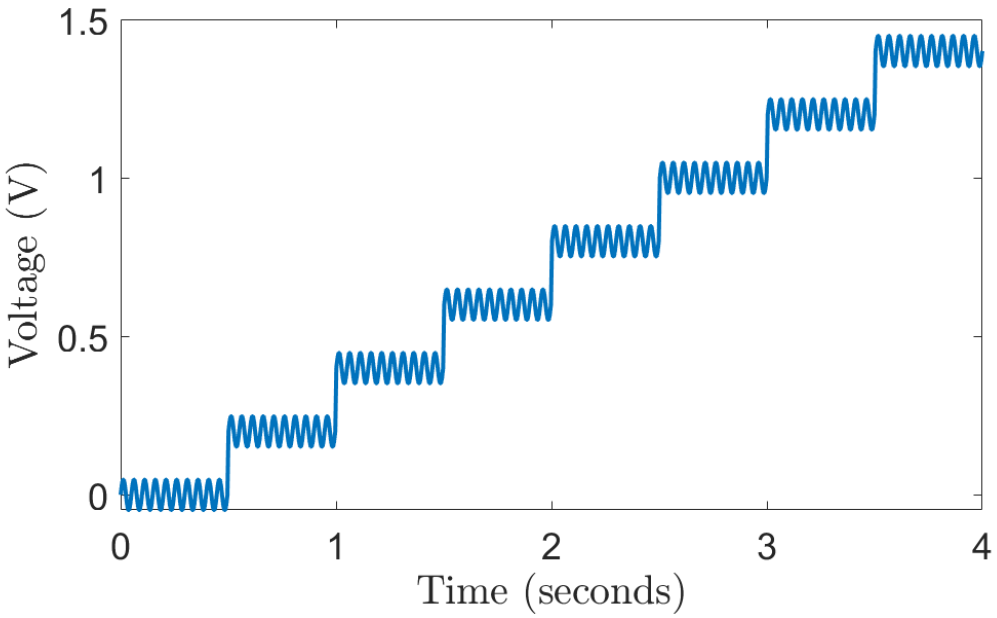

Figure 6.12: Illustration of the waveform used to perform voltage dependence measurements. The signal contains an oscillating part for phase sensitive detection and an offset which biases the device at different points of the voltage response curve.

Magnetic field response

If the oscillating voltage is small enough, the change in the resonance should be linear and hence the output voltage as a function of frequency should resemble the derivative of the transmission curve. Before we measured the electric field response of the device, we first verified the measurement technique by using a coil attached to the sample box, which produces a magnetic field when a current is sourced through it. A 1 kΩ resistor is connected in series with the AWG. The response of the device to applied field is large, which aids in the verification.

Figure 6.13 shows the comparison of the transmission curve data to the measured amplitude using lock-in detection. Figure 6.13a shows the normalized output voltage measured by the VNA and Figure 6.13b is its numerical derivative. Figure 6.13c is the magnetic field response of the device when the offset voltage is fixed at zero. The RF power used is 18 dBm, with the variable attenuator set to 37 dB. Including the power loss from the power splitter, the power to the input line is -22 dBm for this measurement, deep into the linear regime of the resonator. The oscillating voltage is set to 0.1 V peak-to-peak, corresponding to an oscillating current of 0.1 mA peak-to-peak. Figures 6.13b and 6.13c show identical features, namely a large peak corresponding to the first steep negative slope of the resonance dip and another smaller peak, corresponding to the shallower rising edge, with a drop to zero between the two peaks corresponding to the turning point of the curve. The measured magnitude response is not centered on the same frequency as the curve in Figure 6.13b, but is instead about 500 kHz lower.

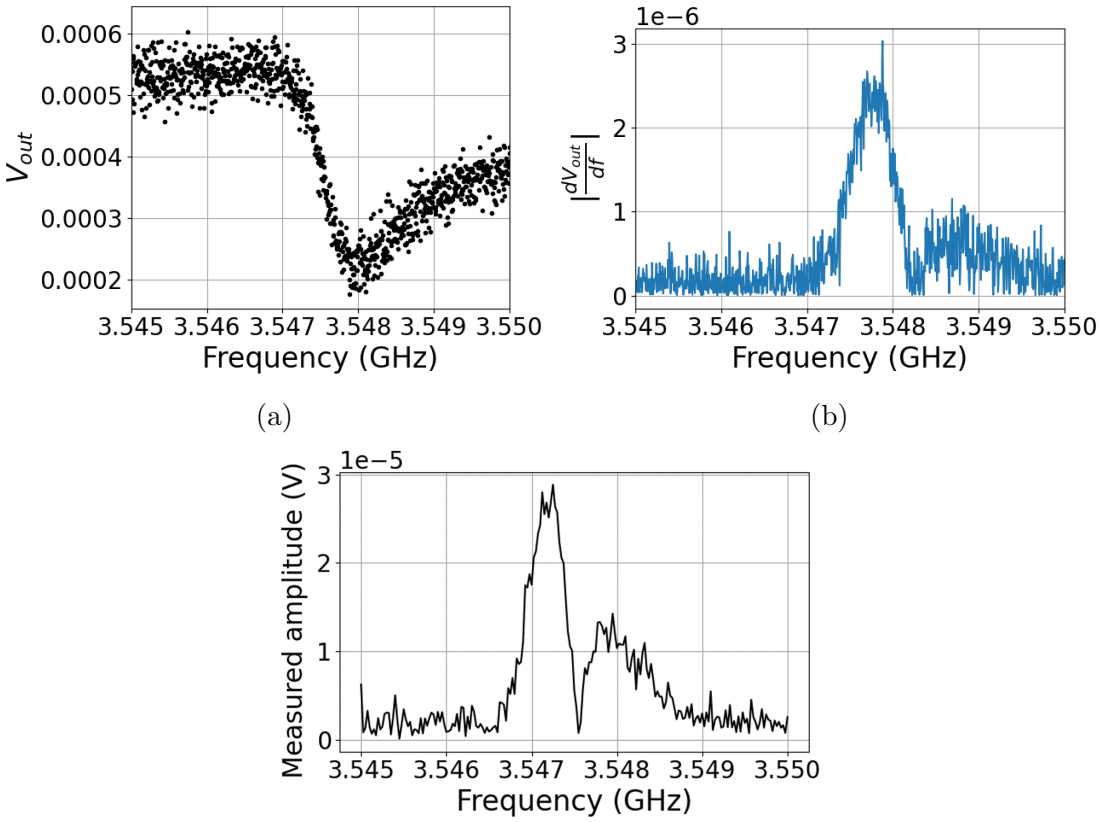

Figure 6.13: Comparison between the numerical derivative of the resonance curve and the magnetic field response. (a) The normalized output voltage obtained from VNA $|S_{21}|$ magnitude measurement of the gated device at a source power of -10 dBm. (b) The numerical derivative of the curve in (a). (c) The measured amplitude response of the device to a 0.1 mA peak-to-peak oscillating current using the lock-in detection scheme at zero bias current.

We then applied an offset current to the coil and measured the change in resonance curve. This current is first applied using a Keithley 6220 precision DC current source and a VNA is used to measure the S_{21} magnitude at a power of -10 dBm. Then using our lock-in setup, we vary the offset current in addition to the oscillating current applied to the coil. The results are presented in Figure 6.14 which show qualitative agreement, with similar hysteretic characteristics in both cases when the direction of current is changed.

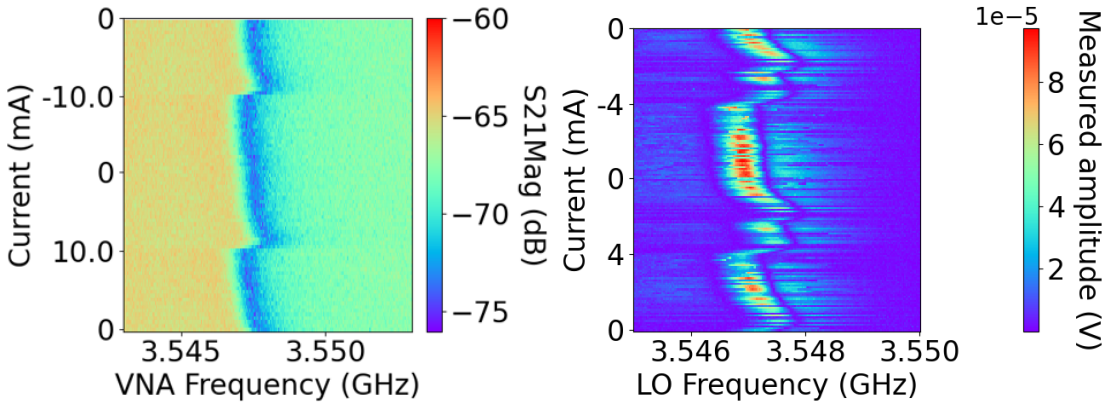

(a) (b)

Figure 6.14: Four-quadrant offset current waveform is applied to the sample coil to obtain the data shown in the figures. The measurement starts from the bottom of the figure and ends at the top. (a) VNA measurement of the magnetic field response of the device. (b) Measurement of the magnetic field response of the device using lock-in detection.

Thus in this section we have validated the measurement principle using lock-in detection. We showed that the measured amplitude by the lock-in amplifier has a strong signal in the spectral vicinity of the resonance frequency of the device. Furthermore, we demonstrated that the measured amplitude is related to the derivative of the output voltage with respect to RF frequency. We then are able to monitor changes in resonance frequency using this method. We use this technique to measure the electric field response next.

Electric field response

We characterise the electric field response of the gated double-nanowire device using the lock-in detection technique demonstrate in the previous section, but this time, the voltage is applied to the on chip gate bias line. We first demonstrate voltage sensitivity of the device as shown in Figure 6.15. The peak-to-peak oscillating voltage used for this measurement is 0.2 V and the RF power at the device input is 2 dBm. Figure 6.15a is the S_{21} data of the device at -1 dBm VNA power, and Figure 6.15b is the modulus of the numerical derivative of this curve. Figure 6.15c and 6.15d are the magnitude and phase of the signal measured by the lock-in amplifier at a fixed offset voltage of zero. As before, the magnitude signal resembles the modulus of the derivative curve. The measured phase changes by 180° when the slope changes sign. The strong signal near the resonance frequency shows that the resonator does responds to the oscillating voltage.

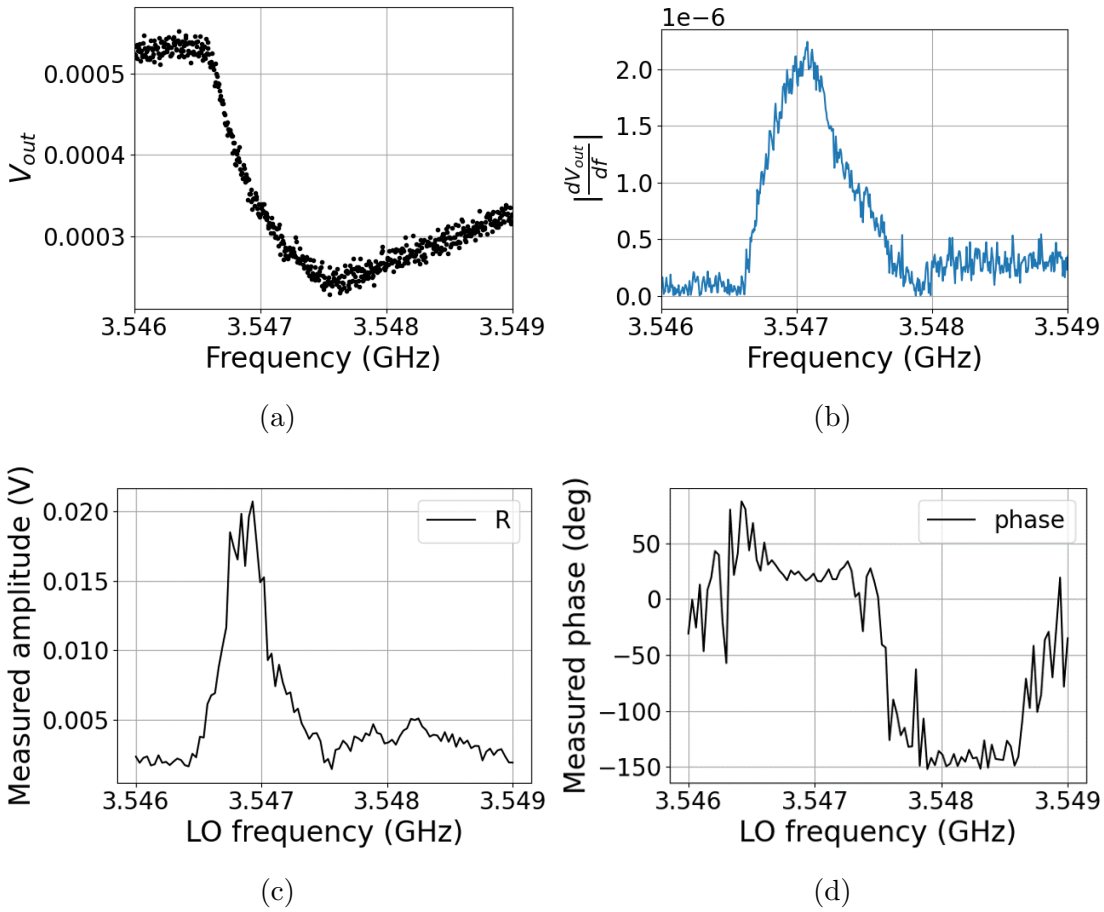

Figure 6.15: Comparison between the numerical derivative of the resonance curve and the electric field response. (a) Normalized output voltage obtained from VNA $|S_{21}|$ magnitude measurement shown in linear scale at a source power of -1 dBm. (b) Derivative with respect to frequency of the smoothed-out S_{21} curve. (c),(d) Measured magnitude and phase of the voltage response using the circuit of Figure 6.11 as a function of frequency at fixed bias voltage.

Voltage Periodicity

In this section we demonstrate the periodic tuning of the resonator with applied offset voltage. In the measurements that follow, the input RF power is 2 dBm and the peak-to-peak voltage is 200 mV. Figure 6.16 shows the signal measured by the lock-in detector, plotted as magnitude and phase in the colour axis. The x-axis is the signal frequency which is varied by 3 MHz from 3.546 GHz to 3.549 GHz, while the voltage offset is varied in the y-axis. The local minimum between the two peaks in the magnitude changes by about 1 MHz as the voltage is tuned by 160 mV, coinciding with the points where the phase signal changes by 180°. The data shows periodicity in both measured magnitude and phase as shown in Figures 6.16c and 6.16d, where we take a vertical slice of the data at a fixed frequency of 3.5473 GHz. In our experiments, we found that the results are independent of whether the frequency or the voltage offset is swept first, nor is it dependent on which direction the voltage offset is being swept.

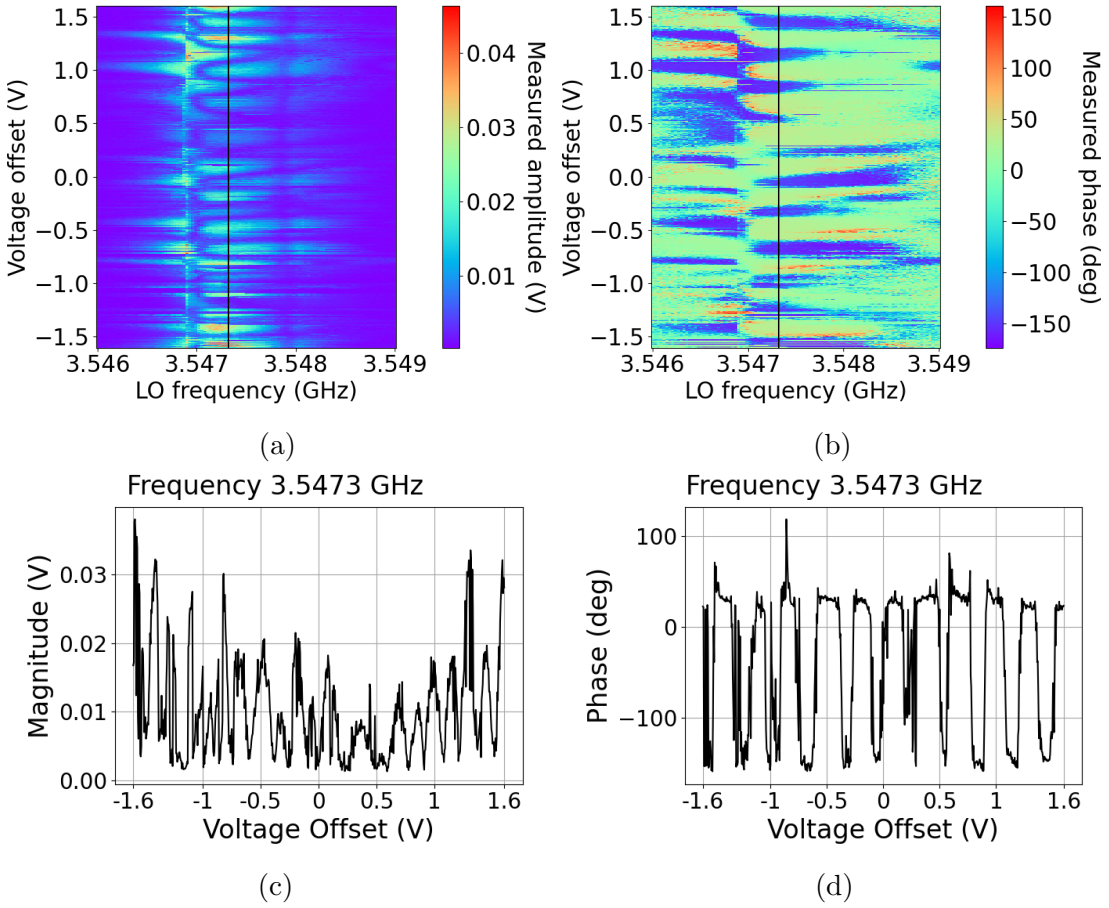

Figure 6.16: (a),(b) Measured magnitude and phase of the voltage response of the gated device by the lock-in amplifier as a function of voltage offset in the y-axis and frequency in the x-axis. (c),(d) Vertical sections of the figures in (a),(b) at a fixed frequency.

The periodicity is more apparent when plotted instead in the quadrature representation. Figure 6.17 shows the X and Y quadratures of the received signal. The vertical slices in Figures 6.17c and 6.17d show clear oscillatory behaviour in the voltage offset with a single period. This is as opposed to the magnitude response, which is always positive and hence contains frequency components at twice the oscillation frequency. We then take the FFT of these signals, as in Figure 6.18 to obtain the voltage period of 292 mV.

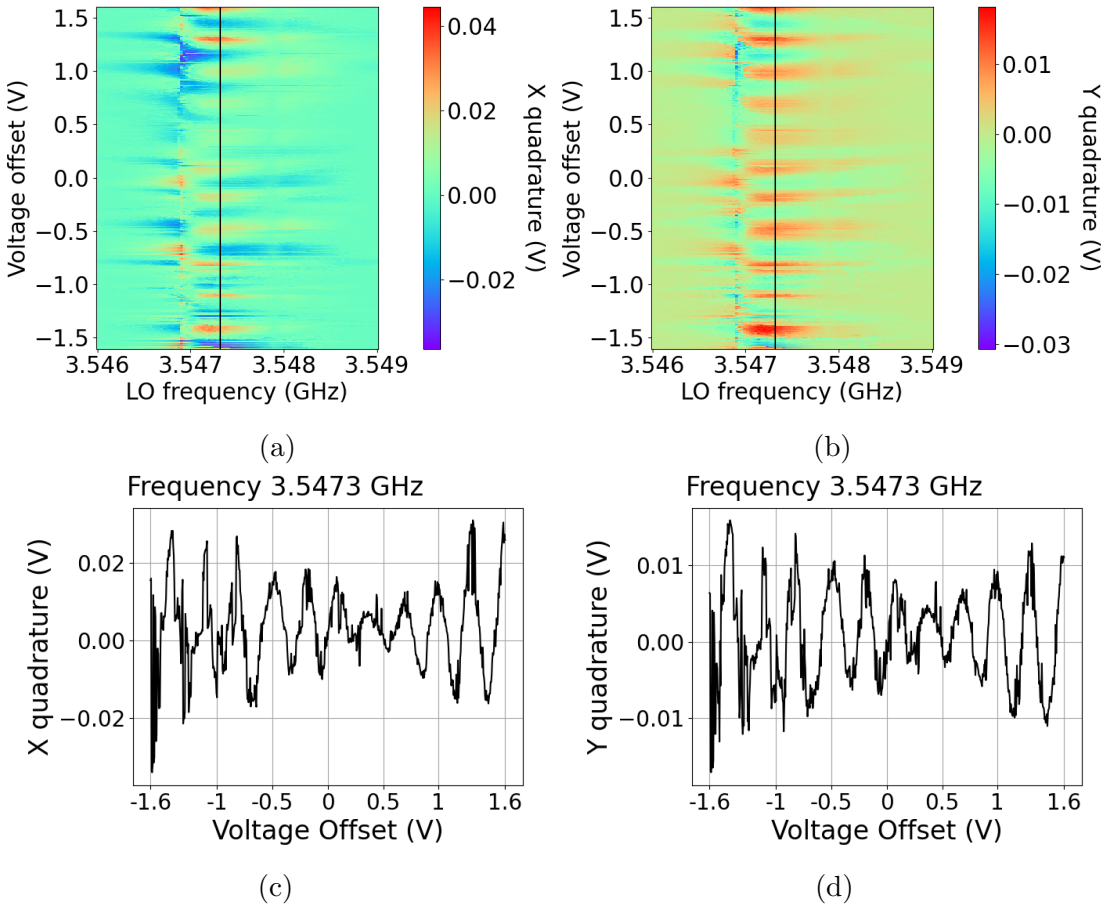

Figure 6.17: (a),(b) Measured X and Y quadratures of the voltage response of the gated device as a function of voltage offset in the y-axis and frequency in the x-axis. (c),(d) Vertical sections of the figures in (a),(b) at a fixed frequency.

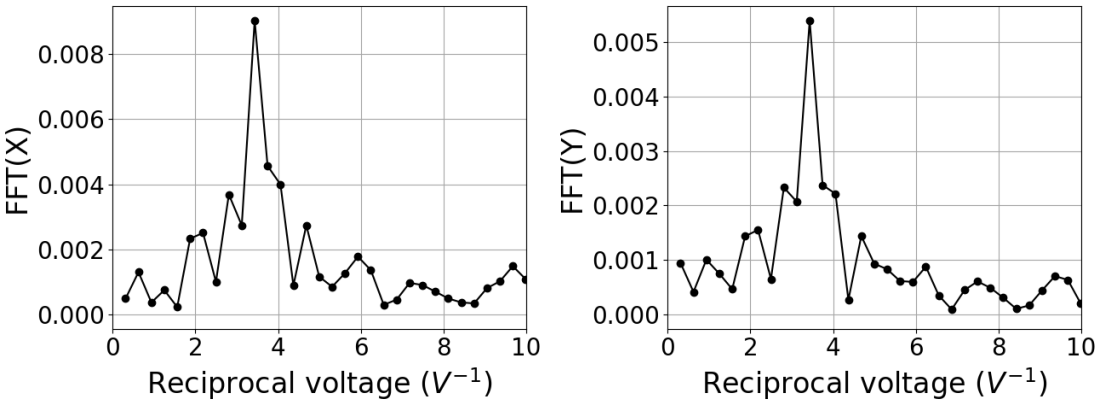

(a) (b)

Figure 6.18: Fast-fourier transform of the data from Figures 6.17c and 6.17d. A single peak is shown in both quadratures which gives a voltage period of 292 mV.

Analysis and Discussion

Since the quadrature data corresponds to the signed derivative of the resonance curve, in this section we analyse the integrated X and Y quadrature data to extract the resonator parameters. The integrated data is shown in Figure 6.19.

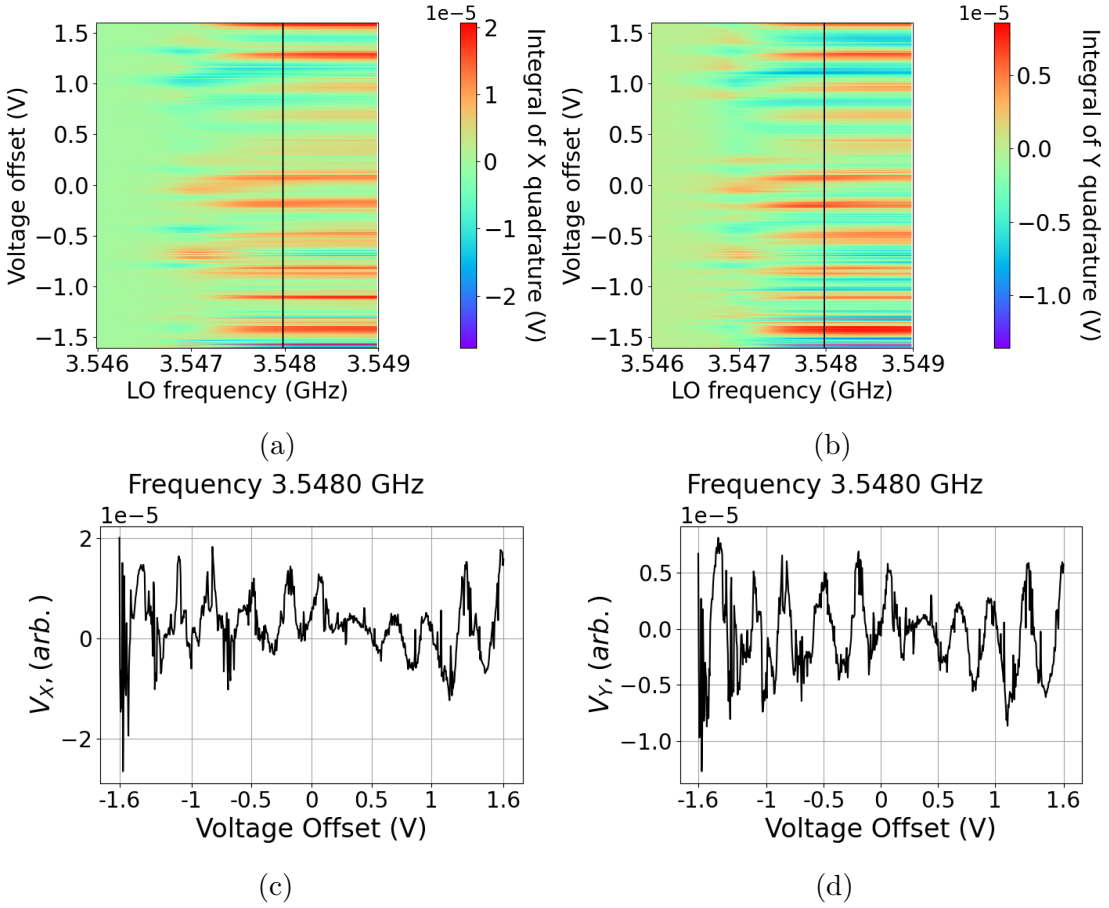

Figure 6.19: (a),(b) Integrated X and Y quadratures of the voltage response as a function of voltage offset in the y-axis and frequency in the x-axis. (c),(d) Vertical sections of the figures in (a),(b) at a fixed frequency.

Figure 6.20 shows a selection of resonance curves from Figure 6.19a when the offset voltage is changed by 100 mV. The resonance frequency is shifted by 0.5 MHz.

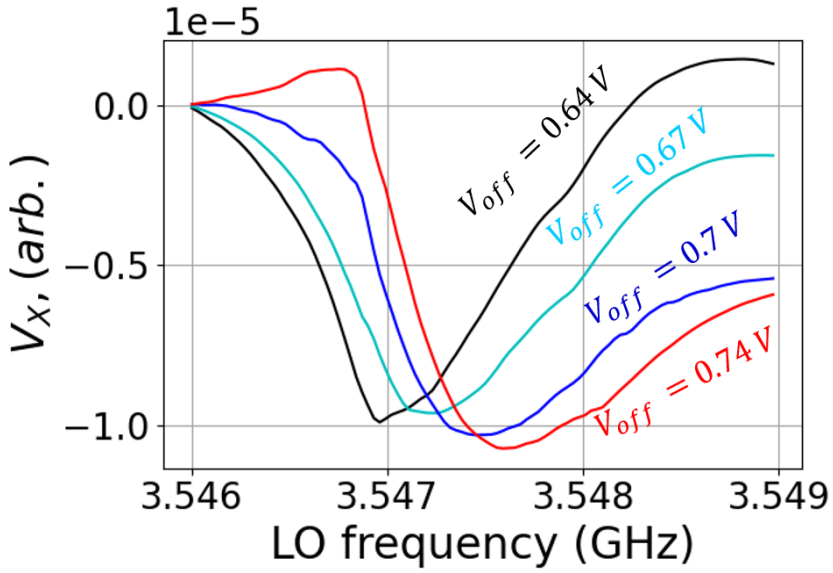

Figure 6.20: Resonance curves extracted from the lock-in measurement for various offset voltages.

From these curves, we are able to extract the resonance frequency and full width at half maximum (FWHM). To extract the resonance frequency f_{res}, we find the minimum point of each curve at fixed offset voltage. We determine the FWHM by first finding the 3 dB point. The curves we obtain are in general quite asymmetric, so for simplicity, we determine the peak of the curve ΔV to be the difference between the maximum and minimum of the curve. The 3 dB point, f_{3dB}, then occurs at $\frac{\Delta V}{\sqrt{2}}$ above the minimum point of the resonance curve. We then calculate the FWHM as $2(f_{res} - f_{3dB})$. Figure 6.21 shows an example of the determination of the resonance and 3 dB points.

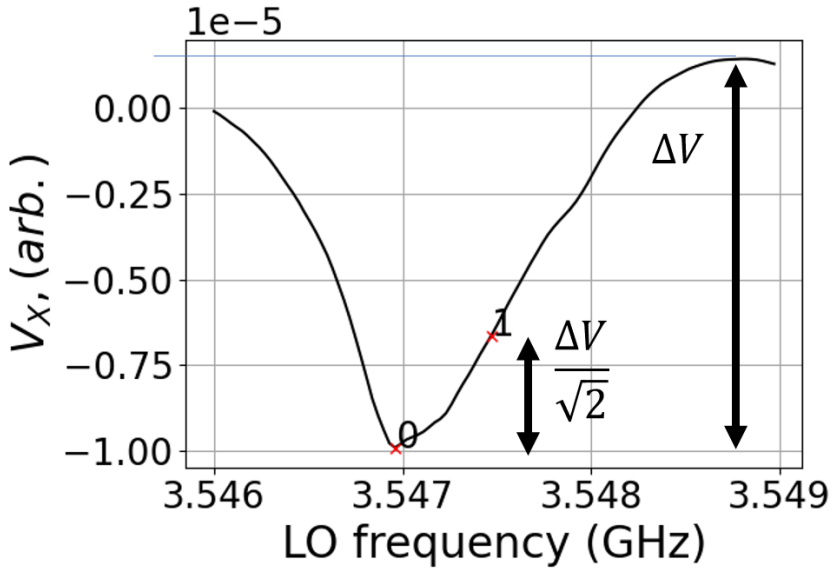

Figure 6.21: Resonance frequency and FWHM extraction. Red crosses labelled '0' and '1' are the resonance and 3 dB points respectively.

The extracted f_{res} and FWHM are plotted in Figure 6.22, extracted from the Y quadrature data over an offset voltage range of 1 V. The plot shows the periodic tuning of the f_{res} and FWHM. Correlated with the increase in f_{res} is the broadening of the resonance dip. The plot shows a lower bound of the resonance frequency at around 3.547 GHz, which changes by about 1 MHz, although some data points indicate that the change exceeds our measurement range. The FWHM at the lower f_{res} is around 0.5 MHz, and increases to about 2 MHz when the f_{res} is maximized.

We interpret our gated-nanowire device as an effective single nanowire, with a charge tuneable critical voltage, analogous to the DC SQUID. Critical voltage modulated by a gate voltage was experimentally observed in studies on the QPS transistor[79][146] which is dual to the DC SQUID, and the arguments for the DC SQUID could be applied to the case here. For charges Q_1 and Q_2 across the each nanowire, the net charge on the superconducting island at Q_g gate charge is

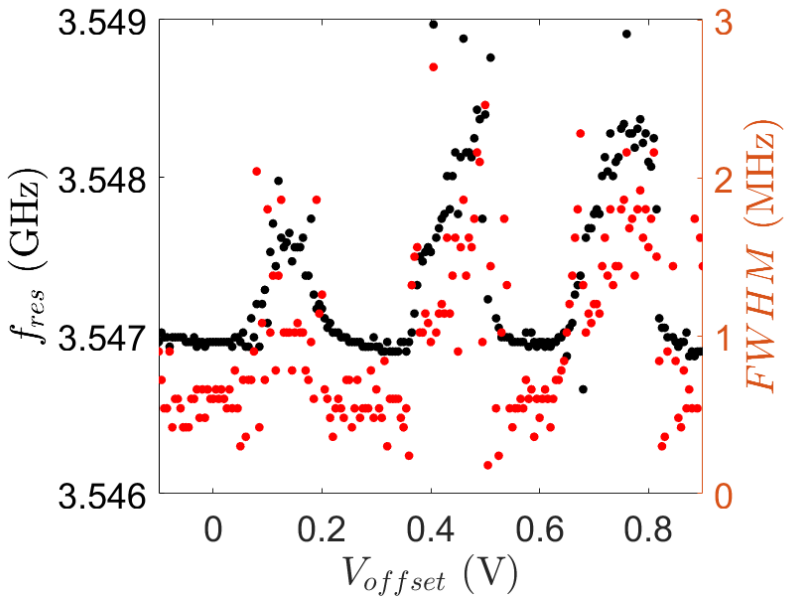

Figure 6.22: Periodic modulation of the resonance frequency (in black) and FWHM (in red) extracted from Y quadrature data due to the offset voltage.

$Q_2 - Q_1 + Q_g = 2en$. The voltage across two identical nanowires is then given by

$$\begin{aligned} V &= V_c(\sin 2\pi q_1 + \sin 2\pi q_2), \\ &= 2V_c \cos\left(\pi \frac{Q_g}{2e}\right) \sin\left(2\pi(q_1 + q_2)\right), \end{aligned} \tag{6.5}$$

where $q_i = \frac{Q_i}{2e}$ and the effective critical voltage of the ideal QPS transistor is $V_{c,eff} = |2V_c \cos(\pi \frac{Q_g}{2e})|$. The differential capacitance of the QPS transistor is thus

$$C = \frac{C_0'(Q_g)}{\cos\left(2\pi(q_1 + q_2)\right)}, \tag{6.6}$$

where $C_0'(Q_g) = \frac{e}{\pi V_{c,eff}} = \frac{e}{\pi |2V_c \cos(\pi \frac{Q_g}{2e})|}$. Asymmetry in the nanowires decreases the depth of modulation of the effective critical voltage, with the highly asymmetric limit, $a = \frac{V_{c2}}{V_{c1}} \ll 1$, giving $V_{c,eff} = V_{c1}\left[1 + a\cos\left(\frac{\pi Q_g}{e}\right)\right]$ [79]. The tuning of the capacitance explains qualitatively the changes we observe, but the data does not follow the simple sinusoidal dependence. Furthermore, the period of the critical voltage implies that C_g is of order 1 aF.

To conclude this section, we present some characterisation of the measurement in the form of input RF power and peak-to-peak voltage dependence V_{pp}. We have so far demonstrated periodic tuning of the resonator in the high power regime, as this resulted in the data with a better signal-to-noise ratio. Figure 6.23 show the X and Y quadrature data for an experiment at a fixed frequency of 3.5475 GHz and $V_{pp} = 0.2$ mV. The digital attenuator which controls the amount of power sent to the input line is calibrated so that 10 dB corresponds to an input power of 0 dBm. Thus we see that with an input power of -10 dBm (20 dB attenuation) a periodic modulation of the response is still observable albeit with a much weaker received signal. This is well in the linear regime and we also note that since the response is frequency dependent, the received signal might improve at a different set point.

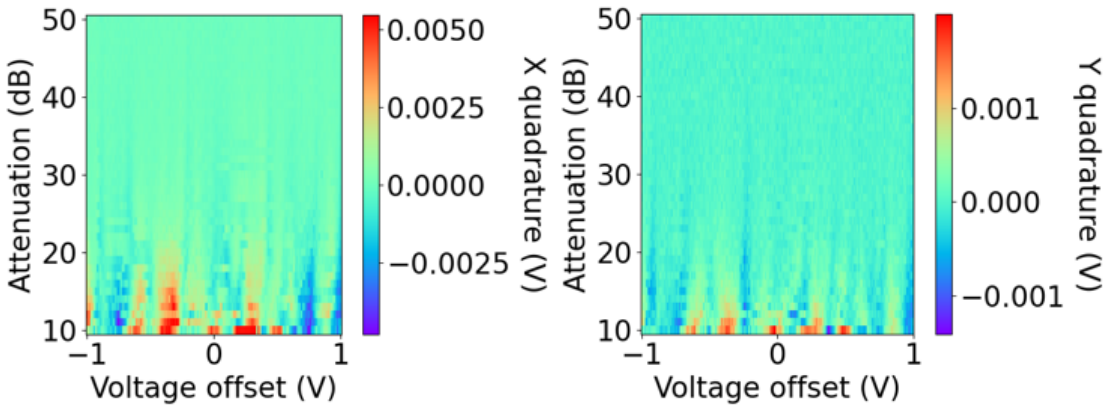

(a) (b)

Figure 6.23: X and Y quadrature of the response of the gated device at a fixed RF frequency of 3.5475 GHz and $V_{pp} = 0.2mV$.

Lastly, Figure 6.24 shows four different runs of our experiments to determine the V_{pp} dependence of measurements. To obtain this result, we set a RF frequency of 3.5475 GHz and input RF power of 0 dBm, and varied the V_{pp} as shown on the y-axis of these plots. The voltage offset is also varied to observe the periodicity for each V_{pp}. The plots show that the periodicity is approximately independent of the value of V_{pp}. In the course of making these measurements, we observed random period-halving events and this is shown in Figures 6.24b, c and d. Figures 6.24b and 6.24c are the same measurement taken at two different times. We see that the period which was taken to be ≈300 mV before, which occurs around V_{pp} = 30 mV to 60 mV has reduced to ≈150 mV at other parts of the figure. This is not a systematic effect of changing V_{pp}, but occurs randomly. Figure 6.24d shows a close-up of this effect. The change in period is possibly an observation of single charge tunnelling onto the island[147][148], which might be a source of noise for our measurements.

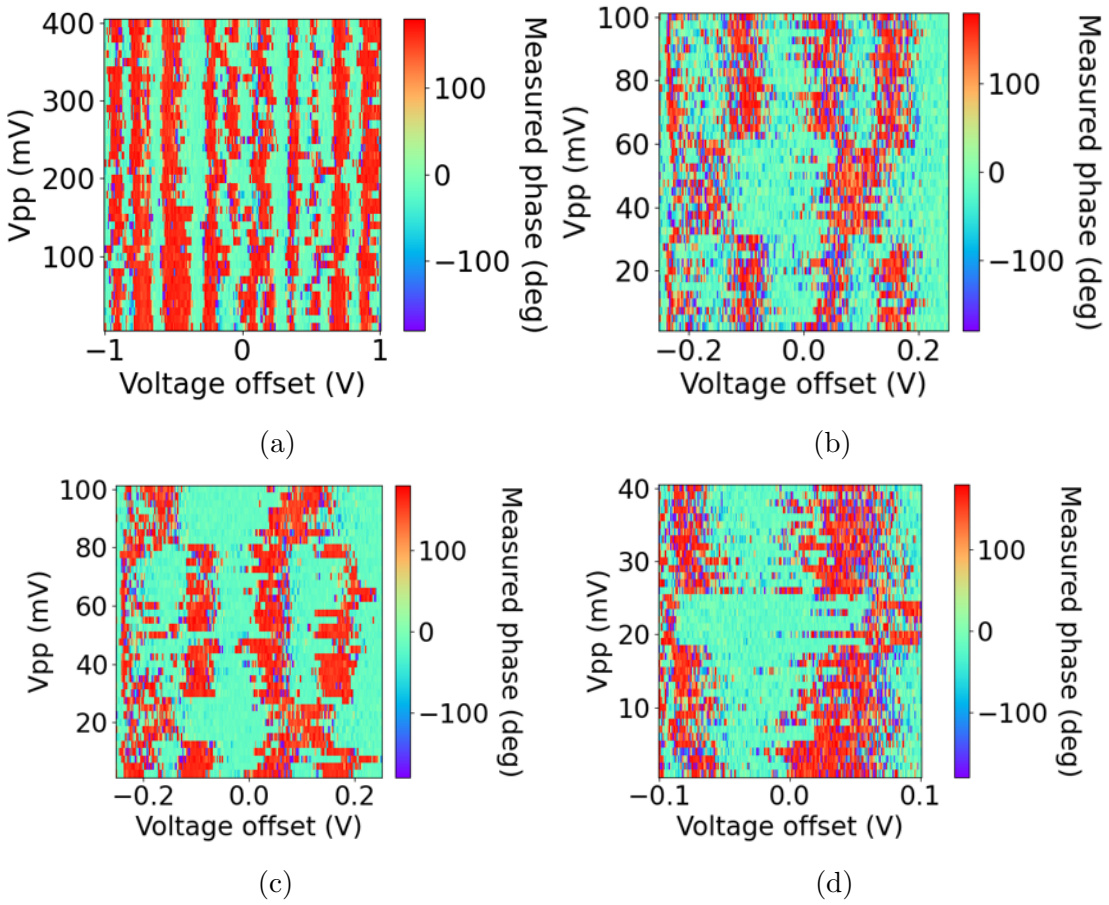

Figure 6.24: Effect of decreasing the peak-to-peak voltage of the measurement on the periodicity. (a) (b) and (c) Two runs of the same measurement with the same parameters. The halving of the periodicity occurs at random locations. (d) Measurement over a smaller voltage range showing a close-up of the random period switching.

6.5 Discussion and Outlook

In conclusion, we have fabricated two variants of a nonlinear resonator—one shunted by a nanowire, and a gate-tuneable variant which consists of two nanowires. For the first device, we demonstrated that it behaves as a driven Duffing oscillator, where the resonant frequency shifts lower with increasing power. We then applied two tones to the sample, a signal at frequency f_s and a pump at frequency f_p and measured the generated idler tone at $f_i = 2f_p - f_s$, indicating a degenerate four-wave mixing process. The idler tone is most prominent near the resonance frequency of the device and the maximum signal gain we found was 5 dB. While we demonstrated that our device is a nonlinear resonator, we have not yet identified the source of nonlinearity.

To show that the effect is due to the nanowires, we fabricated and characterised a gated variant of the device, containing a superconducting island capacitively coupled to a gate voltage bias line. We used a lock-in detection method to investigate the sensitivity of the device to the applied voltage. We first verified the lock-in detection method using the known magnetic response of the device. Subsequently, we exhibited a periodic tuning of the resonant behaviour as the offset voltage is varied. The period was determined to be 292 mV and the resonant frequency was tuned by $\approx$1 MHz. We suggest that the periodic behaviour is a result of the effective critical voltage modulation of our nanowires. We have also seen evidence for single-charge tunnelling onto the island when performing the experiments.

There remains a few outstanding questions yet to be answered in this chapter. The first is the differences in resonance frequencies between the single and double nanowire variants. While this may be attributed to the differences in impedance seen by the resonator in both cases, it has been difficult to rule out the difference in thin film properties. Second, the effective gate capacitance implied by the periodicity we observed is two orders of magnitude lower than the designed value. This may be due to additional capacitances to ground which we have neglected in the network, perhaps due to the capacitance of one or both of the nanowires.

Hongisto and Zorin[79] also report unexpectedly large periodicity in their sample and attribute this to a superconducting island within the nanowire itself that the gate is coupled to. Moreover, the resonance frequency and FWHM data extracted give only qualitative agreement with the model we described and deviations from this model have not been fully understood. Lastly, we have not yet characterised the three-wave mixing properties of the gated device before the end of this project.

We have so far demonstrated possible routes to realizing a nanowire-based dual to the JPA. However the performance of our devices are still far from the current state-of-the-art JPAs and JTWPAs described in Chapter 3. A number of optimizations in our design could help close the gap. The feedline-resonator coupling and the impedance matching to the external circuit are two design elements which can be improved further. A higher nanowire uniformity could also help achieve resonant frequency modulation over a wider range.

With the two-nanowire device, we demonstrated a voltage-tuneable resonator. Tuneable resonators are not only a core element in quantum-limited amplifiers, but in other quantum technologies such as in qubit readout architectures and long-range qubit coupling elements. Conventionally, they are implemented using SQUIDs and controlled using external magnetic fluxes, which are difficult to confine, making cross-talk an issue especially in larger, more complex systems. Electrostatic controls have the potential to overcome some of these issues, with recent publications in the literature implementing this function using hybrid superconductor-semiconductor devices[149] and graphene Josephson junctions[150]. Our work presented here, using superconducting nanowires, represents a novel approach, with a readily scalable fabrication process which can potentially be incorporated into a variety of quantum circuits.

Chapter 7

Conclusions and Outlook

Overall, the work presented in this thesis contributes to the expanding repertoire of superconducting quantum devices by addressing both the design aspects and practical implementation of nonlinear capacitors which includes qubit Hamiltonian engineering, JJ fabrication process development, and design and measurements of QPS nanowire-based circuits. To conclude, we summarize the main findings of this work and offer a brief outlook on potential directions for future research.

In Chapter 4 we considered the implementation of a YY coupler by numerically simulating the Hamiltonian of two flux qubits coupled to a tuneable capacitive coupler. As described in the review chapter, these interactions have the potential to enhance the performance of the current generation of quantum annealers, and also enable the representation of a larger class of Hamiltonians. We used quantum circuit analysis and qubit reduction method based on the Schrieffer-Wolff transformation to determine the circuit parameters required for an implementation of the device. We considered the sensitivity of the coupler to variations in fabrication, designed a circuit layout for an experimental chip and described measurements that can be carried out to verify our design. One obvious direction for extending this work is to fabricate and test the circuit in practice. Compatibility with other types of flux qubit designs and extensions to the coupler design could also be investigated.

In Chapter 5 we developed a fabrication process to produce overlap Josephson junctions in the LCN cleanroom. The main contributions here are the development of backsputtering and oxide growth techniques in our sputter deposition system. We characterised junctions under different processing conditions using resistance measurements and demonstrated the ability to change the interface properties of our methods. We also presented and analysed low temperature transport measurements of the junctions, and showed that they exhibited the characteristics of a nonhysteretic JJ. There is a lot of room for improvement in the methods considered here. In this initial study, we only used indirect methods to determine the properties of the junction interfaces, but its exact composition and structure is unknown. This can be studied using Transmission Electron Microscope (TEM) for inspecting the barrier quality to help understand how to better optimize our process. Furthermore, there is also scope for designing a better junction measurement setup for the low temperature experiments. A multiplexed arrangement will be better suited to allow for a larger number of devices to be characterised at a time, and enable better filtering on the shared leads needed for measuring nanoscale junctions.

Finally, in Chapter 6 we presented the experimental work on using quantum phase-slip nanowires as nonlinear capacitors for parametric amplification. Two variants were considered, one with a single nanowire, and another consisting of two nanowires with an island to which a voltage is applied through gate capacitor. The first device demonstrated all the indications of a nonlinear resonator and showed gain of 5 dB induced by a degenerate four-wave mixing process. For the second variant we developed and verified a lock-in detection method and demonstrated periodic tuning of the resonance frequency by the gate voltage. This proof of principle lays the groundwork for using QPS nanowires as nonlinear capacitive elements in superconducting RF electronics. Remained to be shown is the mixing properties the gated variant of the device. Particularly, parametric amplification by three-wave mixing, which this design enables, has not been verified experimen-

tally. This can be carried out by setting up a bias-tee near the sample space, which will allow both DC biasing and RF driving at the gate. A thorough and careful analysis of our experiments here could also be of great benefit to help understand how the designs can be further optimized for gain, noise performance or bandwidth as needed in a specific application. An interesting research direction could be to design and implement a travelling-wave amplifier based on a series array of QPS nanowires.

References

[1] Richard P. Feynman. "Simulating physics with computers". In: *International Journal of Theoretical Physics* 21.6 (June 1982), pp. 467–488. ISSN: 1572-9575. DOI: 10.1007/BF02650179.

[2] Peter W. Shor. *Fault-tolerant quantum computation*. 1996. DOI: 10.48550/ARXIV.QUANT-PH/9605011.

[3] Lov K. Grover. "A Fast Quantum Mechanical Algorithm for Database Search". In: *Proceedings of the Twenty-Eighth Annual ACM Symposium on Theory of Computing*. STOC '96. Philadelphia, Pennsylvania, USA: Association for Computing Machinery, 1996, pp. 212–219. ISBN: 0897917855. DOI: 10.1145/237814.237866.

[4] B. Camino et al. "Quantum computing and materials science: A practical guide to applying quantum annealing to the configurational analysis of materials". In: *Journal of Applied Physics* 133.22 (June 2023), p. 221102. ISSN: 0021-8979. DOI: 10.1063/5.0151346.

[5] L. Clinton et al. "Towards near-term quantum simulation of materials." In: *Nat Commun* 15 (2024), p. 211. DOI: 10.1038/s41467-023-43479-6.

[6] R. Santagati et al. "Drug design on quantum computers." In: *Nat. Phys.* 20 (2024), pp. 549–557. DOI: 10.1038/s41567-024-02411-5.

[7] D. Bluvstein et al. "Logical quantum processor based on reconfigurable atom arrays". In: *Nature* 626 (2024), pp. 58–65. DOI: 10.1038/s41586-023-06927-3.

[8] Jacquiline Romero and Gerard Milburn. *Photonic Quantum Computing*. 2024.

[9] Masoud Mohseni et al. *How to Build a Quantum Supercomputer: Scaling from Hundreds to Millions of Qubits*. 2025.

[10] Guido Burkard et al. "Semiconductor spin qubits". In: *Rev. Mod. Phys.* 95 (2 June 2023), p. 025003. DOI: 10.1103/RevModPhys.95.025003.

[11] L. M. K. Vandersypen et al. "Interfacing spin qubits in quantum dots and donors—hot, dense, and coherent". In: *npj Quantum Information* 3.1 (Sept. 2017). ISSN: 2056-6387. DOI: 10.1038/s41534-017-0038-y.

[12] S.K. Bartee et al. "Spin-qubit control with a milli-kelvin CMOS chip." In: *Nature* 643 (2025), pp. 382–387. DOI: 10.1038/s41586-025-09157-x.

[13] Daniel Basilewitsch, Clemens Dlaska, and Wolfgang Lechner. "Comparing planar quantum computing platforms at the quantum speed limit". In: *Phys. Rev. Res.* 6 (2 Apr. 2024), p. 023026. DOI: 10.1103/PhysRevResearch.6.023026.

[14] I. Siddiqi. "Engineering high-coherence superconducting qubits". In: *Nat Rev Mater* 6 (2021), pp. 875–891. DOI: 10.1038/s41578-021-00370-4.

[15] Yao-Yao Jiang et al. "Advancements in superconducting quantum computing". In: *National Science Review* 12.8 (June 2025), nwaf246. ISSN: 2095-5138. DOI: 10.1093/nsr/nwaf246.

[16] F. London, H. London, and Frederick Alexander Lindemann. "The electromagnetic equations of the supraconductor". In: *Proceedings of the Royal Society of London. Series A - Mathematical and Physical Sciences* 149.866 (1935), pp. 71–88. DOI: 10.1098/rspa.1935.0048.

[17] F. London. "On the Problem of the Molecular Theory of Superconductivity". In: *Phys. Rev.* 74 (5 Sept. 1948), pp. 562–573. DOI: 10.1103/PhysRev.74.562.

[18] V.L. Ginzburg and L.D. Landau. "73 - ON THE THEORY OF SUPERCONDUCTIVITY". In: *Collected Papers of L.D. Landau*. Ed. by D. TER HAAR. Pergamon, 1965, pp. 546–568. ISBN: 978-0-08-010586-4. DOI: https://doi.org/10.1016/B978-0-08-010586-4.50078-X.

[19] M. Cyrot. "Ginzburg-Landau theory for superconductors". In: *Rep. Prog. Phys.* 36 (1973), pp. 103–158.

[20] J. Bardeen, L. N. Cooper, and J. R. Schrieffer. "Theory of Superconductivity". In: *Phys. Rev.* 108 (5 Dec. 1957), pp. 1175–1204. DOI: 10.1103/PhysRev.108.1175.

[21] Leon N. Cooper. "Bound Electron Pairs in a Degenerate Fermi Gas". In: *Phys. Rev.* 104 (4 Nov. 1956), pp. 1189–1190. DOI: 10.1103/PhysRev.104.1189.

[22] D.H. Douglass and L.M. Falicov. "Chapter III The Superconducting Energy Gap". In: ed. by C.J. Gorter. Vol. 4. Progress in Low Temperature Physics. Elsevier, 1964, pp. 97–193. DOI: https://doi.org/10.1016/S0079-6417(08)60151-1.

[23] P. G. De Gennes. *Superconductivity of Metals and Alloys*. W. A. Benjamin, Inc., 1966. ISBN: 9780429497032.

[24] W S Corak et al. "Exponential temperature dependence of the electronic specific heat of superconducting vanadium". In: *Phys. Rev.; (United States)* 96 (Jan. 1954). DOI: 10.1103/PhysRev.96.1442.2.

[25] R. E. Glover and M. Tinkham. "Transmission of Superconducting Films at Millimeter-Microwave and Far Infrared Frequencies". In: *Phys. Rev.* 104 (3 Nov. 1956), pp. 844–845. DOI: 10.1103/PhysRev.104.844.

[26] Ivar Giaever and Karl Megerle. "Study of Superconductors by Electron Tunneling". In: *Phys. Rev.* 122 (4 May 1961), pp. 1101–1111. DOI: 10.1103/PhysRev.122.1101.

[27] Reinhold Kleiner and Dieter Koelle. “Appendix 1: Basic Properties of Superconductivity”. In: *The SQUID Handbook*. John Wiley & Sons, Ltd, 2004, pp. 357–366. ISBN: 9783527603640. DOI: https://doi.org/10.1002/3527603646.app1.

[28] Bascom S. Deaver and William M. Fairbank. “Experimental Evidence for Quantized Flux in Superconducting Cylinders”. In: *Phys. Rev. Lett.* 7 (2 July 1961), pp. 43–46. DOI: 10.1103/PhysRevLett.7.43.

[29] R. Doll and M. Näbauer. “Experimental Proof of Magnetic Flux Quantization in a Superconducting Ring”. In: *Phys. Rev. Lett.* 7 (2 July 1961), pp. 51–52. DOI: 10.1103/PhysRevLett.7.51.

[30] B.D. Josephson. “Possible new effects in superconductive tunnelling”. In: *Physics Letters* 1.7 (1962), pp. 251–253. ISSN: 0031-9163. DOI: https://doi.org/10.1016/0031-9163(62)91369-0.

[31] P. W. Anderson and J. M. Rowell. “Probable Observation of the Josephson Superconducting Tunneling Effect”. In: *Phys. Rev. Lett.* 10 (6 Mar. 1963), pp. 230–232. DOI: 10.1103/PhysRevLett.10.230.

[32] Sidney Shapiro. “Josephson Currents in Superconducting Tunneling: The Effect of Microwaves and Other Observations”. In: *Phys. Rev. Lett.* 11 (2 July 1963), pp. 80–82. DOI: 10.1103/PhysRevLett.11.80.

[33] Michael Tinkham. *Introduction to Superconductivity*. 2nd ed. Dover Publications, June 2004. ISBN: 9780486435039.

[34] John Clarke et al. “Quantum Mechanics of a Macroscopic Variable: The Phase Difference of a Josephson Junction”. In: *Science* 239.4843 (1988), pp. 992–997. DOI: 10.1126/science.239.4843.992.

[35] Michel H. Devoret, John M. Martinis, and John Clarke. “Measurements of Macroscopic Quantum Tunneling out of the Zero-Voltage State of a Current-Biased Josephson Junction”. In: *Phys. Rev. Lett.* 55 (18 Oct. 1985), pp. 1908–1911. DOI: 10.1103/PhysRevLett.55.1908.

[36] John M. Martinis et al. “Rabi Oscillations in a Large Josephson-Junction Qubit”. In: *Phys. Rev. Lett.* 89 (11 Aug. 2002), p. 117901. DOI: 10.1103/PhysRevLett.89.117901.

[37] Bernard Yurke and John S. Denker. “Quantum network theory”. In: *Phys. Rev. A* 29 (3 Mar. 1984), pp. 1419–1437. DOI: 10.1103/PhysRevA.29.1419.

[38] Michel H Devoret. *Quantum fluctuations in electrical circuits*. Elsevier, 1997, pp. 351–386.

[39] M. H. Devoret, A. Wallraff, and J. M. Martinis. *Superconducting Qubits: A Short Review*. 2004.

[40] Uri Vool and Michel Devoret. “Introduction to quantum electromagnetic circuits”. In: *International Journal of Circuit Theory and Applications* 45.7 (June 2017), pp. 897–934. DOI: 10.1002/cta.2359.

[41] Y. Nakamura, Yu. A. Pashkin, and J. S. Tsai. “Coherent control of macroscopic quantum states in a single-Cooper-pair box”. In: *Nature* 398.6730 (Apr. 1999), pp. 786–788. ISSN: 1476-4687. DOI: 10.1038/19718.

[42] Yu. A. Pashkin et al. “Quantum oscillations in two coupled charge qubits”. In: *Nature* 421.6925 (Feb. 2003), pp. 823–826. ISSN: 1476-4687. DOI: 10.1038/nature01365.

[43] T. Duty et al. “Coherent dynamics of a Josephson charge qubit”. In: *Phys. Rev. B* 69 (14 Apr. 2004), p. 140503. DOI: 10.1103/PhysRevB.69.140503.

[44] K Bladh et al. “The single Cooper-pair box as a charge qubit”. In: *New Journal of Physics* 7 (Aug. 2005), pp. 180–180. DOI: 10.1088/1367-2630/7/1/180.

[45] Alexander Shnirman, Gerd Schön, and Ziv Hermon. “Quantum Manipulations of Small Josephson Junctions”. In: *Phys. Rev. Lett.* 79 (12 Sept. 1997), pp. 2371–2374. DOI: 10.1103/PhysRevLett.79.2371.

[46] T. Duty et al. “Observation of Quantum Capacitance in the Cooper-Pair Transistor”. In: *Phys. Rev. Lett.* 95 (20 Nov. 2005), p. 206807. DOI: 10.1103/PhysRevLett.95.206807.

[47] Yu. A. Pashkin et al. "Josephson charge qubits: a brief review." In: *Quantum Inf Process* 8 (2009), pp. 55–80. DOI: 10.1007/s11128-009-0101-5.

[48] S. M. Girvin. "Circuit QED: superconducting qubits coupled to microwave photons". In: *Quantum Machines: Measurement and Control of Engineered Quantum Systems: Lecture Notes of the Les Houches Summer School: Volume 96, July 2011*. Oxford University Press, June 2014. ISBN: 9780199681181.

[49] T. P. Orlando et al. "Superconducting persistent-current qubit". In: *Physical Review B* 60.22 (Dec. 1999), pp. 15398–15413. DOI: 10.1103/physrevb.60.15398.

[50] J. E. Mooij et al. "Josephson Persistent-Current Qubit". In: *Science* 285.5430 (1999), pp. 1036–1039. DOI: 10.1126/science.285.5430.1036.

[51] Caspar H. van der Wal et al. "Quantum Superposition of Macroscopic Persistent-Current States". In: *Science* 290.5492 (2000), pp. 773–777. DOI: 10.1126/science.290.5492.773.

[52] J. Friedman et al. "Quantum superposition of distinct macroscopic states." In: *Nature* 406 (2000), pp. 43–46. DOI: doi.org/10.1038/35017505.

[53] I. Chiorescu et al. "Coherent Quantum Dynamics of a Superconducting Flux Qubit". In: *Science* 299.5614 (2003), pp. 1869–1871. DOI: 10.1126/science.1081045.

[54] Gioele Consani and Paul A Warburton. "Effective Hamiltonians for interacting superconducting qubits: local basis reduction and the Schrieffer–Wolff transformation". In: *New Journal of Physics* 22.5 (May 2020), p. 053040. DOI: 10.1088/1367-2630/ab83d1.

[55] A. M. Zagoskin. *Quantum Engineering: Theory and Design of Quantum Coherent Structures*. Cambridge University Press, 2011.

[56] Alexey Bezryadin. "Quantum suppression of superconductivity in nanowires". In: *Journal of Physics: Condensed Matter* 20.4 (Jan. 2008), p. 043202. DOI: 10.1088/0953-8984/20/04/043202.

[57] Andrew J Kerman. "Flux–charge duality and topological quantum phase fluctuations in quasi-one-dimensional superconductors". In: *New J. Phys.* 15 (2013). DOI: 10.1088/1367-2630/15/10/105017.

[58] J. S. Langer and Vinay Ambegaokar. "Intrinsic Resistive Transition in Narrow Superconducting Channels". In: *Phys. Rev.* 164 (2 Dec. 1967), pp. 498–510. DOI: 10.1103/PhysRev.164.498.

[59] D. E. McCumber and B. I. Halperin. "Time Scale of Intrinsic Resistive Fluctuations in Thin Superconducting Wires". In: *Phys. Rev. B* 1 (3 Feb. 1970), pp. 1054–1070. DOI: 10.1103/PhysRevB.1.1054.

[60] W. W. Webb and R. J. Warburton. "Intrinsic Quantum Fluctuations in Uniform Filamentary Superconductors". In: *Phys. Rev. Lett.* 20 (9 Feb. 1968), pp. 461–465. DOI: 10.1103/PhysRevLett.20.461.

[61] R. S. Newbower, M. R. Beasley, and M. Tinkham. "Fluctuation Effects on the Superconducting Transition of Tin Whisker Crystals". In: *Phys. Rev. B* 5 (3 Feb. 1972), pp. 864–868. DOI: 10.1103/PhysRevB.5.864.

[62] N. Giordano. "Evidence for Macroscopic Quantum Tunneling in One-Dimensional Superconductors". In: *Phys. Rev. Lett.* 61 (18 Oct. 1988), pp. 2137–2140. DOI: 10.1103/PhysRevLett.61.2137.

[63] N. Giordano. "Superconductivity and dissipation in small-diameter Pb-In wires". In: *Phys. Rev. B* 43 (1 Jan. 1991), pp. 160–174. DOI: 10.1103/PhysRevB.43.160.

[64] A. Bezryadin, C. Lau, and M. Tinkham. "Quantum suppression of superconductivity in ultrathin nanowires." In: *Nature* 404 (2000), pp. 971–974. DOI: 10.1038/35010060.

[65] A. T. Bollinger, A. Rogachev, and A. Bezryadin. "Dichotomy in short superconducting nanowires: Thermal phase slippage vs. Coulomb blockade". In: *Europhysics Letters* 76.3 (Sept. 2006), p. 505. DOI: 10.1209/epl/i2006-10275-5.

[66] A. T. Bollinger et al. “Determination of the Superconductor-Insulator Phase Diagram for One-Dimensional Wires”. In: *Phys. Rev. Lett.* 101 (22 Nov. 2008), p. 227003. DOI: 10.1103/PhysRevLett.101.227003.

[67] K. Andersson and D. B. Haviland. “Escape from a zero-current state in a one-dimensional array of Josephson junctions”. In: *Phys. Rev. B* 67 (9 Mar. 2003), p. 092507. DOI: 10.1103/PhysRevB.67.092507.

[68] I. Pop et al. “Measurement of the effect of quantum phase slips in a Josephson junction chain.” In: *Nature Phys* 6.6 (2010), pp. 589–592. DOI: 10.1038/nphys1697.

[69] Adem Ergül and et al. “Localizing quantum phase slips in one-dimensional Josephson junction chains.” In: *New J. Phys.* 15 (2013). DOI: 10.1088/1367-2630/15/9/095014.

[70] J E Mooij and C J P M Harmans. “Phase-slip flux qubits”. In: *New Journal of Physics* 7.1 (Oct. 2005), p. 219. DOI: 10.1088/1367-2630/7/1/219.

[71] J E Mooij et al. “Superconductor–insulator transition in nanowires and nanowire arrays”. In: *New Journal of Physics* 17.3 (Mar. 2015), p. 033006. DOI: 10.1088/1367-2630/17/3/033006.

[72] O. Astafiev et al. “Coherent quantum phase slip”. In: *Nature* 484 (2012), pp. 355–358. DOI: 10.1038/nature10930.

[73] J. T. Peltonen et al. “Coherent flux tunneling through NbN nanowires”. In: *Phys. Rev. B* 88 (22 Dec. 2013), p. 220506. DOI: 10.1103/PhysRevB.88.220506.

[74] J. Mooij and Y Nazarov. “Superconducting nanowires as quantum phase-slip junctions”. In: *Nature Phys* 2 (2006), pp. 169–172. DOI: 10.1038/nphys234.

[75] C. H. Webster et al. “NbSi nanowire quantum phase-slip circuits: dc supercurrent blockade, microwave measurements, and thermal analysis”. In: *Phys. Rev. B* 87 (14 Apr. 2013), p. 144510. DOI: 10.1103/PhysRevB.87.144510.

[76] K.Y. Arutyunov, J.S. Lehtinen, and T. Rantala. "The Quantum Phase Slip Phenomenon in Superconducting Nanowires with High-Impedance Environment". In: *J Supercond* 29 (Nov. 2016), pp. 569–572.

[77] Nicolas G. N. Constantino et al. "Emergence of Quantum Phase-Slip Behaviour in Superconducting NbN Nanowires: DC Electrical Transport and Fabrication Technologies". In: *Nanomaterials* 8.6 (2018). ISSN: 2079-4991. DOI: 10.3390/nano8060442.

[78] R.S. Shaikhaidarov et al. "Quantized current steps due to the a.c. coherent quantum phase-slip effect." In: *Nature* 608 (2022), pp. 45–49. DOI: 10.1038/s41586-022-04947-z.

[79] T. T. Hongisto and A. B. Zorin. "Single-Charge Transistor Based on the Charge-Phase Duality of a Superconducting Nanowire Circuit". In: *Phys. Rev. Lett.* 108 (9 Feb. 2012), p. 097001. DOI: 10.1103/PhysRevLett.108.097001.

[80] S. Kafanov and N. M. Chtchelkatchev. "Single flux transistor: The controllable interplay of coherent quantum phase slip and flux quantization". In: *Journal of Applied Physics* 114.7 (Aug. 2013), p. 073907. ISSN: 0021-8979. DOI: 10.1063/1.4818706.

[81] S.E. de Graaf et al. "Charge quantum interference device". In: *Nature Phys* 14 (2018), pp. 590–594. DOI: 10.1038/s41567-018-0097-9.

[82] Tadashi Kadowaki and Hidetoshi Nishimori. "Quantum annealing in the transverse Ising model". In: *Phys. Rev. E* 58 (5 Nov. 1998), pp. 5355–5363. DOI: 10.1103/PhysRevE.58.5355.

[83] B. Apolloni, C. Carvalho, and D. de Falco. "Quantum stochastic optimization". In: *Stochastic Processes and their Applications* 33.2 (1989), pp. 233–244. ISSN: 0304-4149. DOI: https://doi.org/10.1016/0304-4149(89)90040-9.

[84] Andrew Lucas. "Ising formulations of many NP problems". In: *Sec. Interdisciplinary Physics* 2 (Feb. 2014). DOI: 10.3389/fphy.2014.00005.

[85] R. Harris et al. “Compound Josephson-junction coupler for flux qubits with minimal crosstalk”. In: *Phys. Rev. B* 80 (5 Aug. 2009), p. 052506. DOI: 10.1103/PhysRevB.80.052506.

[86] Alec Maassen van den Brink, A J Berkley, and M Yalowsky. “Mediated tunable coupling of flux qubits”. In: *New Journal of Physics* 7.1 (Nov. 2005), p. 230. DOI: 10.1088/1367-2630/7/1/230.

[87] R. Harris et al. “Sign- and Magnitude-Tunable Coupler for Superconducting Flux Qubits”. In: *Phys. Rev. Lett.* 98 (17 Apr. 2007), p. 177001. DOI: 10.1103/PhysRevLett.98.177001.

[88] Steven J. Weber et al. “Coherent Coupled Qubits for Quantum Annealing”. In: *Physical Review Applied* 8.1 (July 2017). DOI: 10.1103/physrevapplied.8.014004.

[89] Eleni Marina Lykiardopoulou et al. “Improving nonstoquastic quantum annealing with spin-reversal transformations”. In: *Physical Review A* 104.1 (July 2021). DOI: 10.1103/physreva.104.012619.

[90] E. Y. Loh et al. “Sign problem in the numerical simulation of many-electron systems”. In: *Phys. Rev. B* 41 (13 May 1990), pp. 9301–9307. DOI: 10.1103/PhysRevB.41.9301.

[91] Ryan Babbush, Peter J. Love, and Alán Aspuru-Guzik. “Adiabatic Quantum Simulation of Quantum Chemistry”. In: *Scientific Reports* 4.1 (Oct. 2014). DOI: 10.1038/srep06603.

[92] Hidetoshi Nishimori and Kabuki Takada. “Exponential Enhancement of the Efficiency of Quantum Annealing by Non-Stoquastic Hamiltonians”. In: *Frontiers in ICT* 4 (Feb. 2017). DOI: 10.3389/fict.2017.00002.

[93] I. Ozfidan et al. “Demonstration of a Nonstoquastic Hamiltonian in Coupled Superconducting Flux Qubits”. In: *Phys. Rev. Applied* 13 (3 Mar. 2020), p. 034037. DOI: 10.1103/PhysRevApplied.13.034037.

[94] D. V. Averin and C. Bruder. "Variable Electrostatic Transformer: Controllable Coupling of Two Charge Qubits". In: *Phys. Rev. Lett.* 91 (5 July 2003), p. 057003. DOI: 10.1103/PhysRevLett.91.057003.

[95] H. Paik et al. "Cooper-pair box as a variable capacitor". In: *IEEE Transactions on Applied Superconductivity* 15.2 (2005), pp. 884–887. DOI: 10.1109/TASC.2005.850100.

[96] B. Yurke et al. "Observation of parametric amplification and deamplification in a Josephson parametric amplifier". In: *Phys. Rev. A* 39 (5 Mar. 1989), pp. 2519–2533. DOI: 10.1103/PhysRevA.39.2519.

[97] Bernard Yurke and Eyal Buks. "Performance of Cavity-Parametric Amplifiers, Employing Kerr Nonlinearites, in the Presence of Two-Photon Loss". In: *Journal of Lightwave Technology* 24.12 (2006), pp. 5054–5066. DOI: 10.1109/JLT.2006.884490.

[98] Erik A. Tholén et al. "Nonlinearities and parametric amplification in superconducting coplanar waveguide resonators". In: *Applied Physics Letters* 90.25 (June 2007), p. 253509. ISSN: 0003-6951. DOI: 10.1063/1.2750520.

[99] M. R. Vissers et al. "Low-noise kinetic inductance traveling-wave amplifier using three-wave mixing". In: *Applied Physics Letters* 108.1 (Jan. 2016), p. 012601. ISSN: 0003-6951. DOI: 10.1063/1.4937922.

[100] S. Frasca et al. "Three-wave-mixing quantum-limited kinetic inductance parametric amplifier operating at 6 T near 1 K". In: *Physical Review Applied* 21.2 (Feb. 2024). ISSN: 2331-7019. DOI: 10.1103/physrevapplied.21.024011.

[101] L.D. Landau and E.M. Lifshitz. *Mechanics, Second Edition*. 1969.

[102] Jose Aumentado. "Superconducting Parametric Amplifiers: The State of the Art in Josephson Parametric Amplifiers". In: *IEEE Microwave Magazine* 21.8 (2020), pp. 45–59. DOI: 10.1109/MMM.2020.2993476.

[103] Dominic William Jordan and P. Smith. *Nonlinear ordinary differential equations an introduction for scientists and Engineers*. Oxford University Press, 2007.

[104] M. A. Castellanos-Beltran. "Development of a Josephson Parametric Amplifier for the Preparation and Detection of Nonclassical States of Microwave Fields". PhD thesis. University of Colorado, 2010.

[105] T. Yamamoto et al. "Flux-driven Josephson parametric amplifier". In: *Applied Physics Letters* 93.4 (July 2008), p. 042510. ISSN: 0003-6951. DOI: 10.1063/1.2964182.

[106] A. A. Clerk et al. "Introduction to quantum noise, measurement, and amplification". In: *Rev. Mod. Phys.* 82 (2 Apr. 2010), pp. 1155–1208. DOI: 10.1103/RevModPhys.82.1155.

[107] M. A. Castellanos-Beltran and K. W. Lehnert. "Widely tunable parametric amplifier based on a superconducting quantum interference device array resonator". In: *Applied Physics Letters* 91.8 (Aug. 2007), p. 083509. ISSN: 0003-6951. DOI: 10.1063/1.2773988.

[108] Tanay Roy et al. "Broadband parametric amplification with impedance engineering: Beyond the gain-bandwidth product". In: *Applied Physics Letters* 107.26 (Dec. 2015), p. 262601. ISSN: 0003-6951. DOI: 10.1063/1.4939148.

[109] Theodore White and et al. "Readout of a quantum processor with high dynamic range Josephson parametric amplifiers". In: *Applied Physics Letters* 122.1 (Jan. 2023), p. 014001. ISSN: 0003-6951. DOI: 10.1063/5.0127375.

[110] Daniel Sank et al. "Measurement-Induced State Transitions in a Superconducting Qubit: Beyond the Rotating Wave Approximation". In: *Phys. Rev. Lett.* 117 (19 Nov. 2016), p. 190503. DOI: 10.1103/PhysRevLett.117.190503.

[111] N. E. Frattini et al. "Optimizing the Nonlinearity and Dissipation of a SNAIL Parametric Amplifier for Dynamic Range". In: *Phys. Rev. Appl.* 10 (5 Nov. 2018), p. 054020. DOI: 10.1103/PhysRevApplied.10.054020.

[112] C. Macklin et al. “A near–quantum-limited Josephson traveling-wave parametric amplifier”. In: *Science* 350.6258 (2015), pp. 307–310. DOI: 10.1126/science.aaa8525.

[113] Hampus Renberg Nilsson et al. “High-Gain Traveling-Wave Parametric Amplifier Based on Three-Wave Mixing”. In: *Phys. Rev. Appl.* 19 (4 Apr. 2023), p. 044056. DOI: 10.1103/PhysRevApplied.19.044056.

[114] Martina Esposito et al. “Perspective on traveling wave microwave parametric amplifiers”. In: *Applied Physics Letters* 119.12 (Sept. 2021), p. 120501. ISSN: 0003-6951. DOI: 10.1063/5.0064892.

[115] Kevin O’Brien et al. “Resonant Phase Matching of Josephson Junction Traveling Wave Parametric Amplifiers”. In: *Phys. Rev. Lett.* 113 (15 Oct. 2014), p. 157001. DOI: 10.1103/PhysRevLett.113.157001.

[116] Arpit Ranadive et al. “Kerr reversal in Josephson meta-material and traveling wave parametric amplification”. In: *Nature Communications* 13.1 (Apr. 2022). ISSN: 2041-1723. DOI: 10.1038/s41467-022-29375-5.

[117] Sergey Bravyi, David P. DiVincenzo, and Daniel Loss. “Schrieffer–Wolff transformation for quantum many-body systems”. In: *Annals of Physics* 326.10 (2011), pp. 2793–2826. ISSN: 0003-4916. DOI: https://doi.org/10.1016/j.aop.2011.06.004.

[118] D.P. Pappas, M. Field, and Kopas C.J. et al. “Alternating-bias assisted annealing of amorphous oxide tunnel junctions.” In: *Commun Mater* 5.150 (2024).

[119] I. M. Pop et al. “Fabrication of stable and reproducible submicron tunnel junctions”. In: *Journal of Vacuum Science & Technology B* 30.1 (Jan. 2012), p. 010607. ISSN: 2166-2746. DOI: 10.1116/1.3673790.

[120] Yashwanth Balaji et al. *Electron-beam annealing of Josephson junctions for frequency tuning of quantum processors*. 2024.

[121] J.B. Hertzberg, E.J. Zhang, and S. et al. Rosenblatt. "Laser-annealing Josephson junctions for yielding scaled-up superconducting quantum processors." In: *npj Quantum Inf* 7.129 (2021).

[122] T Yamamoto et al. "Superconducting flux qubit capacitively coupled to an LC resonator". In: *New Journal of Physics* 16.1 (Jan. 2014), p. 015017. DOI: 10.1088/1367-2630/16/1/015017.

[123] A. Wallraff et al. "Strong coupling of a single photon to a superconducting qubit using circuit quantum electrodynamics". In: *Nature* 431.7005 (Sept. 2004), pp. 162–167. DOI: 10.1038/nature02851.

[124] Alexandre Blais et al. "Cavity quantum electrodynamics for superconducting electrical circuits: An architecture for quantum computation". In: *Phys. Rev. A* 69 (6 June 2004), p. 062320. DOI: 10.1103/PhysRevA.69.062320.

[125] J. M. Fink et al. "Climbing the Jaynes–Cummings ladder and observing its nonlinearity in a cavity QED system". In: *Nature* 454.7202 (July 2008), pp. 315–318. DOI: 10.1038/nature07112.

[126] J. J. Sakurai. *Modern Quantum Mechanics (Revised Edition)*. 1st ed. Addison Wesley, Sept. 1993. ISBN: 0201539292.

[127] Alexandre Blais et al. "Circuit quantum electrodynamics". In: *Rev. Mod. Phys.* 93 (2 May 2021), p. 025005. DOI: 10.1103/RevModPhys.93.025005.

[128] Verjauw J. et al. "Path toward manufacturable superconducting qubits with relaxation times exceeding 0.1 ms". In: *npj Quantum Inf* 8.93 (2022). DOI: 10.1038/s41534-022-00600-9.

[129] N Foroozani et al. "Development of transmon qubits solely from optical lithography on 300 mm wafers". In: *Quantum Sci. Technol.* 4.025012 (2019).

[130] J M Kreikebaum et al. "Improving wafer-scale Josephson junction resistance variation in superconducting quantum coherent circuits". In: *Supercond. Sci. Technol.* 33.06LT02 (2020).

[131] Jochen Braumüller et al. “Multiphoton dressing of an anharmonic superconducting many-level quantum circuit”. In: *Phys. Rev. B* 91 (5 Feb. 2015), p. 054523. DOI: 10.1103/PhysRevB.91.054523.

[132] X. Wu et al. “Overlap junctions for high coherence superconducting qubits”. In: *Applied Physics Letters* 111.3 (July 2017), p. 032602. ISSN: 0003-6951. DOI: 10.1063/1.4993937.

[133] Alexander Stehli et al. “Coherent superconducting qubits from a subtractive junction fabrication process”. In: *Applied Physics Letters* 117.12 (Sept. 2020), p. 124005. ISSN: 1077-3118. DOI: 10.1063/5.0023533.

[134] C. M. Quintana et al. “Characterization and reduction of microfabrication-induced decoherence in superconducting quantum circuits”. In: *Applied Physics Letters* 105.6 (Aug. 2014), p. 062601. ISSN: 0003-6951. DOI: 10.1063/1.4893297.

[135] Lunjie Zeng et al. “Direct observation of the thickness distribution of ultra thin AlOx barrier in Al/AlOx/Al Josephson junctions”. In: *Journal of Physics D: Applied Physics* 48 (Sept. 2015). DOI: 10.1088/0022-3727/48/39/395308.

[136] A.W. Kleinsasser, R.E. Miller, and W.H. Mallison. “Dependence of critical current density on oxygen exposure in Nb-AlO/sub x/-Nb tunnel junctions”. In: *IEEE Transactions on Applied Superconductivity* 5.1 (1995), pp. 26–30. DOI: 10.1109/77.384565.

[137] K. Bayros et al. “Influence of pinholes and weak-points in aluminum-oxide Josephson junctions”. In: *Phys. Rev. Mater.* 8 (4 Apr. 2024), p. 046202. DOI: 10.1103/PhysRevMaterials.8.046202.

[138] Jochen Braumüller. “Development of a tunable transmon qubit in microstrip geometry”. Dec. 2013.

[139] J. Potter. “Experimental Study of the Quantum Phase-Slip Effect in NbN Nanowires”. July 2021.

[140] M. Göppl et al. "Coplanar waveguide resonators for circuit quantum electrodynamics". In: *Journal of Applied Physics* 104.11 (Dec. 2008), p. 113904. ISSN: 0021-8979. DOI: 10.1063/1.3010859.

[141] Spartak Gevorgian, LJ Peter Linner, and Erik L Kollberg. "CAD models for shielded multilayered CPW". In: *IEEE transactions on microwave theory and techniques* 43.4 (1995), pp. 772–779.

[142] David M. Pozar. *Microwave engineering*. Wiley, 1998.

[143] M. S. Khalil et al. "An analysis method for asymmetric resonator transmission applied to superconducting devices". In: *Journal of Applied Physics* 111.5 (Mar. 2012), p. 054510. ISSN: 0021-8979. DOI: 10.1063/1.3692073.

[144] Chunqing Deng, Martin Otto, and Adrian Lupascu. "An analysis method for transmission measurements of superconducting resonators with applications to quantum-regime dielectric-loss measurements". In: *Journal of Applied Physics* 114.5 (Aug. 2013), p. 054504. ISSN: 0021-8979. DOI: 10.1063/1.4817512.

[145] S. Probst et al. "Efficient and robust analysis of complex scattering data under noise in microwave resonators". In: *Review of Scientific Instruments* 86.2 (Feb. 2015), p. 024706. ISSN: 0034-6748. DOI: 10.1063/1.4907935.

[146] K. Yu. Arutyunov and J.S. Lehtinen. "Junctionless Cooper pair transistor". In: *Physica C: Superconductivity and its Applications* 533 (2017). Ninth international conference on Vortex Matter in nanostructured Superdonductors, pp. 158–160. ISSN: 0921-4534. DOI: https://doi.org/10.1016/j.physc.2016.02.010.

[147] F. W. J. Hekking et al. "Coulomb blockade of two-electron tunneling". In: *Phys. Rev. Lett.* 70 (26 June 1993), pp. 4138–4141. DOI: 10.1103/PhysRevLett.70.4138.

[148] T. M. Eiles, John M. Martinis, and Michel H. Devoret. "Even-odd asymmetry of a superconductor revealed by the Coulomb blockade of Andreev reflection". In: *Phys. Rev. Lett.* 70 (12 Mar. 1993), pp. 1862–1865. DOI: 10.1103/PhysRevLett.70.1862.

[149] William M. Strickland et al. “Superconducting Resonators with Voltage-Controlled Frequency and Nonlinearity”. In: *Phys. Rev. Appl.* 19 (3 Mar. 2023), p. 034021. DOI: 10.1103/PhysRevApplied.19.034021.

[150] G. Butseraen et al. “A gate-tunable graphene Josephson parametric amplifier”. In: *Nat. Nanotechnol.* 17 (2022), pp. 1153–1158. DOI: 10.1038/s41565-022-01235-9.